

# Spatio-temporal diagnostics of plasma fluctuations with probe arrays and statistical techniques

Dissertation

zur Erlangung des Doktorgrades

der Mathematisch-Naturwissenschaftlichen Fakultät

der Christian-Albrechts-Universität

zu Kiel

vorgelegt von

Iulian Teliban

Kiel

November 2006

Referent: Prof. Dr. A. Piel  
Korreferent: .....  
Tag der mündlichen Prüfung: 15. Dezember 2006  
Zum Druck genehmigt: .....

Der Dekan

## Kurzfassung

In dieser Arbeit werden fortgeschrittene diagnostische Methoden zur Analyse von Plasmaturbulenzfluktuationen untersucht und optimiert. Im Zentrum des Interesses stehen dabei 2D-Sonden-Arrays und die Methode der konditionellen Mittelung. Hierbei handelt es sich um weit verbreitete Diagnostiken zur raum-zeitlichen Untersuchung von Plasmafluktuationen. Zunächst wird die Leistungsfähigkeit von 2D-Sonden-Arrays unter wohl definierten Bedingungen, d.h. anhand von synthetischen und experimentellen Daten vom KIWI Experiment untersucht. Hierbei zeigt sich, dass die räumliche Auflösung der üblichen Sonden-Arrays zu gering ist, um anspruchsvolle Turbulenzuntersuchungen durchzuführen. Aus diesem Grund wird ein sogenannter "Super-Resolution"-Algorithmus, der aus dem Bereich der Computervision stammt, an die hier vorliegende Situation angepasst, der die Auflösung in beiden räumlichen Dimensionen verdoppelt. Die Leistungsfähigkeit des verwendeten Algorithmus wird anhand von simulierten Turbulenzdaten verifiziert. Im Anschluss werden die Möglichkeiten und Grenzen der konditionellen Mittelung anhand von synthetischen und experimentellen Daten des Blaamann Experiments untersucht. Auf den ersten Blick scheint die Methode der konditionellen Mittelung eine hohe räumliche und zeitliche Auflösung mit nur zwei Sonden zu erreichen. Allerdings wird durch den Mittelungsprozess die zeitliche Auflösung reduziert und somit die Untersuchung von schnellen dynamischen Vorgängen verfälscht, z.B. erscheinen dipolare Strukturen unter Umständen als Monopole. Um eine Vorstellung von den physikalischen Prozessen zu gewinnen, die sich mit den beschriebenen Methoden beobachten lassen, werden Vergleiche unter ähnlichen Plasmabedingungen im KIWI Experiment durchgeführt. Es wird gezeigt, dass konditionelle Mittelung nur in der näheren Umgebung um die Referenzsonde verlässliche Ergebnisse liefert. Im Gegensatz dazu ist es mit Hilfe des "Super-Resolution"-Algorithmus und 2D-Sonden-Arrays möglich, globale Untersuchungen der Plasmaturbulenz durchzuführen. Diese Ergebnisse zeigen, dass zur Untersuchung von Turbulenz, instantane raum-zeitliche Messungen notwendig sind.



## Abstract

In this work advanced diagnostic techniques, used to analyze plasma turbulence fluctuations, are investigated and optimized. For this reason diagnostics based on Langmuir probes such as 2D-probe arrays and conditional averaging method, used for spatio-temporal investigation of plasma fluctuations, are analyzed. First, the capabilities of probe-arrays are tested under well-defined conditions with synthetic data and experimental data from the linear KIWI device. It turns out, that the spatial resolution of standard probe-arrays is too low for advanced turbulence investigations. For this reason a super-resolution algorithm known from computer vision for image resolution enhancement is adapted to 2D-probe arrays. The improved performance of the super-resolution algorithm, which increases resolution by a factor of two in both spatial directions, is verified by using simulated turbulence data. Further, prospects and limitations of conditional averaging techniques are investigated on synthetic data and turbulence data from the Blaumann experiment. Although conditional averaging method shows an apparently high spatial and temporal resolution using just two probes, the averaging process implies that only the average temporal evolution is observed which can be quite different from real turbulence dynamics, e.g. dipolar structures can be distorted to appear as monopoles. To understand the physical processes resolved by these diagnostics, a comparison of their results on similar plasma conditions from KIWI turbulence regime is made. It is shown that conditional averaging gives reliable results only for local approximation around the reference probe while by super-resolving of the 2D-probe array data the global evolution is obtained. In this way it turns out, that for characterization of the turbulence instantaneous spatio-temporal measurements are needed.



# Contents

<b>1</b>	<b>Introduction</b>	<b>1</b>
<b>2</b>	<b>The experiment KIWI</b>	<b>5</b>
2.1	Experimental setup . . . . .	5
2.2	Diagnostics . . . . .	8
2.2.1	Electrostatic probes . . . . .	8
2.2.2	2D scanning system . . . . .	11
2.2.3	2D probe arrays . . . . .	12
2.3	Data analysis methods . . . . .	13
2.3.1	Statistical data analysis . . . . .	13
2.3.2	Correlation analysis . . . . .	14
2.3.3	Spectral analysis . . . . .	15
2.4	KIWI plasma characteristics . . . . .	15
2.4.1	Equilibrium profiles . . . . .	16
2.4.2	Plasma fluctuations . . . . .	18
2.5	Summary . . . . .	21
<b>3</b>	<b>Conditional averaging technique</b>	<b>23</b>
3.1	Technical description of standard CA method . . . . .	23
3.2	Analytical modeling of CA . . . . .	24
3.3	Prospects and limitations of CA . . . . .	28
3.3.1	Synthetic data . . . . .	28
3.3.2	Results and comparison . . . . .	29
3.4	Correlation analysis of CA-results . . . . .	32
3.5	Summary and remarks . . . . .	34
<b>4</b>	<b>Application of the CA technique to experiment</b>	<b>37</b>
4.1	Experimental details . . . . .	37
4.2	Application of CA to drift wave investigation . . . . .	38
4.3	Application of CA analysis to Blaamann turbulence data . . . . .	40

4.4	Application of CA analysis to KIWI turbulence data . . . . .	52
4.5	Conclusion . . . . .	54
<b>5</b>	<b>Technical issues</b>	<b>57</b>
5.1	The probe position estimation . . . . .	57
5.2	The probe size calibration . . . . .	60
<b>6</b>	<b>Super-resolution methods</b>	<b>65</b>
6.1	Super-resolution for image processing . . . . .	65
6.1.1	Super-resolution definition and requirements . . . . .	66
6.1.2	Super-resolution algorithm . . . . .	66
6.2	Super-resolution for plasma diagnostics . . . . .	71
6.2.1	Super-resolution algorithm for 2D probe arrays . . . . .	71
6.2.2	Optical flow vs. displacement vectors . . . . .	73
6.3	Remarks . . . . .	74
<b>7</b>	<b>Application of SR to plasma diagnostics</b>	<b>75</b>
7.1	Application to synthetic data . . . . .	75
7.2	Application to simulation turbulence data . . . . .	82
7.3	Summary and conclusion . . . . .	85
<b>8</b>	<b>Comparison of SR and CA</b>	<b>87</b>
8.1	Spatio-temporal characterization of weak turbulence . . . . .	87
8.1.1	Super-resolution results . . . . .	88
8.1.2	Conditional averaging results . . . . .	88
8.2	The amplitude evolution . . . . .	90
8.3	The spatio-temporal structure . . . . .	92
8.4	Conclusion . . . . .	93
<b>9</b>	<b>Summary and conclusions</b>	<b>97</b>
	<b>Bibliography</b>	<b>100</b>



# Chapter 1

## Introduction

Plasma fluctuation diagnostics in fusion devices has gained considerable interest for many years, since these fluctuations are the signature of plasma turbulence. Turbulence is responsible for the so-called anomalous radial transport [1, 2, 3, 4]. This relationship has indeed been verified, wherever the direct measurement of the turbulence-induced transport was possible, i.e. mainly in the plasma edge of fusion devices [3, 5, 6, 7] or in the low- $\beta$  laboratory plasma [8, 9, 10, 11]. The observed transport is usually not satisfactorily described by classical and neoclassical theory. Therefore, additional transport processes are responsible for the observed anomalous transport, such as  $\tilde{E} \times B$  convection in the turbulent electric field  $\tilde{E}$  [12, 13, 14, 15, 16]. Since the anomalous transport is the dominant restriction of the energy confinement in fusion devices, trying to understand the turbulence is worth the effort.

Langmuir probes are well established diagnostic tools in plasma physics [17, 18, 19] and perhaps, the simplest tool which can be used for plasma fluctuations diagnostic. They are found to be reliable diagnostics tools for low frequency plasma fluctuations in gas discharges [8, 20, 21], as well as at the plasma edges in fusion devices, i.e. in the limiter shadow or scrape-off layer (SOL) of tokamaks [7, 22, 23]. Langmuir probes have some great advantages: they are easy to use, allow for local measurement of plasma parameter, offer a fairly high temporal resolution, and give the opportunity to observe several fluctuating quantities at the same time.

Since turbulence is a spatio-temporal phenomenon, it is important to have not only a sufficient temporal resolution, but also to record fluctuations at several positions in space simultaneously. Along this idea, probe-arrays have been developed from one-dimensional (1D) to two-dimensional (2D) types. 1D-probe poloidal arrays have been successfully used in linear low- $\beta$  magnetized device for drift waves and turbulence investigations [24, 25, 26, 27, 28]. Linear arrays are used to diagnose fluctuations along the magnetic field lines [8]. Furthermore, 1D-arrays were found suitable for investigation of azimuthal plasma fluctuations and asymmetries in SOL [29, 30, 31]. Full space-time information about the plasma fluctuation were achieved

with a 2D-probe square array, by Zweben and Gould on the Caltech tokamak [32] and by Stroth *et. al.* in TJK [11, 33]. Angular arrays were used to explore the 2D spatial structure of the fluctuations in the plane perpendicular to the magnetic field in the SOL [5] and it was shown that more information can be obtained by the angular arrangement than by separate use of a poloidal and a radial array. However, all probe-array types are well localized and do not cover the full plasma cross-section.

Today, common spatio-temporal diagnostics rely on these probe arrays [24, 32, 34, 35, 36, 37] and on spectroscopic methods [38, 39, 40]. Their spatial resolution is limited by probe size, number of recording channels and plasma disturbance. They typically yield images with about  $10 \times 10$  data points, which corresponds to a minimum resolution of a few millimeters. Such a resolution is too poor for advanced turbulence investigations (energy cascades, transport barriers, etc.). Although these spatio-temporal diagnostics are very limited in spatial resolution, their temporal resolution is in most cases by far sufficient. In many cases sample rates of 1MS/s (Mega sample/second) are achieved, which is almost one order of magnitude higher than necessary.

On the other hand, the computational power of today's computers has allowed to run advanced simulations for turbulence studies in fluids and plasmas. They have shown that high spatial and temporal resolution are needed to gain insight, e.g. into the various transport processes being involved in fusion devices [41, 42, 43]. In fluids, experiments are almost competitive with simulations [44]. Using tracer particles and direct imaging techniques a wide range of spatial and temporal scales is covered. Typical image resolution is of the order of Megapixels, i.e. the diagnostic allows to detect structures simultaneously, which differ in size by three orders of magnitude. To achieve similar spatial resolution in plasma diagnostics is much more difficult. Recent studies show that direct imaging is possible [45, 46, 47], but the resolution is well below Megapixels and the technique is very demanding and not applicable in general. At the moment, a sufficient spatial resolution with Langmuir probes can only be obtained by statistical techniques, e.g. conditional averaging [48, 49, 50] or cross-correlation [51, 52, 53]. However, the averaging process implies a loss of information; namely only the average temporal evolution is observed, which can be quite different from the instantaneous dynamics.

These limitations of diagnostics with Langmuir probes provoke a series of questions which are worth to be answered:

- Is the resolution of the probe arrays sufficient for turbulence investigation?
- Are there possibilities to enhance the spatial resolution of 2D-arrays?
- Are the results of statistical methods, i.e. conditional averaging, reliable for the understanding of turbulence?

To tackle the resolution problem these questions are addressed with data from

a 2D-probe array in the linear KIWI<sup>1</sup> device [54, 55, 56]. For this reason the technical aspects of the device are shortly summarized (chapter 2). For this plasma type, Langmuir probes are well established methods for measuring density and potential fluctuations. To attack the first question monochromatic drift modes and the weak turbulence regime are investigated (chapter 5). This approach is possible due to the well known features of KIWI plasma. Furthermore, the resolution of the probe array is examined with synthetic data (chapter 7). To approach the second question an attempt is made to adapt a method of image enhancement from *computer vision* to probe arrays data with a limited number of probes (chapter 6). The method is tested on well defined data as synthetic data and simulated data of plasma turbulence (chapter 7). Because statistical methods yield sufficient spatial resolution an averaging techniques, such as "conditional averaging" between two probes is investigated and optimized (chapter 3 and 4). To understand the physical processes resolved by this method a comparison with full probe-array data is proposed (chapter 8).

---

<sup>1</sup>Kiel Instrument for Wave Investigations



# Chapter 2

## The experiment KIWI

This chapter describes the KIWI experiment and the diagnostics used in this work. The first part focuses on the technical description of the device. Further the diagnostic methods are introduced. The methods used for data analysis are also briefly described from the theoretical point of view. The plasma equilibrium is investigated by density, potential and temperature profiles. The equilibrium is characterized to provide the basis for the spatio-temporal fluctuations analysis. The fluctuation analysis is resumed, in this chapter, only to the temporal dynamics investigation. The spatio-temporal analysis will require more attention in this work and is the subject of the next chapters.

### 2.1 Experimental setup

The experiments are performed in a linear magnetized device, KIWI (Kiel Instrument for Waves Investigations) (Fig. 2.1) [54, 55, 56]. It consists of two identical cylindrical source chambers with a diameter of 80 cm and a midsection of 180 cm length and 30 cm diameter. The two source chambers are separated from the midsection by biased stainless steel mesh grids with transparency of 68%. For the investigations presented in this work, only one chamber is operated. The separation grid of the active source chamber is biased positive and the second grid, as well as all parts of the inactive source chamber are kept at ground voltage, i.e. they are acting as loss surfaces.

The plasma is produced inside of the active source chamber by a thermionic hot-cathode discharge in Argon using an array of 18 filaments. Typical technical parameters for the proper plasma production are listed in Tab. 2.1. The resulting plasma enters in the central section by diffusion, caused in principal by the axial density gradient between the source chamber and the midsection. The plasma produced in the source chamber is coupled into the midsection via the biased grid. By using additional field coils at the ends, the magnetic field of the midsection can be

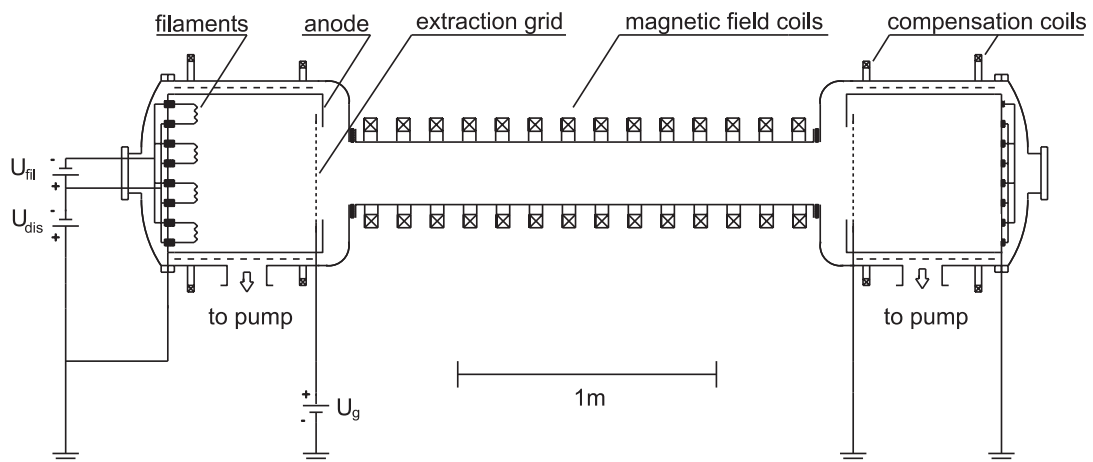
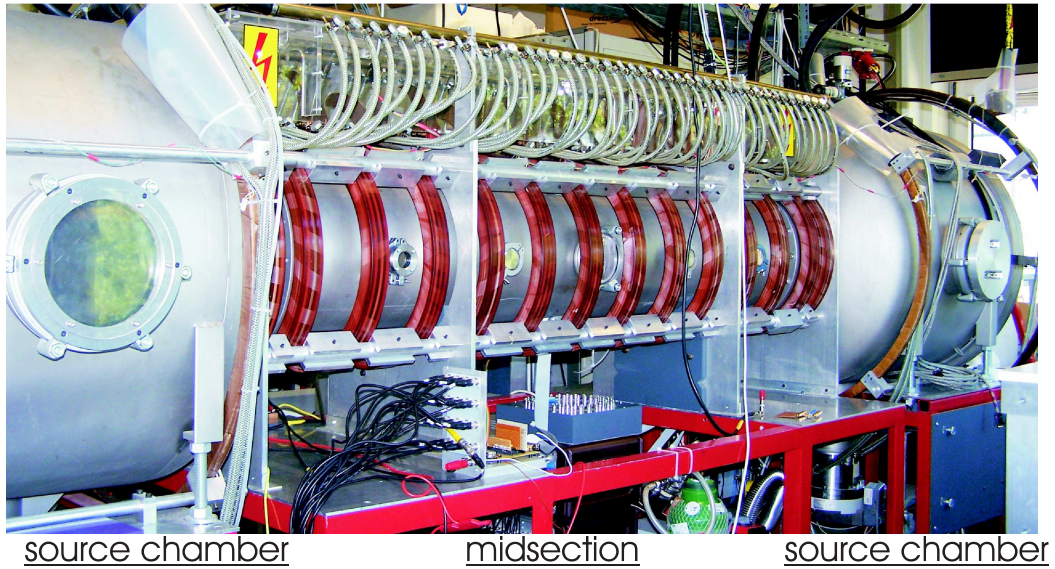


Figure 2.1: Picture of the triple plasma device KIWI. The sketch shows the device components in detail. It shows the experimental arrangement used in this work. Typical operation in this work is with just one active source chamber. The second grid is fully grounded to act as a well defined boundary.

Parameter	Value
base pressure	$4 - 8 \cdot 10^{-5}$ Pa
neutral gas pressure	$1 - 5 \cdot 10^{-2}$ Pa
discharge voltage	$U_{dis} = 65$ V
discharge current	$I_{dis} = 5 - 12$ A
filament voltage	$U_{fil} = 15$ V
filament current	$I_{fil} = 60 - 78$ A
grid voltage	$U_g = 0 - 14$ V
magnetic field (midsection)	$B = 0.07$ T

Table 2.1: Kiwi operation parameters

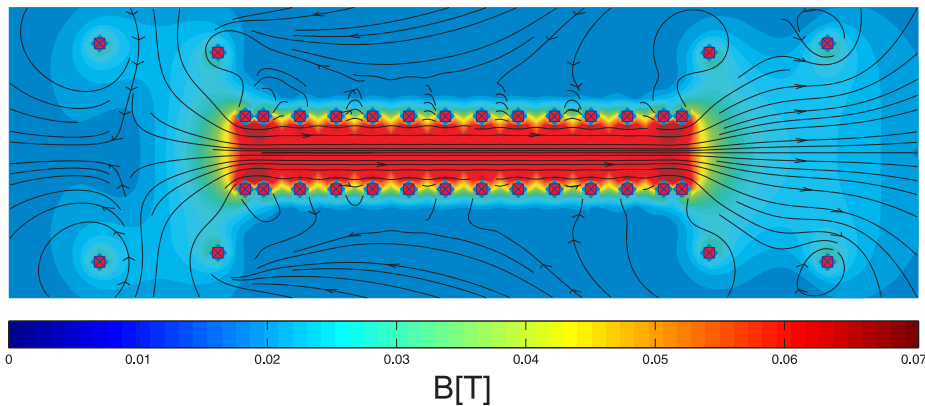


Figure 2.2: The magnetic field calculation for KIWI experiment coils. The black lines denote the field lines and the arrows indicate direction of the magnetic field. The coil position is indicated by  $\boxtimes$ . The magnetic field is computed for typical KIWI operation condition ( $I_{coil} = 320A$ ).

almost compensated to reduce magnetic mapping of the primary electrons between the source chamber and the midsection [57] (Fig. 2.2). For a better emission [57] the hot filaments are localized in the magnetic gap formed by cusp operation geometry of compensation coils. In addition permanent magnets are used as a magnetic wall in line cusp geometry in order to increase the ionization efficiency of the primary electrons in the source chamber [58, 59, 60]. Therefore, the longer trapping time of the charged particles in the source leads to a better thermalization of the plasma, i.e. the velocity distribution function is almost Maxwellian. The magnetic field in the midsection, produced by a set of 14 magnetic field coils, is homogeneous with typically 0.07 T and the magnetic field ripple less than 5%, except for the ends Fig. 2.2, where the field lines are diverging. In this way a weakly ionized plasma column (ionization degree  $< 0.1\%$ ) is produced in the magnetized midsection.

The most important feature of the KIWI is its steady state operation with stable plasma condition for several hours. This founds the basis for measurements with high

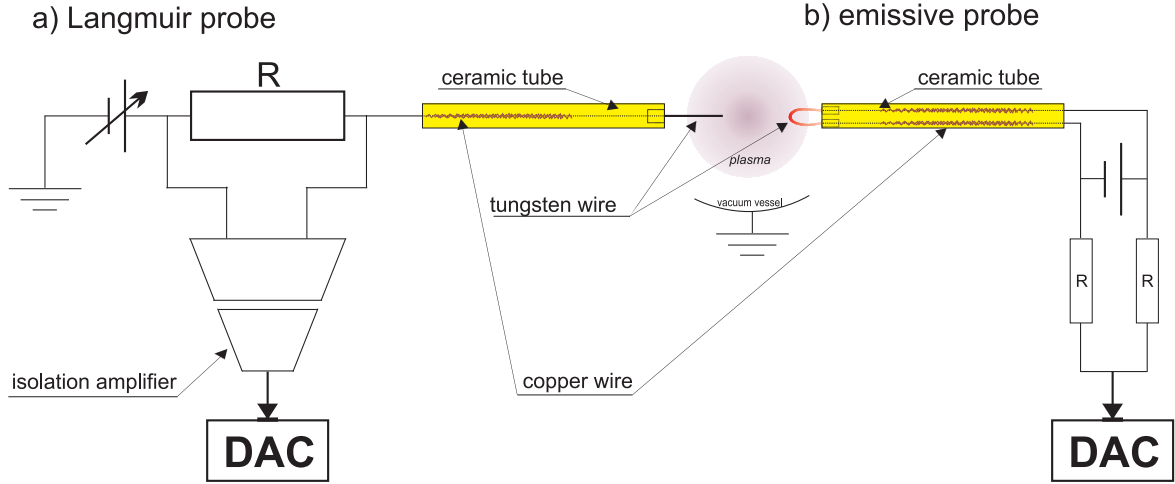


Figure 2.3: Schematic diagram of measurement circuits for Langmuir (a) and emissive (b) probes. The vacuum vessel acts as reference electrode. For a symmetric pickup the emissive probe uses two equal resistors.

spatial and temporal resolution. The long time series permit statistical methods for the data analysis.

## 2.2 Diagnostics

The main diagnostic tools in this work are electrostatic probes. They have the advantage to measure several plasma quantities with high spatial and temporal resolution. The following section will give a short description of Langmuir and emissive probes.

### 2.2.1 Electrostatic probes

#### Langmuir probes

In the most common case Langmuir probes consist of small electrodes inserted into plasma Fig. 2.3a. Biasing of the probe against the plasma a shield forms around the probe (Debye sheath). It accelerates or repels the plasma species (electrons, ions) towards the probe surface. The current picked up at the probe from plasma at different bias voltage draws the *current-voltage probe characteristic*. From this characteristic some plasma parameters can be estimated: the electron temperature  $T_e$ , the plasma potential  $U_p$  and the plasma density  $n$ . A typical probe characteristic is shown in Fig. 2.4. It is a convention to plot the reversed probe current for a better visualization. In general the current-voltage probe characteristic consists of three regions.



A. If the probe is biased at potentials much smaller than the plasma potential,  $U \ll U_p$ , all electrons are repelled and the current is carried exclusively by the ions<sup>1</sup> (region A in Fig. 2.4). The net current to the probe is given by the ion saturation current [17, 18]

$$I = I_{i,sat} = 0.61 \cdot n_e \cdot e \cdot A \cdot \sqrt{\frac{k_B \cdot T_e}{m_i}} \quad (2.1)$$

where  $n_e$  is the electron density,  $e$  the elementary charge,  $k_B$  the Boltzmann constant,  $T_e$  the electron temperature,  $m_i$  the ion mass and  $A$  is the effective probe surface.

B. By reducing the probe bias, more and more electrons have sufficient kinetic energy to reach the probe. The electron current contribution to total probe current, assuming Maxwellian velocity distribution, increases exponentially until the probe bias equals the plasma potential  $U_p$  (region B in Fig. 2.4)

$$I_e = I_{e,sat} \cdot \exp\left(\frac{e(U - U_p)}{k_B \cdot T_e}\right) \quad (2.2)$$

where  $I_{e,sat}$  is the electron saturation current,  $U$  the probe potential and  $U_p$  the plasma potential. In this regime the net current to the probe is

$$I = I_{i,sat} + I_e \quad (2.3)$$

For the point where  $I = 0$  (floating probe,  $U = U_f$ ) the probe voltage is more negative with respect to the plasma potential due to the higher mobility of the electrons in comparison with ions.

C. For larger bias than the plasma potential (region C in Fig. 2.4) all the electrons reach the probe and the ions are repelled. In contrast with the ion saturation regime, the electron saturation regime depends on the probe shape. In practice, for the planar probes (ideal with guard ring) a real saturation can be observed while for the cylindrical (used in this work) and spherical probes the current increase monotonically. This is mainly caused by an increase of the collecting area with probe voltage. In particular not the effective probe surface itself acts as collecting area but the probe sheath. If the sheath length ( a few Debye lengths  $\lambda_D = (\epsilon_0 T / e^2 n_e)^{1/2}$ ) is much smaller than typical probe dimensions  $d$ , i.e. probe diameter, the collecting area is the surface area of the probe  $A$ . For a sheath length larger than  $d$  the probe current is determined by orbital motion of the plasma particles (OML) [19, 61, 62, 63]. The ion current can be neglected and the net current to the probe in the electron saturation regime is given by

$$I = I_{e,sat} = -n_e \cdot e \cdot A \cdot \sqrt{\frac{k_B T_e}{2\pi m_e}}. \quad (2.4)$$

In general involving equations describing the ion Eq. 2.2 and electron Eq. 2.4 currents, plasma density and the electron temperature are obtained [17, 18]. In

---

<sup>1</sup>In the KIWI device only single charged positive ions are observed

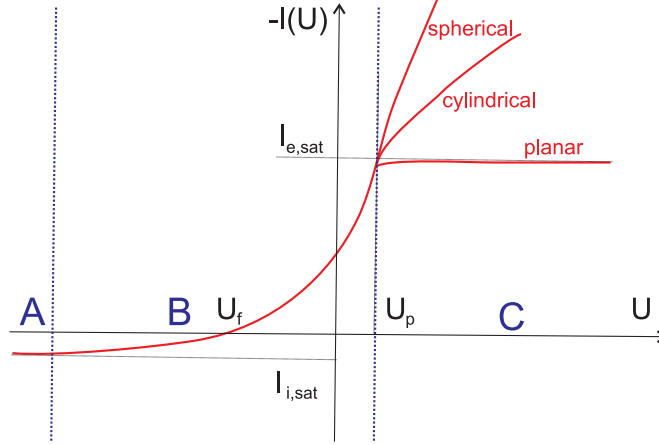


Figure 2.4: Typical voltage-current probe characteristic. The three specific regimes are separated by blue vertical lines. By  $U_f$  and  $U_p$  the floating and plasma potential are denoted.  $I_{i,sat}$  and  $I_{e,sat}$  represents the saturation value of ion and electron current respectively. Note the different behavior of plane, cylindrical and spherical probe at voltages higher than the plasma potential.

magnetized plasma the probe characteristic analyze becomes much more complex because the magnetic field leads to a strong anisotropy of the plasma. A detailed analysis algorithm used at this experiment with the complications related to magnetized plasma can be found in [64].

The evaluation of the probe characteristics for fluctuating quantities is a quite complicated task. For the fluctuating plasma parameters of the form

$$n = n_0 + \tilde{n}, \quad U_p = U_{p0} + \tilde{U}_p \quad \text{and} \quad T_e = T_{e0} + \tilde{T}_e \quad (2.5)$$

which extent up to several hundred kHz for the turbulent plasma, the probe voltage has to sweep at several MHz to get a sufficient high number of data points for a probe characteristic. By considering that the electron temperature fluctuation can be negligible, the fluctuating quantities are estimated at constant probe bias by using the following assumptions

$$\tilde{n} \approx \frac{\tilde{I}_{i,sat}}{\sqrt{T_{e0}}}, \quad (2.6)$$

$$\tilde{U}_p \approx \tilde{U}_f. \quad (2.7)$$

These equations show that the floating potential and the ion saturation current fluctuations can be interpreted as fluctuations of density and plasma potential.

### Emissive probes

The estimation of the plasma potential can be done directly from the probe characteristic (turning point). The detection of the turning point is sometimes a sophisticated task and requires a full probe characteristic. It can be affected by the probe geometry, ion and electron beams etc [65]. An emissive probe is an alternative to measure directly plasma potential from a simple floating potential measurement [66, 67, 68, 69]. An emissive probe is practically realized by a small loop of tungsten wire inserted into double bore ceramic tube as shown in Fig. 2.3b. It is heated until electron emission occurs by applying an external electric current through it. If the probe voltage is smaller than the plasma potential  $U_p$  the emitted electrons flow to the plasma. In this case the current towards the probe is given by:

$$I = I_i + I_{em} - I_e. \quad (2.8)$$

where  $I_{em}$  is the emitted electron current given by Richardson's law

$$I_{em} = K \cdot T_w^2 \cdot \exp\left(-\frac{e \cdot W_w}{K_B \cdot T_w}\right), \quad (2.9)$$

where  $K$  is the Richardson constant ( $K = 6.012 \cdot 10^5 \text{ Am}^{-2} \text{ K}^{-2}$ ),  $W_w$  is the work function of the wire material and  $T_w$  is the temperature of the emitting wire ( $I_{em} \gg I_i$  for high temperature). Inserting eq. 2.2 and 2.1 into the eq. 2.8 and considering only the floating point ( $I = 0$  and  $U = U_f$ ) yields

$$U_f = U_p - \frac{k_B \cdot T_e}{e} \cdot \ln\left(\frac{I_{e,sat}}{I_{i,sat} + I_{em}}\right). \quad (2.10)$$

By regulating the heating current through the probe the emitting current equals the electron saturation current ( $\ln(I_{e,sat}/(I_{i,sat} + I_{em})) \approx 0$ ). The result is, that the floating potential becomes nearly identical with the plasma potential [65]. Therefore the plasma potential and its fluctuations can be measured directly by the floating potential of the emissive probe. Due to the disturbance caused by the electron emission on the surrounding plasma and on other probes it is used (in this work) only to determine the equilibrium plasma potential.

### 2.2.2 2D scanning system

For the spatial plasma diagnostic a 2D probe positioning system is mounted in the middle of the magnetized midsection Fig. 2.5. It can scan the poloidal cross-section perpendicular to the magnetic field and covers almost the entire device cross-section. The poloidal plan can be scanned with a spatial resolution of 1 mm. Depending on the plasma quantity to be measured, Langmuir or emissive probes are mounted on this positioning system. This system is used for the plasma equilibrium profile estimation and also for the plasma fluctuation analysis, i.e. the conditional averaging and the cross-correlation analysis.

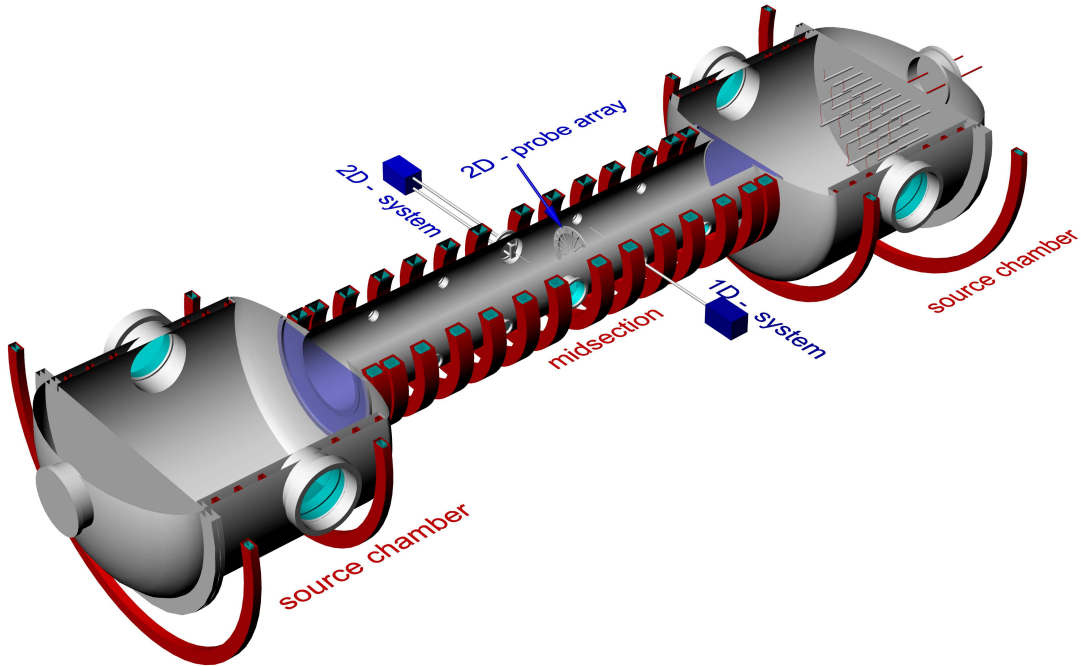


Figure 2.5: The 3D drawing of triple plasma device KIWI. The sketch shows the device components in detail. It shows the experimental arrangement used in this work. All probe diagnostics are close to the center of the midsection, i.e. well separated from the grid region.

### 2.2.3 2D probe arrays

The advantage of multi-probe arrays to gain spatio-temporal information about the plasma fluctuation has already been shown in previous investigations on the KIWI device [24, 25, 8, 27]. Here, a new circular probe array system has been designed and optimized for an uniform full coverage of the plasma column. It includes 63 regular spaced probes distributed to 9 bars of 4 probes and 9 bars of 3 probes each, Fig. 2.6. Each probe consists of a tungsten wire of  $200\ \mu\text{m}$  diameter and about 4 mm length. A detailed technical sketch of the entire system is shown in Fig. 2.7. The radial position of the probes can be varied in the range of  $\pm 1\text{cm}$  by a special adjusting system. The heavy support permits also an azimuthal rotation of the entire probe array inside of the vacuum vessel. This allows for an equidistant probe arrangement on arbitrary contours.

All channels are simultaneously acquired by a 16-Bit 64 channel transient recorder (Nicolet) with storage capacity of 1 Megasample per channel. The maximum sample rate is 1 MHz. The DC part is removed by the capacitor (C), Fig. 2.7.

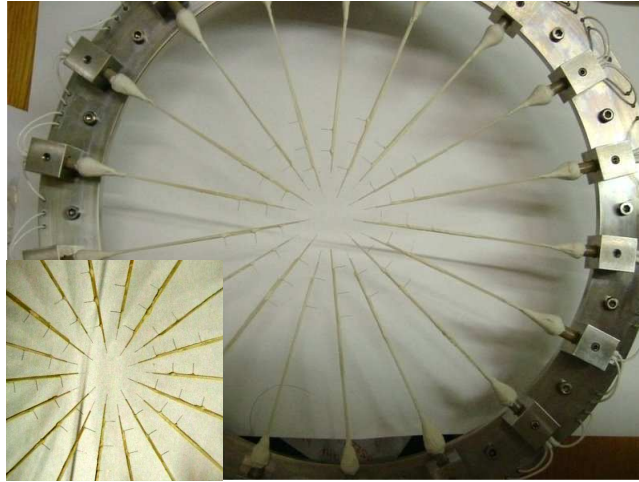


Figure 2.6: Picture of 2D probe array. The probe distribution is shown by the close-up picture in the lower left corner. Technical details are shown in Fig. 2.7

Hence, only the fluctuations are recorded. To measure the plasma density fluctuations, all probes are negatively biased by a set of batteries as shown in Fig. 2.7. The density fluctuations are taken as the current fluctuations through  $R_S$ . Plasma potential fluctuations are estimated from the floating potential measurements by removing the bias on the probes (red line in Fig. 2.7).

## 2.3 Data analysis methods

To analyze fluctuation quantities in general statistical and spectral methods are used [70, 71]. The basic description and notations for the probability density function, correlation functions and the Fourier analysis to time series, are introduced for reference.

### 2.3.1 Statistical data analysis

In the KIWI experiment, typical data sets are recorded with a sample frequency of 1 MHz and up to 1 million data points. The long time series are well suited for a statistical analysis. The statistical characterization of the time series is done by the probability density function and its moments. The Probability Density Function (PDF),  $P(n)$ , is defined as the probability to find a value,  $n$ , within the amplitude interval  $[n, n + dn]$ . The function normalization implies

$$\int_{-\infty}^{+\infty} P(n) dn = 1. \quad (2.11)$$

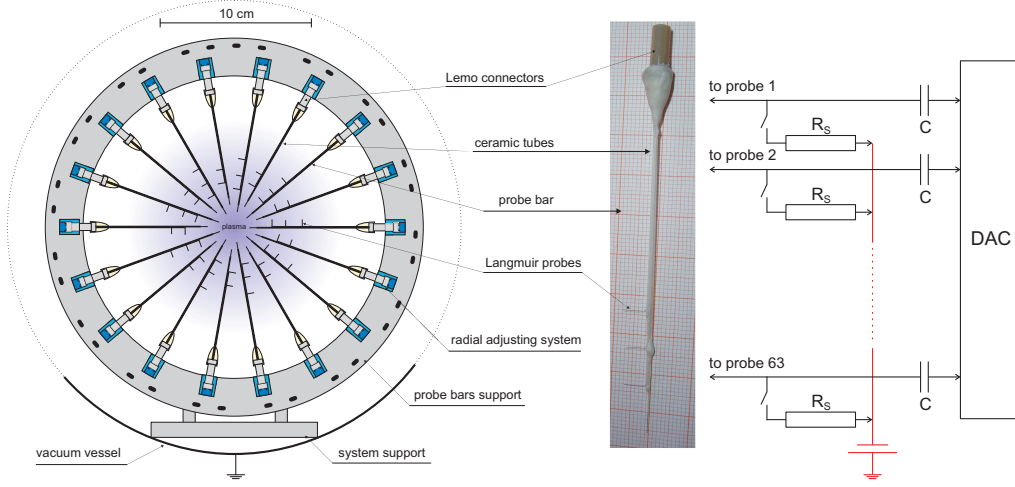


Figure 2.7: Technical sketch of the 2D probe array inside of the plasma vessel. The picture of a probe bar with 4 probes shows details of the real design. The acquisition circuit shows the possibility of both plasma potential and density fluctuations measurements by optional biasing (red line).

The PDF is usually used to characterize statistically the discrete amplitude distribution. In general it is represented by the histogram. By the PDF estimation the mean of the distribution is

$$\langle n \rangle = \int_{-\infty}^{+\infty} n \cdot P(n) dn. \quad (2.12)$$

To quantify the results of the PDF typically central moments  $m_i$  are defined as

$$m_i = \int_{-\infty}^{+\infty} (n - \langle n \rangle)^i \cdot P(n) dn = \langle (n - \langle n \rangle)^i \rangle. \quad (2.13)$$

with  $i \in [1, 2, 3, \dots]$ . It is obvious that the first moment is represented by the mean value,  $m_1 = \langle n \rangle$ . The second central moment, the variance, has a special meaning

$$m_2 = \int_{-\infty}^{+\infty} (n - \langle n \rangle)^2 \cdot P(n) dn = \langle (n - \langle n \rangle)^2 \rangle = \sigma_n^2, \quad (2.14)$$

where  $\sigma_n^2$  specifies the PDF width and is commonly used in plasma physics to measure the average fluctuation amplitude [72]. Higher central moments give information on the shape and tail of the PDF. They are used to indicate deviation of the PDF from a Gaussian.

### 2.3.2 Correlation analysis

The degree of similarity between two fluctuation quantities, e.g. the density fluctuations at two different spatial positions inside the plasma device  $n_1(x, t)$  and

$n_2(x + \Delta x, t)$ , is denoted by the cross-correlation function. Mathematically, it is computed as follows

$$C_{n_1, n_2}(\Delta x, \tau) \simeq \int_{-\infty}^{+\infty} n_1(x, t) \cdot n_2(x + \Delta x, t + \tau) dt. \quad (2.15)$$

For  $n_1 = n_2$ , the autocorrelation function is estimated. For a better comparison a normalization of the cross-correlation is needed. For this reason the geometrical average of the auto-correlation at  $\tau = 0$  and  $\Delta x = 0$  is used. Therefore,

$$R_{n_1, n_2}(\Delta x, \tau) = \frac{C_{n_1, n_2}(\Delta x, \tau)}{\sqrt{C_{n_1, n_1}(0, 0) \cdot C_{n_2, n_2}(0, 0)}} \quad (2.16)$$

is limited to  $[-1, 1]$ . Values of 1 indicate total correlated time series while by values of -1 they are anti-correlated. No correlation is indicated by values close to zero. Time lag values, corresponding to the maximum correlation, different of zero indicate time shifted series.

### 2.3.3 Spectral analysis

A standard tool to analyze the temporal behavior of a fluctuation are Fourier methods. By Fourier analysis, the fluctuation quantity, i.e. the plasma density  $n(x, t)$ , is decomposed in harmonic components

$$\hat{n}(k, \omega) = \frac{1}{\sqrt{2\pi}} \int_{-\infty}^{+\infty} n(x, t) \cdot \exp(-i\omega t) dt. \quad (2.17)$$

A useful quantity based on Fourier transformation is the auto-power spectral density is defined as

$$S(k, \omega) = \langle \hat{n}(k, \omega)^2 \rangle \quad (2.18)$$

The power is commonly given in decibel (dB) by the following transformation

$$S(k, \omega) = 10 \times \log_{10} \left( \frac{S(k, \omega)}{S_{ref}(k, \omega)} \right) \quad (2.19)$$

and represented against the frequency  $f = \omega/2\pi$  to describe the power density contribution of harmonic components.  $S_{ref}(k, \omega)$  is the reference power used for the comparison [73].

## 2.4 KIWI plasma characteristics

Although, plenty of work has been spent in the past [9, 56, 55, 54, 8, 27] for the plasma equilibrium and the fluctuation characterization, it is necessary to reinvestigate briefly them by using the new 2D positioning system. First, it has to be shown

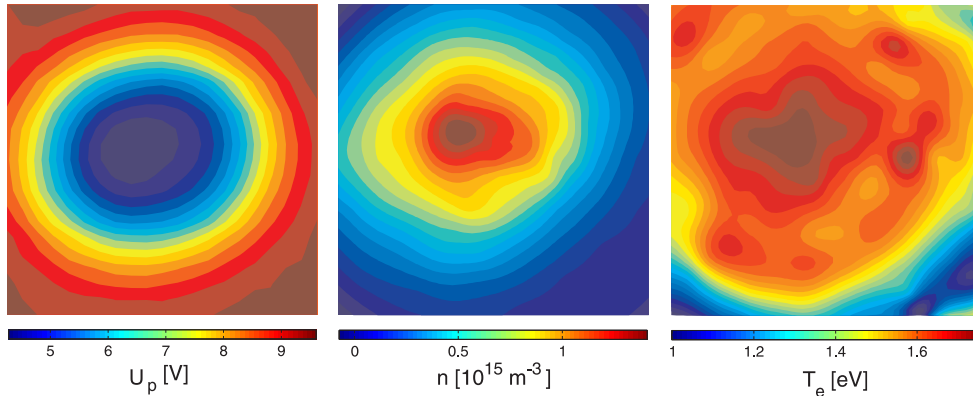


Figure 2.8: Cross-section of plasma potential, electron density and temperature. The area of  $8 \times 8$  cm is scanned with a resolution of 2 mm

that the experimental conditions remain unchanged by using this new system. Second its high spatial resolution (up to 1 mm) is used to improve the previous results. Because the plasma fluctuation dynamic is related to the equilibrium profiles of the plasma, they are investigated for one specific situation ( $U_g = 6V$ ) in detail. Dependence on grid bias is analyzed by simple 1D profiles of the plasma density and potential. Measurements on the drift waves dynamics are done in the cylindrical magnetized plasma varying of the active grid voltage.

### 2.4.1 Equilibrium profiles

To determine  $n$  and  $T_e$  probe characteristics from a Langmuir probe are analyzed. For this reason a cylindrical probe with diameter of  $100 \mu\text{m}$  and length of  $4 - 5$  mm is mounted on the 2D positioning system. The plasma potential is more accurately estimated by replacing the cylindrical probe with an emissive probe [65].  $U_p$  is determined by the floating potential  $U_f$  of the emissive probe. Typical equilibrium profiles for a grid voltage  $U_g = 6V$  are shown in Fig. 2.8. The potential profile shows always positive values having smaller values at the center of the plasma column ( $\sim 4V$ ). The electron plasma density has maximum values at the center and decays to zero close to the wall. Both profiles show a fast decay towards the wall while the temperature profile indicates almost constant values for the entire scanned area. These results reflect the cylindrical geometry of the plasma device and are in good agreement with the previous measurements [9, 54].

In the previous investigations [9], 2D equilibrium potential and density profiles along the axial plane have been investigated, Fig. 2.9. It can be seen that in the axial direction the plasma in the midsection can be divided in two regions. The first one, the area close to the active grid ( $z < 200$  mm) where the potential and radial density profiles are influenced by the fringing magnetic field lines, i.e. the density



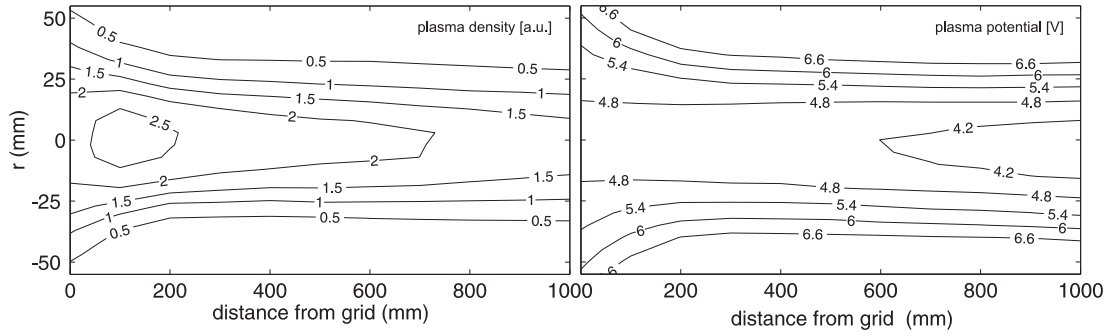


Figure 2.9: Axial plasma density and potential profiles for  $U_g = 6V$ . [Ph.D. thesis D. Block [9]]

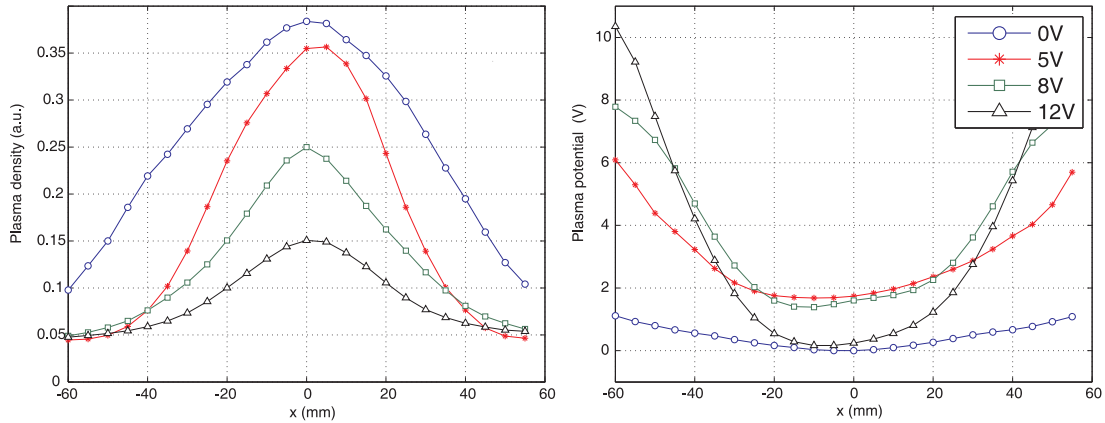


Figure 2.10: Radial plasma profiles (density and potential) in the magnetized midsection, for different values of the grid bias.

profile is broader and the equi-potential surfaces are diverging. The second one, the area far from the grid ( $z > 200$  mm) where the density and plasma have narrower and uniform profiles. The axial density gradient is caused by the axial and radial particle transport. The difference between the voltage drop seen in this profile and the voltage between separation grids (6V) is found within the shield at the grids (the sheath). Nevertheless, the remaining axial electric field can be explained by the plasma resistivity [54].

The source chamber and the midsection are connected via the biased grid. The influence on the grid voltage on the plasma profiles in the magnetized midsection has already been investigated in detail, [54]. But, to understand the next section it is necessary to briefly reinvestigate this influence. For this reason 1D profiles of plasma density and plasma potential at the plasma center in the midsection are analyzed, Fig. 2.10. Here the plasma density and potential values are subtracted in the similar way as for 2D profiles. For this profiles only the central plasma region (120 mm) of the midsection (300 mm diameter) is 1D scanned with 5 mm resolution.

Fig. 2.10 indicates that the grid voltage has a significant influence on both density and potential of the plasma. By increasing the grid bias a lower plasma density and steeper electric field are obtained in the magnetized midsection. In principle, the density peak depends on the grid bias, but the profile does not change significantly in shape for  $U_g > 0V$ .

The radial potential gradients of about  $\sim 300V/m$  (Fig. 2.10) cause azimuthal  $E \times B$ -drifts. They are the main destabilizing mechanism for the drift waves in KIWI experiment [74]. A previous analysis of plasma potential profiles in KIWI has shown that at the central plasma region it can be fitted by a simple parabola [54]. Using this assumption, the  $E \times B$ -velocity can be written as

$$\vec{v}_{E \times B} = -\frac{\nabla U_p \times \vec{B}}{B^2} = \kappa \cdot \frac{r}{B} \cdot \vec{e}_\Theta \quad (2.20)$$

where  $\kappa$  is a constant and  $\vec{e}_\Theta$  the azimuthal unit vector. Thus, the rotation frequency ( $\omega_{E \times B} = \frac{v_{E \times B}}{r}$ ) caused by  $E \times B$  drift is independent of the radial position  $r$ . Therefore the  $E \times B$  rotation of the plasma column is radially unshered, i.e. the plasma can be regarded as a rotating solid body.

A Gaussian fitted to plasma density profile, Fig. 2.10, shows excellent agreement [54]. Based on this the diamagnetic drift velocity is given by

$$\vec{v}_D = -\frac{\nabla p_e \times \vec{B}}{enB^2} = C \cdot r \cdot T_e \cdot \vec{e}_\Theta \quad (2.21)$$

where  $C$  is again a constant. By justified assumption of radially constant temperature, Fig. 2.8, the electron diamagnetic drift velocity depends only on  $r$ . Hence, the corresponding drift frequency  $\omega_D$  is independent on radius, i.e. the drift is radially unshered. The plasma diffusion in the midsection depends on grid bias, so, the main velocities will only depend on grid voltage [55, 54]. For this reason the grid voltage is used as the main parameter to destabilize drift waves in the magnetized midsection.

## 2.4.2 Plasma fluctuations

The previous work on KIWI, [8, 55, 54] has shown that fluctuations can be observed only for certain discharge parameters, see Tab. 2.1. As already mentioned in the last paragraph, the most used parameter to control the occurrence of fluctuations and their dynamics is the grid voltage  $U_g$ . The influence of this parameter on equilibrium plasma profiles has been discussed in many papers, [8, 54]. It was shown that by increasing the grid voltage (0V–14V) the plasma fluctuation follows a Ruelle-Taken-Newhouse scenario from stable fluctuations (regular drift waves), at low  $U_g$ , to weak turbulence (multi mode states) at higher grid bias [75, 76]. In Fig. 2.11 the specific KIWI plasma fluctuation transition scenario is depicted by density fluctuation

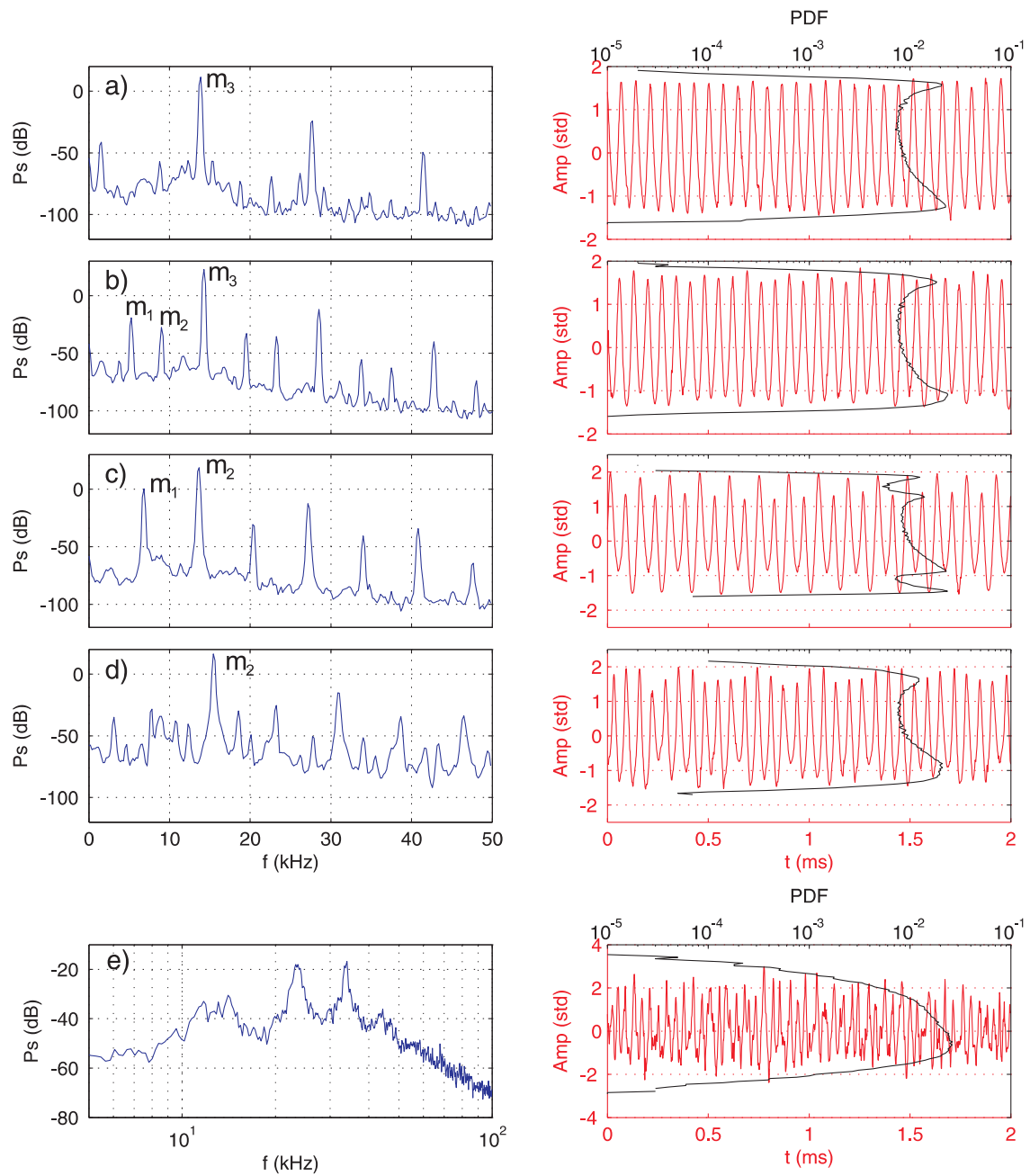


Figure 2.11: Time series, signal PDF (left) and power spectrum (right) of the density fluctuations for increasing grid voltage. The control grid voltage: (a)  $U_g = 4V$ , (b)  $U_g = 5V$ , (c)  $U_g = 6V$ , (d)  $U_g = 8V$ , (e)  $U_g = 12V$ . At the last situation the power spectrum is represented in double logarithmic scale.

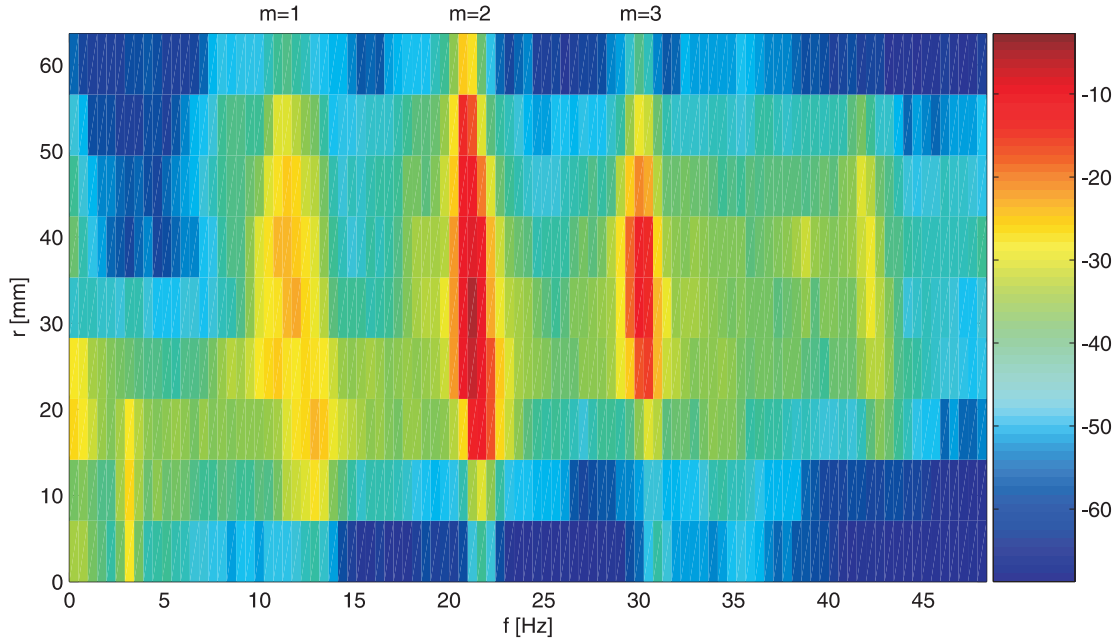


Figure 2.12: The radial power spectra distribution of the density fluctuation. This graphic shows the case of a weak turbulence (multi mode) state ( $U_g=11V$ ).

spectra and PDFs. The plasma density fluctuations are obtained by recording the ion saturation fluctuations with a Langmuir probe, localized in the area of steepest gradients. First fluctuations are observed at  $U_g = 4$  V where the frequency spectra is sharply peaked at the frequency  $f = 16$  KHz corresponding to mode  $m=2$ <sup>1</sup>, and their higher harmonics, Fig. 2.11a. By slightly increasing of the grid bias  $U_g = 5V$  (Fig. 2.11b), the single mode situation is destabilized and additional drift modes are introduced. By a further increase of  $U_g$  the mode number changes to  $m=2$  for  $U_g = 7.8V$  (Fig. 2.11d). The time series of the density fluctuations show a slight increase of amplitude level with the grid bias. The weak turbulence state with strongly irregular, intermittent density fluctuations and a broad, noise-like spectrum is found at high grid voltages ( $U_g \simeq 12V$ ), Fig. 2.11e.

The observed fluctuations of turbulence state can be identified as drift modes by analyzing also the spectral radial distribution of density fluctuations as in Fig. 2.12. The theoretical predicted radial distribution of the eigenmode structure [77] with the mode peaks slightly shifted radially outwards, are clearly observed in the experiment. They indicate also the fluctuation maximum close to the position of maximum density gradient (Fig. 2.10). The frequency range is also in good agreement with theory and previous experimental findings [8, 55]

<sup>1</sup>Details about mode number computation are presented in the chapter 8.

## 2.5 Summary

In this chapter the technical details of the KIWI experiment have been summarized. The new diagnostic tools used in this work have also been presented. Furthermore, the equilibrium profiles and the transition route from the drift wave to the weak turbulence have been reinvestigated. It has been shown that the propagation of the azimuthal drift waves is radially unshaped, i.e. the  $E \times B$  rotation of the plasma column and the diamagnetic electron drift are found to be unshaped. The active grid bias controls drift wave dynamics in the magnetized midsection.

If the temporal dynamics of the turbulence can be characterized by the simple spectral analysis, its spatial evolution requires multi-points measurements. To gain insight into the complex situation of the turbulence (multi mode state), spatio-temporal measurements with high resolution are required. This can be achieved using 2D probe array measurements and statistical techniques, i.e. conditional averaging and cross-correlation techniques. The performance of multi probe measurements and statistical analysis is the subject of the next chapters. The global monochromatic drift modes with their spatial and temporal structures, which are now well understood will allow us to investigate the capability of this techniques.



# Chapter 3

## Conditional averaging technique

This chapter concentrates on the technical description of conditional averaging (CA) technique. For a better understanding, an analytical model of this method, which incorporates the trigger condition aspects, is proposed. Prospects and limitations of the standard CA method are further analyzed on synthetic data and compared with analytical results. Particularly, the influence of the trigger condition on quality of conditional averaging is discussed in detail.

### 3.1 Technical description of standard CA method

Conditional averaging or conditional sampling is the most common statistical technique used for spatio-temporal diagnostic of the plasma fluctuation. It is a powerful tool used for coherent structure detection in turbulence [27, 48, 78, 79]. The basic idea of the method is the following: in general any fluctuating signal  $f(x, t)$  can be split into three components, a time-independent fraction  $f(x)$ , a fraction  $f_{coh}(x, t)$  containing all coherent fluctuations, and a fraction  $f_r(x, t)$  for the incoherent fluctuations.  $f(x)$  is easily removed by subtracting the time-average of  $f(x, t)$ . From the remaining time-dependent part  $\tilde{f}(x, t) = f_{coh}(x, t) + f_r(x, t)$ , the coherent fluctuations  $f_{coh}(x, t)$  can be extracted by means of an ensemble average over many independent realizations of  $\tilde{f}(x, t)$ , i.e.

$$\langle \tilde{f}(x, t) \rangle = \langle f_{coh}(x, t) + f_r(x, t) \rangle = \langle f_{coh}(x, t) \rangle + \langle f_r(x, t) \rangle = f_{coh}(x, t). \quad (3.1)$$

$\langle \cdot \rangle$  indicates the ensemble average and  $\langle f_r(x, t) \rangle$  vanishes due to its incoherence.

Although, this is a mathematically simple procedure, the problem remains how to obtain such an ensemble of independent realizations. A solution was proposed by Kaplan and Laufer [78] and Kovasznyai, Kibens and Blackwelder [79]. Their method of conditional averaging uses a trigger condition to detect large scale structures. Whenever the trigger condition  $f_c$  is met a realization of  $\tilde{f}(x, t)$  is recorded, i.e.

$$\langle \tilde{f}(x, t) \rangle_{ca} = \langle \tilde{f}(x, t) | f(x, t = 0) = f_c \rangle. \quad (3.2)$$

Little later, Adrian [48] showed that the conditional averaged signal  $\langle \tilde{f}(x, t) \rangle_{ca}$  is the best estimate of  $f_{coh}(x, t)$ , because it minimizes the least square error. A key issue for the success of conditional averaging is the proper choice of the trigger condition. On the one hand, the trigger condition has to be characteristic for the large scale structures. This assures that only these structures cause trigger events. On the other hand, the trigger condition should not be too specific to assure that a large number of structures is detected to allow for a statistical treatment. To resolve this difficulty, the method of stochastic estimation was proposed [48, 80]. It bases on the fact that the conditional average can be written as a series expansion containing spatio-temporal correlation functions. The benefit is that conditional statistics can be estimated by unconditional statistics. Some nice results have been obtained [81, 82, 83, 84] but unfortunately the convergence of the series expansion could not be shown for arbitrary signals. This leaves us with the initial problem of a proper trigger condition. The most simple trigger condition is a threshold. However, the commonly used trigger condition combines a threshold with the sign of the first derivative.

The common CA setup consists of two probes which simultaneously record a pair of time series ( $f_{RP}$  and  $f_{MP}$ ). One probe, called reference probe (RP), is maintained at a fixed position while the moveable probe (MP) scans an area of interest in the plasma device. The typical procedure of CA requires that an event in the signal of the reference probe,  $f_{RP}(t)$ , lies within a prescribed amplitude interval and has a positive (negative) slope. Every time when these trigger conditions are fulfilled a short sub-series (sequence)  $f_{MP,k}(t^*)$  with  $t^* \in [t_k + \tau - \Delta, t_k + \tau + \Delta]$  is selected from the time series,  $f_{MP}(t)$  at the moveable probe (Fig.3.1).  $\Delta$  specifies the length of the sub-series and is usually taken to be of the order of the correlation time of the signal.  $\tau$  is a time delay which considers the propagation of the detected structure from  $x_{RP}$  to  $x_{MP}$ . The sub-series  $f_{MP,k}(t^*)$  can be considered as independent if the additional condition  $t_{k+1} - t_k > 2\Delta$  is fulfilled, i.e. the sub-series are not allowed to overlap. Finally, the CA-result is calculated by averaging over all sub-series  $f_{MP,k}(t^*)$ . Formally, this reads

$$\langle f_{MP}(t^*) \rangle_{ca} = \langle f_{MP,k}(t^*) \mid f_{c1} \leq f_{RP}(t_k) \leq f_{c2} \wedge \partial_t f_{RP}(t_k) \geq 0 \rangle. \quad (3.3)$$

with  $f_{c1}$  and  $f_{c2}$  denoting the lower and upper bound of the trigger window. The desired spatio-temporal resolved conditional average is obtained by repeating the above described procedure for various position of the moveable probe in a 2D plane. The obvious advantage is that spatio-temporal conditional averages of high spatial and temporal resolution can be obtained with only two probes.

## 3.2 Analytical modeling of CA

The above described conditional averaging procedure can be modeled with a few assumptions on the signal  $\tilde{f}(x, t)$ . The aim of this model is to find an expression for



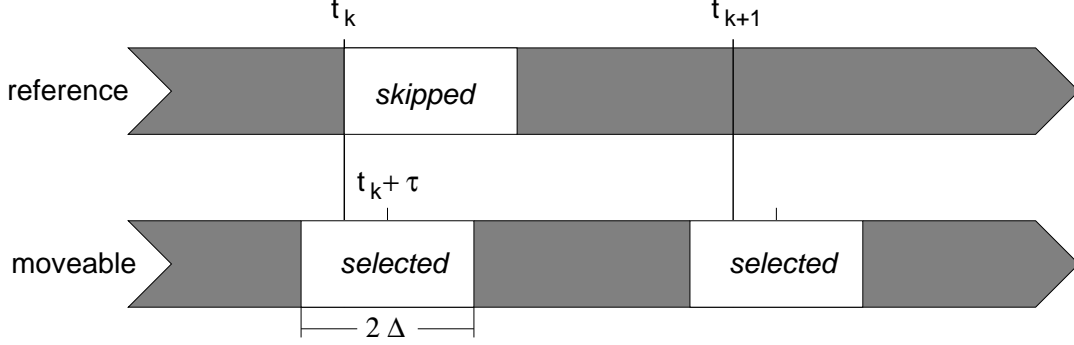


Figure 3.1: Experimental realization of CA. Each time  $t_k$  the reference signal fulfills the trigger condition, a sequence centered about  $t_k + \tau$  is taken from the moveable probe signal. The minimum distance between two sequences is set to  $2\Delta$  to assure statistical independence.

$\langle \tilde{f}(x, t) \rangle_{ca}$  which just depends on statistical properties of  $\tilde{f}(x, t)$ . For this purpose, the probability to find a trigger event at time  $t_k$  has to be investigated first. Let  $P(\tilde{f}(x, t))$  be the probability distribution function of  $\tilde{f}(x, t)$  with

$$\int_{-\infty}^{\infty} P(\tilde{f}(x, t)) d\tilde{f} = 1. \quad (3.4)$$

In this case, the probability that  $\tilde{f}(x, t)$  exceeds a given threshold  $f_c$  at any time  $t_k$  is

$$p_t(x, t_k) = \int_{f_c}^{\infty} P(\tilde{f}(x, t_k)) d\tilde{f}. \quad (3.5)$$

Using  $\tilde{f}(x, t_k) = f_{coh}(x, t_k) + f_r(x, t_k)$ , this can be rewritten as

$$p_t(x, t_k) = \int_{f_c - f_{coh}(x, t_k)}^{\infty} P(\tilde{f}_r(x, t_k)) d\tilde{f}, \quad (3.6)$$

i.e. the probability to find a trigger event at time  $t_k$  is just the probability that the incoherent fluctuations are large enough to exceed the difference between  $f_c$  and  $f_{coh}(x, t_k)$ . In case of a trigger window this is readily modified to

$$p_w(x, t_k) = \int_{f_{c1} - f_{coh}(x, t_k)}^{f_{c2} - f_{coh}(x, t_k)} P(\tilde{f}_r(x, t_k)) d\tilde{f}. \quad (3.7)$$

If an additional condition is imposed on the first derivative of  $\tilde{f}(x, t)$ , e.g.  $\tilde{f}(x, t_k + 1) \geq f_{c2}$ , equation 3.7 has to be modified further. With the assumption that  $f_r(x, t_k)$  and  $f_r(x, t_k + 1)$  are statistically independent, i.e. that the probability to find a

trigger event at  $t_k$  is given by the product of the probabilities to fulfill both trigger conditions, we obtain:

$$p_d(x, t_k) = p_w(x, t_k) \int_{f_{e2}-f_{coh}(x, t_k)}^{\infty} P(\tilde{f}_r(x, t_k + 1)) d\tilde{f}. \quad (3.8)$$

Further, a constraint on non-overlapping sequences has to be added to the model, i.e. only one trigger event is allowed per sequence. To fulfill the trigger conditions at  $t_k$ , it is necessary, that there has not been a trigger event within  $N$  time steps before (with  $\Delta \equiv N$  time steps). Consequently, the probability for a trigger event has to be written as

$$p(x, t_k) = p_d(x, t_k) \prod_{j=1}^N (1 - p_d(x, t_k - j)). \quad (3.9)$$

The probability to find a trigger event at  $t_k$  is the product of all probabilities of the  $N$  time steps before  $t_k$ , that no trigger event occurred times the probability that it is fulfilled at  $t_k$ .

Knowing  $p(x, t_k)$ ,  $\langle \tilde{f}(x, t^*) \rangle_{ca}$  can be calculated. According to its definition

$$\langle \tilde{f}(x, t^*) \rangle_{ca} = \frac{1}{M} \sum_{k=1}^M f_{mov,k}(x, t^*) \quad (3.10)$$

with  $t^* \in [t_k + \tau - \Delta, t_k + \tau + \Delta]$ . Using  $p(x, t_k)$  the sum of all trigger events can be rewritten as a sum of the trigger probability at each point in the time interval  $t^*$  times the coherent signal fraction  $f_{coh}$ . Let us assume for a moment that all detected subsequences contain some fraction of  $f_{coh}(x, t)$  and that  $\tau = 0$ . In this case, we obtain

$$\langle \tilde{f}(x, t^*) \rangle_{ca} = \frac{\sum_{j=-N}^N p(x, t_k + j) f_{coh}(x, t_k + j)}{\sum_{j=-N}^N p(x, t_k + j)}. \quad (3.11)$$

Hence, if  $f_r(x, t) = 0$ ,  $p(x, t_k + j)$  would be zero except for one time step  $t_k$ , which is defined by the trigger condition, where it is one (if the trigger condition can be satisfied at all). The sum in the numerator would therefore be just  $f_{coh}(x, t_k)$ . As soon as  $f_r(x, t) \neq 0$ ,  $p(x, t_k + j)$  has finite values for any time step  $t_k + j$ , i.e.  $f_r(x, t)$  introduces a jitter to the trigger positions (Fig. 3.2). Its influence on  $\langle \tilde{f}(x, t^*) \rangle_{ca}$  is described by Eq. 3.11. However, despite of this trigger jitter there is a finite probability  $p_{err}(x, t_k)$  that trigger events occur even if there is no coherent structure within  $N$  time steps distance of  $t_k$ , i.e.  $f_{coh}(x, t_j) = 0$  for  $j \in [1, 2N + 1]$ . In this case the trigger condition has to be fulfilled solely by  $\tilde{f}_r(x, t_k)$ . In the following these events are called false trigger events. Combining  $f_{coh}(x, t) = 0$  and equation (3.8),  $p_{err}(x, t_k)$  can be calculated analogous to equation (3.9). With  $\langle \tilde{f}_r(x, t^*) \rangle_{ca} = 0$  by

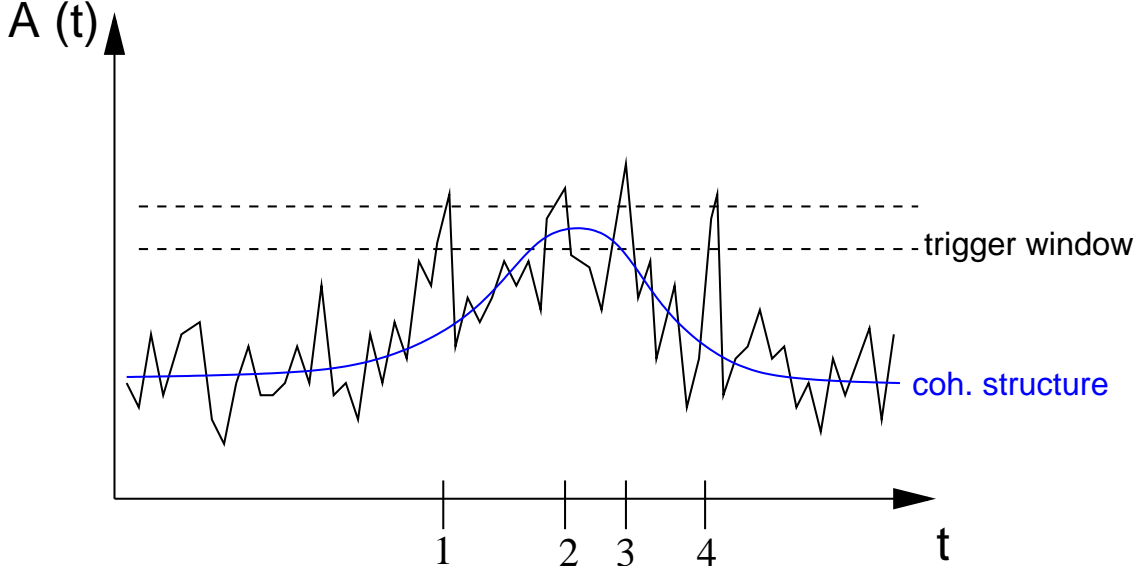


Figure 3.2: Adding noise to a well defined coherent structure introduces a trigger jitter to the conditional averaging process. The numbers mark positions within one sequence where the trigger conditions is fulfilled. Note that the trigger position for the noise free coherent signal is not among them.

definition, false trigger events will introduce an additional damping of  $\langle \tilde{f}(x, t^*) \rangle_{ca}$  and equation 3.11 is extended to

$$\langle \tilde{f}(x, t^*) \rangle_{ca} = \frac{\sum_{j=-N}^N p(x, t_k + j) f_{coh}(x, t_k + j)}{\sum_{j=-N}^N p(x, t_k + j)} [1 - M_{err}]. \quad (3.12)$$

with  $M_{err}$  being the relative number of false trigger events compared to the number of trigger events related to coherent fluctuations. An estimate for  $M_{err}$  is given by

$$M_{err} = \left(1 - \frac{M_{coh}}{M}\right) \sum_{j=1}^{2N+1} p_{err}(x, t_k) \quad (3.13)$$

with  $M$  being the maximum number of sequences that can be placed within the recorded time series and  $M_{coh}$  being the number of coherent structures.

Up to now, it has been assumed that a trigger at  $t_k$  implies that there has been no trigger event within  $N$  time steps before, i.e.  $2N$  time steps are needed to calculate Eq. 3.11 or 3.12. For a well posed trigger condition this is usually fulfilled. However, if  $p_{err}(x, t_k)$  is not small or if the coherent structures occur frequently, trigger events are often, i.e. the average number of time steps between trigger events will approach  $2N$  (see Fig. 3.1). A trigger event at  $t_{k+1} = t_k + 2N + 1 + i$  has the probability

$$p(x, t_{k+1}) = p_d(x, t_{k+1}) \prod_{j=1}^{\min(i, N)} (1 - p_d(x, t_{k+1} - j)). \quad (3.14)$$

because the interval  $[t_k, t_k + 2N]$  is not tested for trigger events and hence  $p_d(x, t) = 0$  for all points inside this interval. However, for a well posed trigger condition,  $p_d(x, t)$  is close to zero everywhere except for positions very close to a coherent structure and therefore Eq. 3.14 is a good estimate for  $p(x, t_k)$  as well.

Finally, it has to be noted that Eq. 3.12 would only be identical to the experimentally obtained conditional average in the limit of an infinite number of sequences used for the averaging process. For a finite number of sequences  $M$ ,  $\langle \tilde{f}_r(x, t^*) \rangle_{ca}$  will not vanish and the remaining noise level  $\delta f_{ca}$  of  $\langle \tilde{f}(x, t^*) \rangle_{ca}$  can be estimated by

$$\delta f_c = \sigma_r \sqrt{M} \quad (3.15)$$

with  $\sigma_r$  being the standard deviation of  $\tilde{f}_r(x, t)$ .

### 3.3 Prospects and limitations of CA

To test whether the analytic prediction of  $\langle \tilde{f}(x, t^*) \rangle_{ca}$  which incorporates the influence of the trigger condition, is a good description for the conditional averaging process, it is compared with the CA results on well defined synthetic data. For this synthetic data sets of coherent structures embedded in gaussian noise are generated from the computer. The influence of the trigger condition on the quality of the conditional average will be discussed and compared with analytical model results.

#### 3.3.1 Synthetic data

To produce a conditional average from synthetic data, time series with a length of  $10^6$  samples and Gaussian distributed noise are generated. 500 coherent structures are added to this time series at equally distributed random positions with the only restriction that structures are not allowed to overlap, i.e. structures have a minimum distance of 200 samples. To model the coherent part of the signal  $f_{coh}$  is assumed to be a Gaussian. Note that this choice does not affect the following results. Any smooth function would yield similar results. The sequence length is set to  $2\Delta = 200$  samples and is about five times longer than the size of the coherent structure. This means that the total time series can be splitted into 5000 sequences at maximum. This is one order of magnitude higher than the number of coherent structures placed in the time series. Hence, for a well proposed trigger condition Eq. 3.14 should give a reasonable description of the conditional average. All other parameters are varied systematically. In the following, their values are normalized to the noise level  $\sigma_r$ .

### 3.3.2 Results and comparison

To investigate the impact of the trigger condition on the CA result, the synthetic data is analyzed using the standard CA procedure as described in section 1. For this purpose the trigger condition uses an amplitude threshold in combination with a positive slope and a trigger window. For Gaussian distributed noise ( $\tilde{f}_r(x, t)$ ) with a standard deviation  $\sigma_r = 1$ , Eq. 3.6, 3.7, and 3.8 simplify to

$$p_t(x, t_k) = \frac{1}{2} \operatorname{erfc} \left[ \frac{f_c - f_{coh}(x, t_k)}{\sqrt{2}} \right], \quad (3.16)$$

$$p_w(x, t_k) = \frac{1}{2} \operatorname{erfc} \left[ \frac{f_{c1} - f_{coh}(x, t_k)}{\sqrt{2}} \right] - \frac{1}{2} \operatorname{erfc} \left[ \frac{f_{c2} - f_{coh}(x, t_k)}{\sqrt{2}} \right], \quad (3.17)$$

$$p_d(x, t_k) = p_w(x, t_k) \frac{1}{2} \operatorname{erfc} \left[ \frac{f_{c2} - f_{coh}(x, t_k + 1)}{\sqrt{2}} \right]. \quad (3.18)$$

To quantify the results the main structure properties: structure amplitude and structure size are considered for analysis.

#### Structure amplitude

Fig. 3.3 shows three typical results for small ( $A_{coh} = 1.4\sigma_r$ ), medium ( $A_{coh} = 3\sigma_r$ ) and large ( $A_{coh} = 5\sigma_r$ ) amplitudes of the coherent structures. The blue line is the conditional average and the filled circles mark the analytic result. The conditional average is obtained by using a trigger window of ( $2\sigma_r < f_c < 2.2\sigma_r$ ). In all cases the analytic model reproduces the conditional average. This is a first indication that the analytic model gives a good description of the conditional averaging process. Furthermore, all plots show that the obtained amplitude of the conditional average is significantly lower than the amplitude of the original coherent structure. This amplitude reduction by a factor of 3 to 4 is found in all plots as well as an almost constant noise level of the conditional average.

To investigate this behavior in more detail, Fig. 3.4 shows the amplitude of the conditional average as a function of the trigger level. The amplitude of the original coherent structure is indicated by the dashed line ( $A_{coh} = 3\sigma_r$ ). The results of the conditional averaging process are indicated by dots and the solid line shows the prediction of the analytic model. Both are in good agreement. Obviously, the amplitude  $3\sigma_r$  is only resolved for trigger levels higher than  $2.5\sigma_r$ . For lower trigger levels a significant amplitude reduction is observed. However, for high trigger levels the deviation of the conditional average from the analytic results is large and the spread in amplitude increases significantly. Fig 3.5 shows the event statistics of Fig. 3.4. The solid line is again the result of the analytic model while the dots represent the conditional average of the synthetic data. The dashed line (analytic model) and the crosses (synthetic data) indicate the number of false trigger events. First of all, a good agreement is found between the model and the conditional

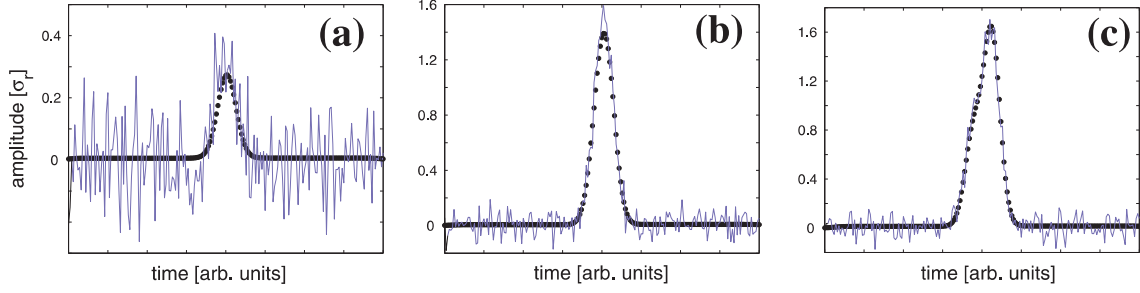


Figure 3.3: Comparison of conditional averaged synthetic data (blue line) and the analytic prediction (dots). All plots refer to conditional averages using a trigger window ( $2\sigma_r < f_c < 2.2\sigma_r$ ) and a positive slope as trigger conditions. The amplitude of the original coherent structures is (a)  $A_{coh} = 1.4\sigma_r$ , (b)  $A_{coh} = 3\sigma_r$ , and  $A_{coh} = 5\sigma_r$ .

average. Second, the plot shows that the number of correctly detected coherent structures has a maximum at a trigger level of about  $2\sigma_r$ . For higher trigger level the number decreases and already at  $f_c = 3\sigma_r$  only half of the structures are found. Additionally the number of false trigger events is very high for trigger level  $f_c < 2\sigma_r$ . Hence, the amplitude damping observed in Fig. 3.4 is caused by the dominance of the false trigger events in the averaging process. For high trigger level the number of false trigger events vanishes but the number of detected structures decreases as well. The result is a poor statistic, i.e. averaging process almost fails and the conditional average signal still contains a strong noise component. Only for a small range of trigger levels ( $2\sigma_r < f_c < 3\sigma_r$ ) the number of false trigger events is smaller than the number of detected structures and the overall number of events is still high enough for a reasonable statistic. From these results it can be concluded that high trigger levels are needed to avoid a high number of trigger errors and that very long time series are needed to achieve a reasonable trigger statistics.

### Structure size

Fig. 3.6 shows the amplitude of the conditional average as a function of the amplitude of the original coherent structure for a fixed trigger level ( $2\sigma_r < f_c < 2.2\sigma_r$ ). The solid line and the dots are the results of the analytic model and the conditional averaging process, respectively. The dashed line is given as reference and marks the true amplitude of the coherent structure. Fig. 3.7 shows the corresponding event statistic. Again, the model description reproduces the results of the conditional averaged synthetic data. The results show that only structures with amplitudes significantly higher than the noise level are reproduced with reasonable amplitude (Fig. 3.6). Only for structures with amplitudes  $A_{coh} > 2\sigma_r$  the number of correctly detected structures exceeds the number of false trigger events (Fig. 3.7). The best ratio is obtained for structures with  $A_{coh} \approx 3\sigma_r$ . This coincides with the position

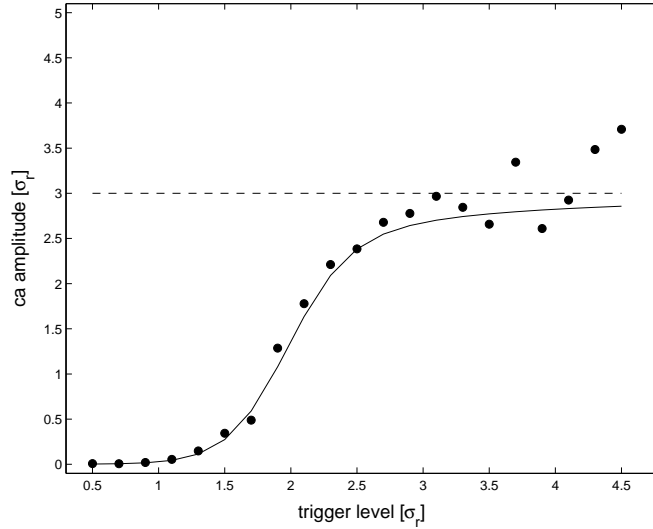


Figure 3.4: Comparison of the detected maximum amplitude of conditional averaged synthetic data (dots) and the analytic prediction (solid line) as a function of the imposed trigger level. The dashed line refers to the amplitude of the original coherent structure ( $A_{coh} = 3\sigma_r$ ). The conditional averages are obtained for a trigger window with a width of  $\Delta f_c = 0.2\sigma_r$  and a positive slope as trigger conditions. The trigger level in the plot specifies the lower boundary of the trigger window.

of the maximum amplitude for the conditional average in Fig. 3.6. The general amplitude reduction with respect to the original amplitude of the coherent structures is again related to the number of false trigger events (see Fig. 3.5 and 3.7). The additional amplitude reduction for large structures is caused by the trigger condition. For the results shown here the structure amplitude has been varied but the width of the structure was kept constant. Therefore, high amplitude structures have a smaller probability to fulfill the rather restrictive trigger condition ( $\Delta f_c = 0.2\sigma_r$ ) as the trigger window is set to regions with a steep slope. However, similar results are found for other trigger conditions and hence it can be stated that conditional averaging is not sensitive for small amplitude structures and that the introduction of a trigger window acts like an amplitude filter to a certain extent.

Nevertheless, one has to keep in mind that the structure amplitude is not the same as the structure size, as illustrated in Fig. 3.8. A structure with a given size  $s$  will produce a time trace with a width  $\Delta t$  which is proportional to the ratio of structure size and its velocity  $v$ . Hence, a smaller structure with a lower velocity can have the same time trace if the ratio  $s/v$  is the same. This means that conditional averaging based on a single reference probe can only be size sensitive if structures move faster with decreasing size. Unfortunately, this assumption will not hold in general. Combined with the rather poor filter characteristic of the trigger conditions (Fig. 3.6) it has to be stated that conditional averaging is able to extract large amplitude structures from a noisy background and that a scale sensitivity can not

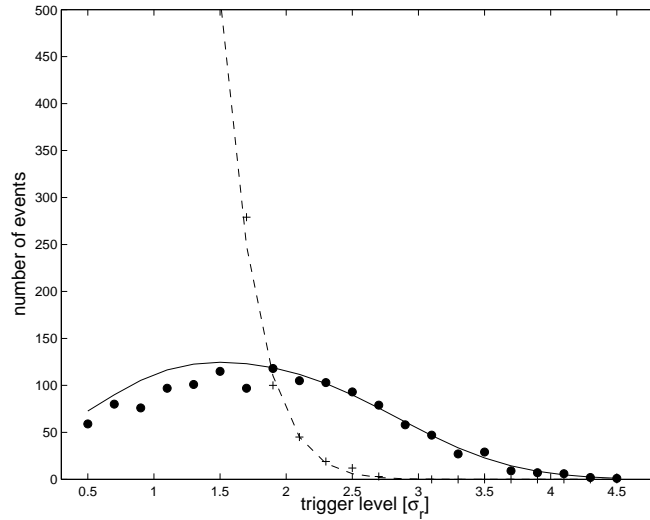


Figure 3.5: Event statistics for the trigger level scan shown in Fig. 3.4. The dots shows the number of correctly detected coherent structures obtained by conditional averaging of synthetic data. The solid line is the corresponding prediction from the analytic model. The dashed line shows the number of false trigger events estimated by the analytic model. The crosses mark the corresponding results from the synthetic data.

be achieved with a single reference probe setup. However, with the reasonable assumption that high amplitudes are in general a signature of large structure size the sensitivity on large amplitudes would provide a limited size sensitivity of conditional averaging.

### 3.4 Correlation analysis of CA-results

The detailed analysis on the structure amplitude from the previous section has shown that the conditional averaging process introduces a significant amplitude reduction to the data. Two typical scenarios have been distinguished by synthetic data analysis [85]:

- (1) a coherent structure is recorded with a time shift due to noise (trigger jitter).
- (2) noise causes a trigger event without any coherent structure being involved (trigger error).

It was shown that both effects contribute to the amplitude damping of the detected coherent structures. In order to identify the origin of the amplitude damping this section introduces a correlation analysis of the CA-results to identify trigger errors and to estimate trigger jitter. The basic idea behind this is simple. If the CA analysis allows to observe some structures it is possible to use the CA-structures as a first estimate for the real structures. If one now computes the cross-correlation function



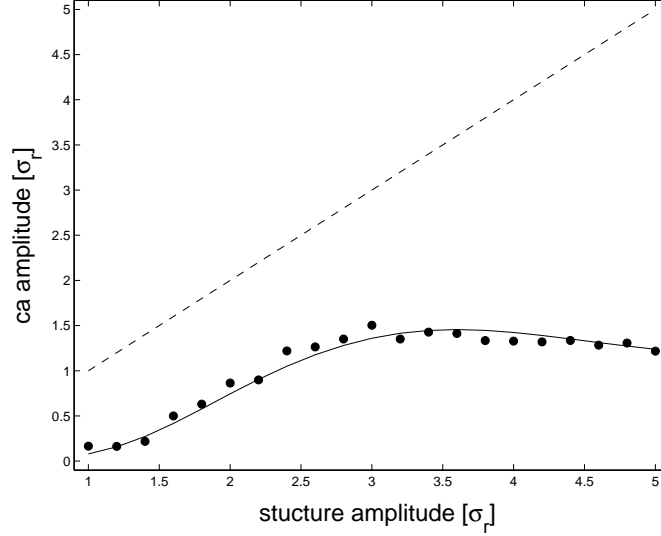


Figure 3.6: Comparison of the detected maximum amplitude of conditionally averaged synthetic data (dots) and its analytic prediction (solid line) as a function of the amplitude of the coherent structure. The dashed line refers to the amplitude of the original coherent structure. The conditional averages are obtained for a trigger window ( $2\sigma_r < f_c < 2.2\sigma_r$ ) and a positive slope as trigger conditions.

(CCF) between CA-result and all selected sub-series on RP and MP signal respectively, it should be possible to identify and remove those events which cause the amplitude damping. The CCF is computed by

$$CCF(\tau) = \int \langle f_P(x_P, y_P, t^*) \rangle_{ca} f_{P,k}(x_P, y_P, t^* + \tau) dt^*, \quad (3.19)$$

where  $P$  is either RP or MP,  $k = 1, 2, \dots, n$  ( $n$  is total number of events) and  $t^* \in (t_k - \Delta, t_k + \Delta)$ . A detailed sketch of the correlation analysis is depicted in Fig. 3.9. By applying the trigger condition (here, trigger level = 2), the subseries are selected from the main time series (i.e. #1, #2, #3). Their average leads to a smooth CA result. Further, by computation of CCF between all selected time series and CA result will allow to judge whether the signal in the sub-series is similar to the CA-result or not. This means that without an a-priori knowledge of the structure properties, the correlation analysis allows to identify those subseries which have low correlation values, i.e. those who are likely to be trigger errors. Furthermore, the timelag  $\tau_{max}$  (here,  $\tau_1$ ,  $\tau_2$  and  $\tau_3$ ) of maximum correlation is a measure for trigger jitter. Typical for a trigger jitter are high CCF values with  $\tau_{max} \neq 0$ , i.e. noise that causes a trigger close to a coherent structure ( $\tau_2$ ). The crucial point is how one can define a robust criterion for high and low correlation or for trigger jitter. The definition of "high" and "low" correlation is certainly difficult as it might vary for different experiments and even different spatial positions. A criterion on trigger jitter is much easier as we will show in the following chapter.

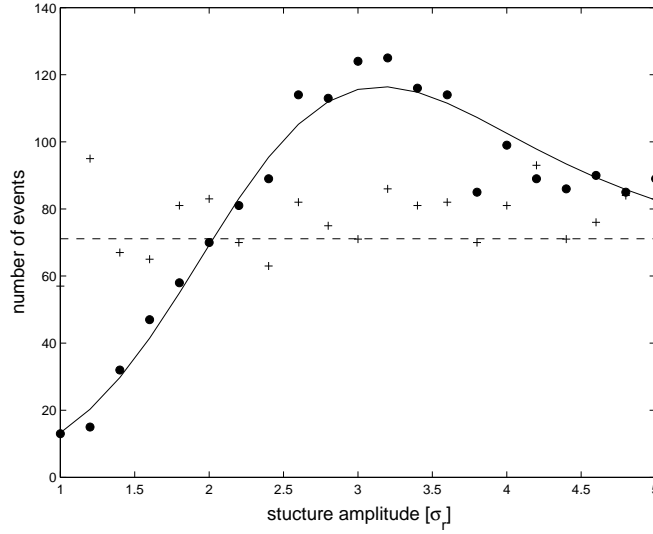


Figure 3.7: Event statistics for the amplitude scan shown in Fig. 3.6. The dots show the number of correctly detected coherent structures obtained by conditional averaging of synthetic data. The solid line is the corresponding prediction from the analytic model. The dashed line shows the number of false trigger events estimated by the analytic model. The crosses mark the corresponding results from the synthetic data.

### 3.5 Summary and remarks

The advantages and limitations of conditional averaging technique for spatio-temporal plasma diagnostic, has been in detail discussed in this chapter. On one hand its computational simplicity and high spatial and temporal resolution obtained by using just two probes are advantages of the technique. On the other hand, the accuracy of the result depends on the proper choice of the trigger condition. Only a trigger condition which is specific for the coherent structures assures that only coherent events are selected. Unfortunately, such a specific trigger condition is difficult to define as it requires a-priori knowledge of the coherent structures, e.g. their shape [86]. It happens that the trigger condition is fulfilled with a certain probability by other signals as well. By means of a detailed comparison of the model predictions and conditional averaged synthetic data, it was shown that the conditional averaging process introduces a significant amplitude reduction to the data. The reason for this amplitude reduction are trigger errors, i.e. false trigger events that are caused by the background noise without any coherent signal being involved, and the trigger jitter, i.e. time-shifted coherent events due to the background noise. This is a crucial issue for the estimation of the structures contribution to anomalous transport. As a consequence the results of CA can only be taken as a lower bound for a transport estimation. Further, the comparison showed that conditional averaging is not sensitive with respect to structure size. In general, only large amplitude fluctuations are

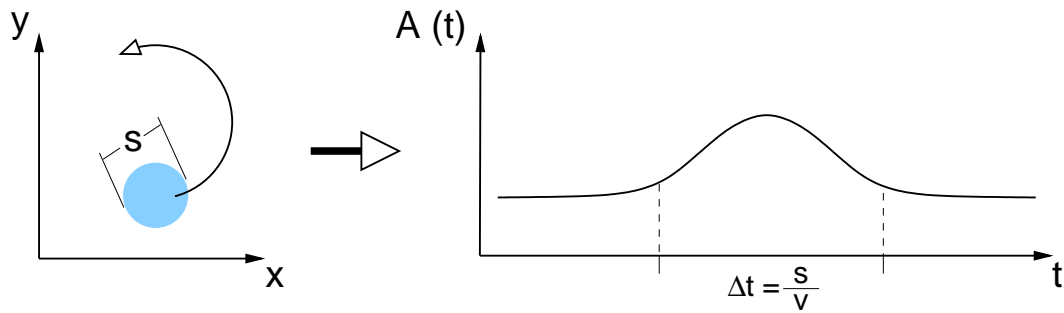


Figure 3.8: A structure of size  $s$  moving with a velocity  $v$  (left plot) causes a signal at a single position along its trajectory a signal with a typical time scale  $\Delta t$  (right plot). Note that  $\Delta t$  depends only on the ratio of structure size and velocity.

detected by this method, i.e. only those structures are detectable which are poking out of the background noise. To overcome these limitations a correlation analysis of selected events is proposed as additional implement to the trigger condition. The results of correlation analysis will be applied on typical plasma turbulence data sets from experiments in the following chapter.

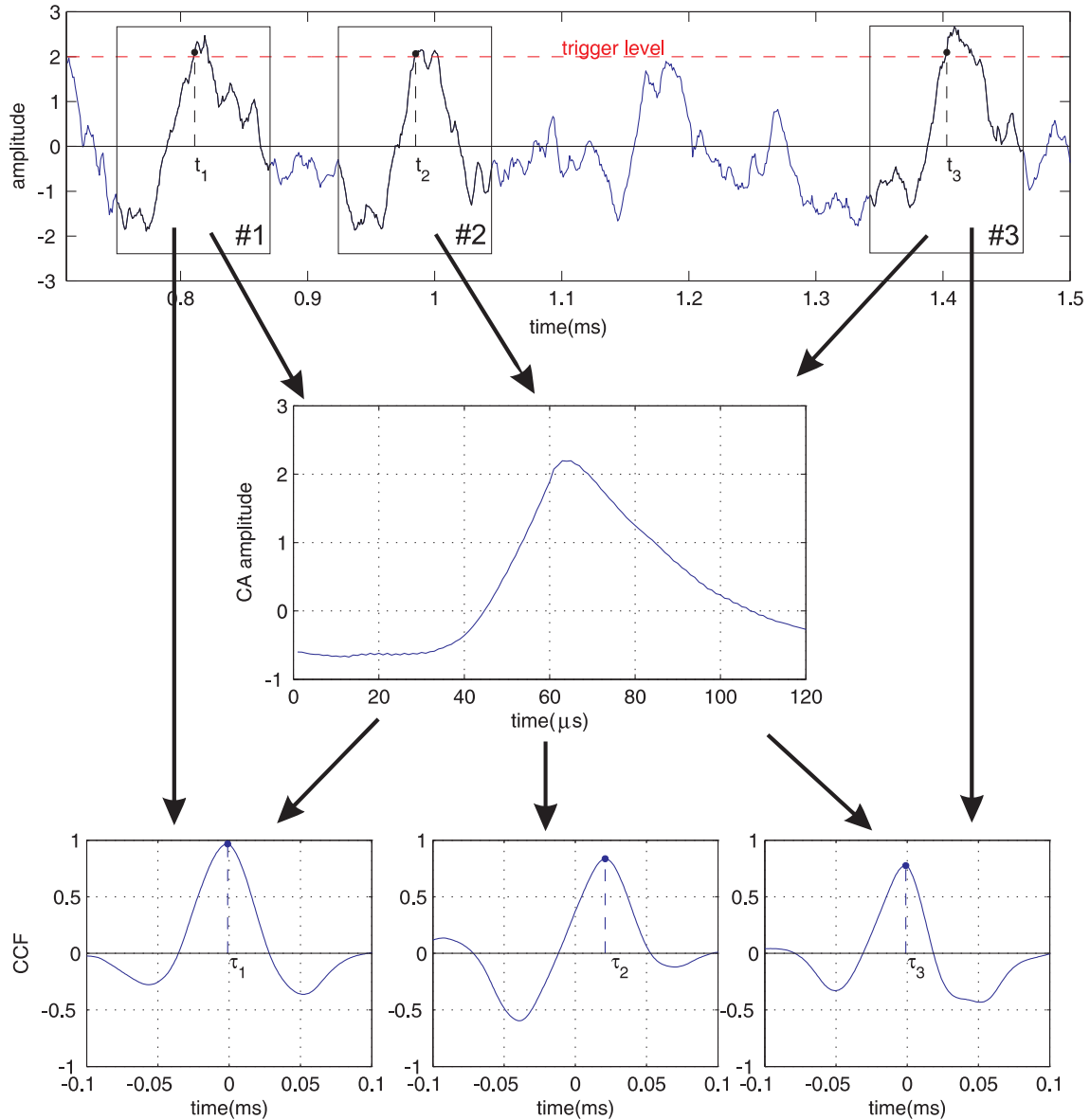


Figure 3.9: The sketch of the proposed correlation analysis to identify trigger errors and trigger jitter. The top picture shows the original time series used for CA analysis. Selected sub-series are labeled by #1...3. The CA result is depicted by the picture in the center. The CCF functions of #1...3 with CA result are shown in the bottom pictures. A shift for maximum correlation (e.g.  $\tau_2$ ) allows to identify trigger jitter.

# Chapter 4

## Application of the CA technique to experiment

In this chapter experimental results of the conditional averaging (CA) method are presented. CA is applied to different systems to investigate its applicability for turbulence studies. For this purpose, experimental data sets from two different experiments (KIWI and Blaamann) are chosen. The reliability of the method is tested first on stationary monochromatic drift waves in KIWI, which are well understood by plenty of previous investigations. The limits of CA in experiment are tested in the complex situation of typical turbulence data sets from a simple magnetized torus (Blaamann, University Tromsø). Further using the proposed correlation analysis (chapter 3 section 3.4), the possible improvements of CA method are analyzed in detail by computation of cross-correlation at reference and at movable probe, respectively. The weak turbulence regime from KIWI is investigated using the standard CA and the proposed correlation analysis of CA results in the last section of the chapter. The CA results of multi-mode state in KIWI are required in the following chapters.

### 4.1 Experimental details

The CA experiments have been performed in two different experimental situations: in a linear magnetized device (KIWI) and in a simple magnetized torus (Blaamann). The KIWI experiment is able to produce a full spectrum of data sets from simple drift waves (Fig. 4.1a) to weak turbulence (Fig. 4.1b) while in Blaamann only the turbulence regime is accessible for investigation. The turbulent plasma regime of KIWI is characterized, additionally by the power law behavior at high frequencies, by presence of pronounced peaks which are observed at lower frequencies [87, 76, 88]. A study of the transition scenario to turbulence reveals a dominant role of drift modes [75] related to these peaks. These global modes are directly driven by the

density gradient perpendicular to the magnetic field and their dynamic is governed by the axially boundary conditions. Further detailed information on the physics of drift waves and turbulence in KIWI can be found in [54]. It should be pointed out, that due to the dominance of modes, the existence of large-scale coherent structures [27] is obvious and the CA method can be used for their diagnostic. The CA analysis of well known drift waves, i.e. drift wave amplitudes and dynamics, is necessary as a preliminary test of the technique.

In case of the simple magnetized torus (SMT) Blaamann, the purely toroidal magnetic field configuration provides closed field lines and the strong uncompressed  $\nabla B$ - and the curvature drift prevent formation of a MHD equilibrium [89, 90]. The plasma source (in this work a RF-source) plays an important role in the formation of potential and density profiles [91]. Details about Blaamann experiment can be found in [50]. The density and potential fluctuations in a SMT yield similar spectra as the SOL fluctuations in fusion devices [52]. The presence of the coherent structures in SMT has been reported in a significant number of papers [92, 20, 93, 94], i.e. for RF-discharge, monopole-like structures were observed [92]. With respect to the instability mechanism, there is experimental evidence that the structures are curvature driven modes [92, 20, 95, 93]. The complex process of turbulence in SMT is a strong test of CA method.

The CA analysis uses the common setup of the technique (chapter 3). The main diagnostic tool consists of the 2D positioning system which scans automatically a poloidal cross-section in the device. Spatio-temporal dynamics of plasma density fluctuations are resolved using CA analysis of the time series from two Langmuir probes mounted at a reference position (RP) and on the positioning system (MP). The reference probe (RP) is localized in the region of the steepest density gradient. To measure the plasma density fluctuation, time series of ion saturation current fluctuations are recorded with a sample rate of 1 MHz. The length of the time series differs in these two experiments from 100.000, in KIWI, to 256.000 data points in Blaamann experiment measurements.

## 4.2 Application of CA to drift wave investigation

A preliminary test of the CA method is done by analyzing the data from monochromatic drift waves in the KIWI experiment. By adjusting the grid bias a monochromatic saturated drift mode can be excited. In the drift wave mode state the time series shows strictly periodic fluctuations of the density (Fig. 4.1a). The power spectrum is sharply peaked at 16 kHz and higher harmonics. The probability density function (PDF) is double humped and peaked at the maximum values of the density fluctuations which is typical for coherent, sinusoidal signals. As a detailed analysis of temporal dynamics in KIWI is given in Chapter 2, only the spatial dynamics features of a stationary saturated drift mode are investigated here using CA analysis.

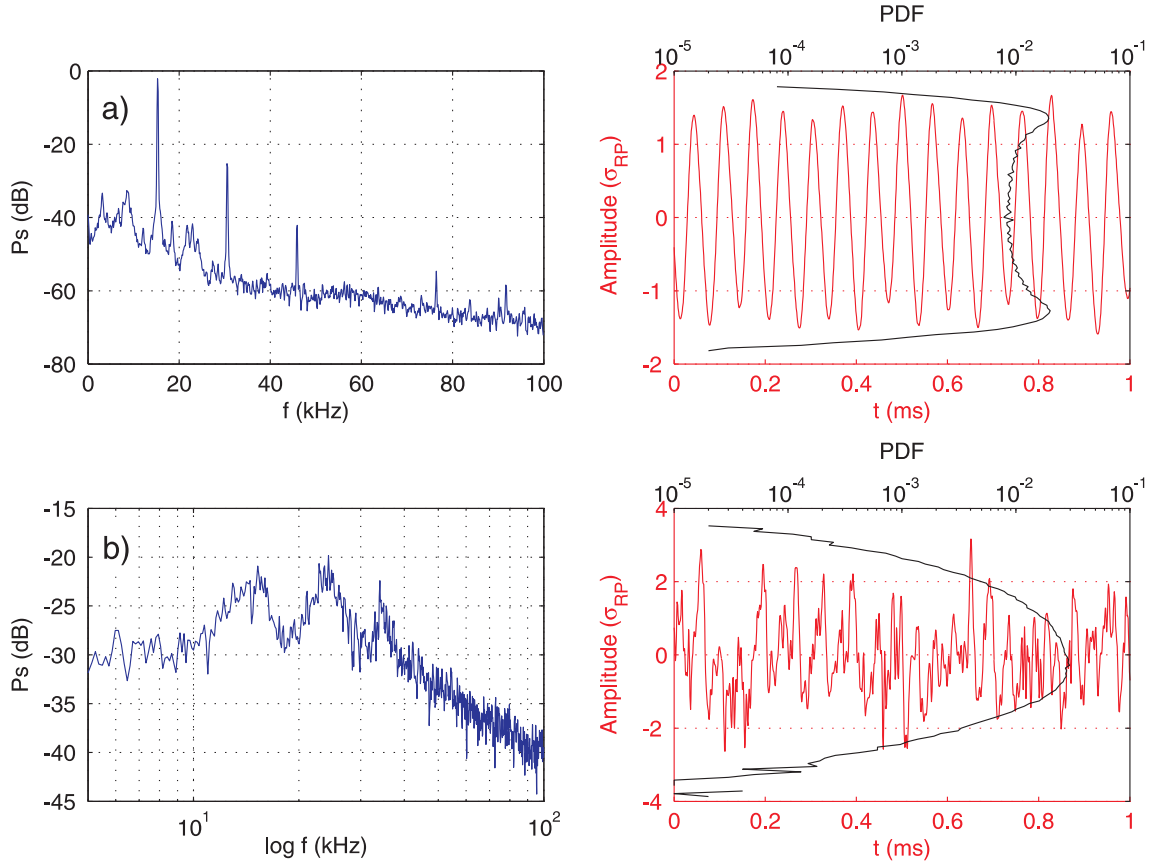


Figure 4.1: Typical spectra (blue line) and time series (red line) of density fluctuations for a drift mode (a) and weak turbulence (b). The black line shows the PDF of fluctuation data.

For this reason, a 2D azimuthal cross-section of the cylindrical plasma in the middle of the magnetized midsection (Fig.2.5) is scanned using a Langmuir probe with a spatial step width of 5 mm.

The conditional averaged result of the density fluctuations in the azimuthal plane is represented in Fig. 4.2. The standard trigger condition is an amplitude threshold ( $f_{cl} = 1 \cdot \sigma_{RP}$ ) combined with a positive signal slope. Two density maxima and two density minima which propagate azimuthally in anti-clock wise direction are found on one azimuthal circumference, i.e. pattern of  $m=2$ . The maximum of the fluctuation amplitude is found in the maximum density gradient region and the amplitude decreases towards the plasma center and edge, as predicted by theory [77]. A periodic wave structure is obtained, i.e. it is not localized in space and time. These results are fully consistent with previous investigations [27]. The resolved drift wave structure amplitudes and dynamics by standard CA analysis reproduce well the previous results of probe array measurements, [54, 8]. Therefore, standard CA gives a reliable tool for monochromatic drift waves investigation. A decisive test

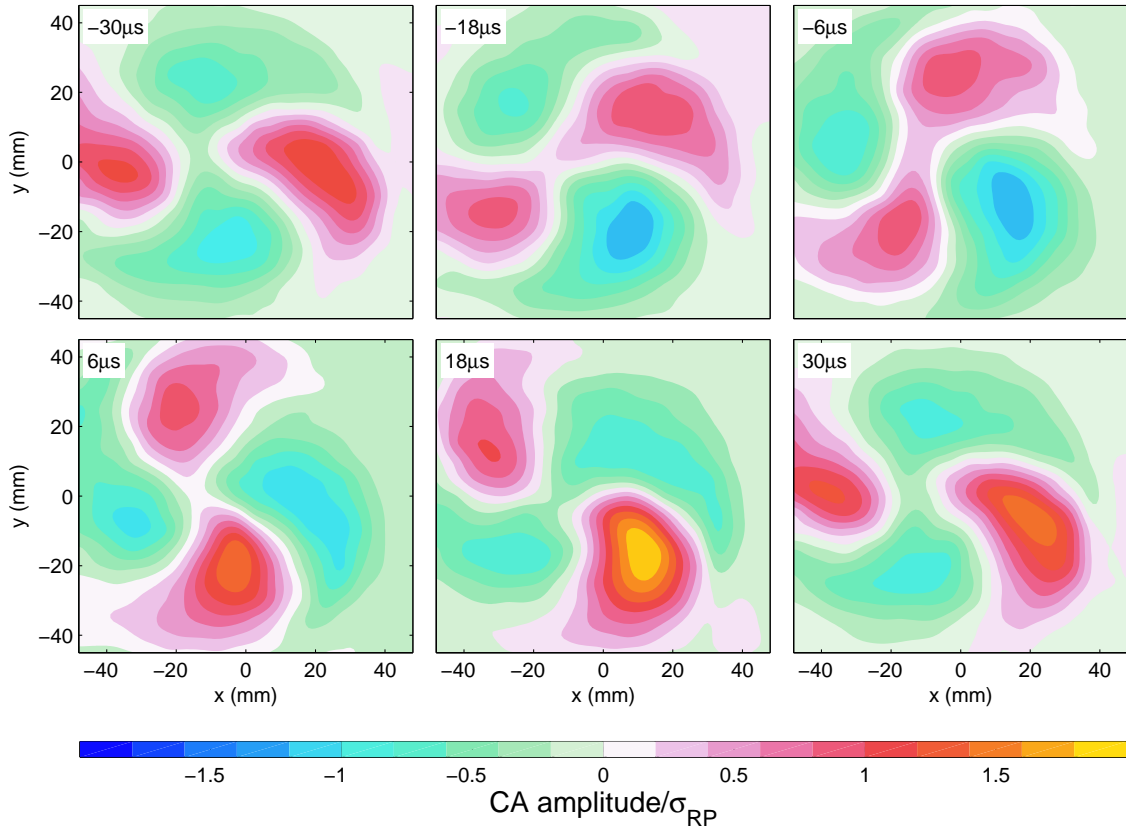


Figure 4.2: Spatio-temporal results of the improved CA analysis for  $-30 \mu s < \tau < 30 \mu s$ . The results are similar to standard CA technique for the drift mode situation. The parameters for the CA analysis are:  $f_{cl} = 1 \cdot \sigma_{RP}$  and a trigger window width of  $0.2 \cdot \sigma_{RP}$ . The time  $\tau$  is given for each subplot in the top left corner.

of CA technique requires applicability for the complex situation of turbulence. For this reason turbulence data sets from Blaamann and KIWI are further analyzed according to the CA procedure.

### 4.3 Application of CA analysis to Blaamann turbulence data

In this section data from the Blaamann experiment is analyzed using the standard CA scheme as described in the chapter 3. Fig. 4.3(a) shows the PDF of the reference probe signal in units of its standard deviation  $\sigma_{RP}$ . It shows a broad distribution of amplitudes with a standard deviation of about  $\sigma_{RP} = 0.12$ . The trigger condition uses an amplitude threshold in combination with a positive slope and a trigger window. In all cases the width of the trigger window is set to  $0.2 \cdot \sigma_{RP}$  and the



### 4.3. APPLICATION OF CA ANALYSIS TO BLAAMANN TURBULENCE DATA41

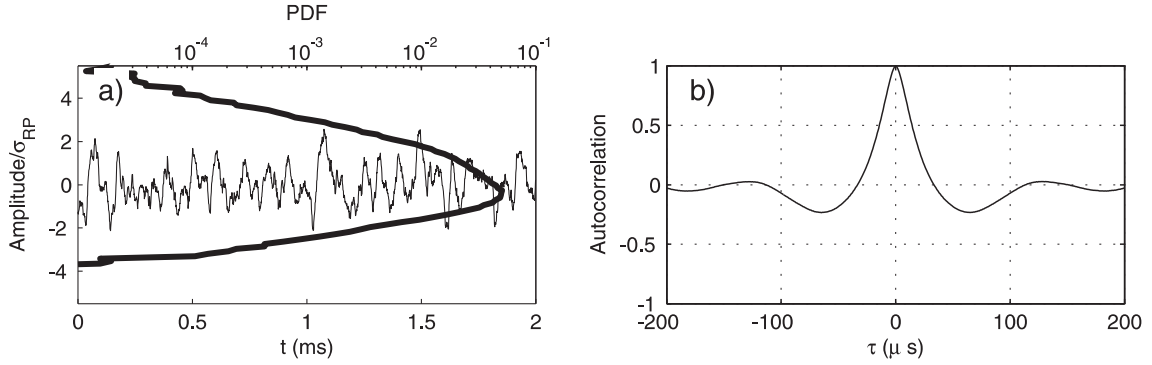


Figure 4.3: (a) A sequence of the typical fluctuation data recorded by the reference probe is represented by the thin line. The bold line shows the PDF of the entire time series. Both are denoted in standard deviation units  $\sigma_{RP}$ . (b) Autocorrelation function of the signal from the reference probe. The autocorrelation function drops to zero at approximately  $\tau = 30 \mu s$ .

trigger level  $f_{c1}$  is specified by the lower boundary of the trigger window. The length of the selected sub-series is chosen with respect to the autocorrelation time (Fig.4.3b) to  $\Delta = 30 \mu s$ , but the results remain qualitatively the same for larger values of  $\Delta$ , [50].

A typical result of the CA process is plotted in Fig. 4.4 where large scale structures are observed which propagate clockwise. The spatial periodicity indicates a mode-like behavior with a mode number  $m = 2$ . Concerning the amplitudes, it should be noted that structures passing directly through the position of the reference probe are artificially improved by the CA analysis. Therefore, amplitude information in close vicinity of the RP has to be interpreted with care.

If the trajectory is extracted from the density maxima in Fig. 4.4 and its amplitude is plotted as a function of its trajectory the results presented in Fig. 4.5a are obtained. Furthermore, the CA amplitude is computed for different trigger levels, i.e.  $f_{c1} = 1.5 \cdot \sigma_{RP}$ ,  $f_{c1} = 2 \cdot \sigma_{RP}$  and  $f_{c1} = 2.5 \cdot \sigma_{RP}$ . Despite of a change of amplitude along the trajectory, indicating growth and decay of the structure, it is seen that the structure amplitude increases with increasing trigger level. Further, the amplitude evolution along its trajectory remains almost unchanged. At first sight, this result is expected as a higher trigger level should remove coherent structures with amplitudes below  $f_{c1}$  and the remaining structures will have a higher amplitude on average. However, to get a quantitative comparison, Fig. 4.5b shows the standard deviation  $\sigma_{MP}$  of  $f_{MP}$  along the same path. It is found that the average fluctuation amplitude is at maximum about  $\sigma_{MP}/\sigma_{RP} = 1.5$  and  $\sigma_{MP} \sim \sigma_{RP}$  at the reference position. With a trigger level  $f_{c1} > 1.5 \cdot \sigma_{RP}$  one should expect the CA-amplitudes (Fig. 4.5a) to be larger or at least equal to  $f_{c1}$ . However, the observed CA-amplitudes are about 2-3 times smaller, which denotes a significant amplitude reduction introduced by the CA process. Even for the extreme case of  $f_{c1} = 2.5 \cdot \sigma_{RP}$

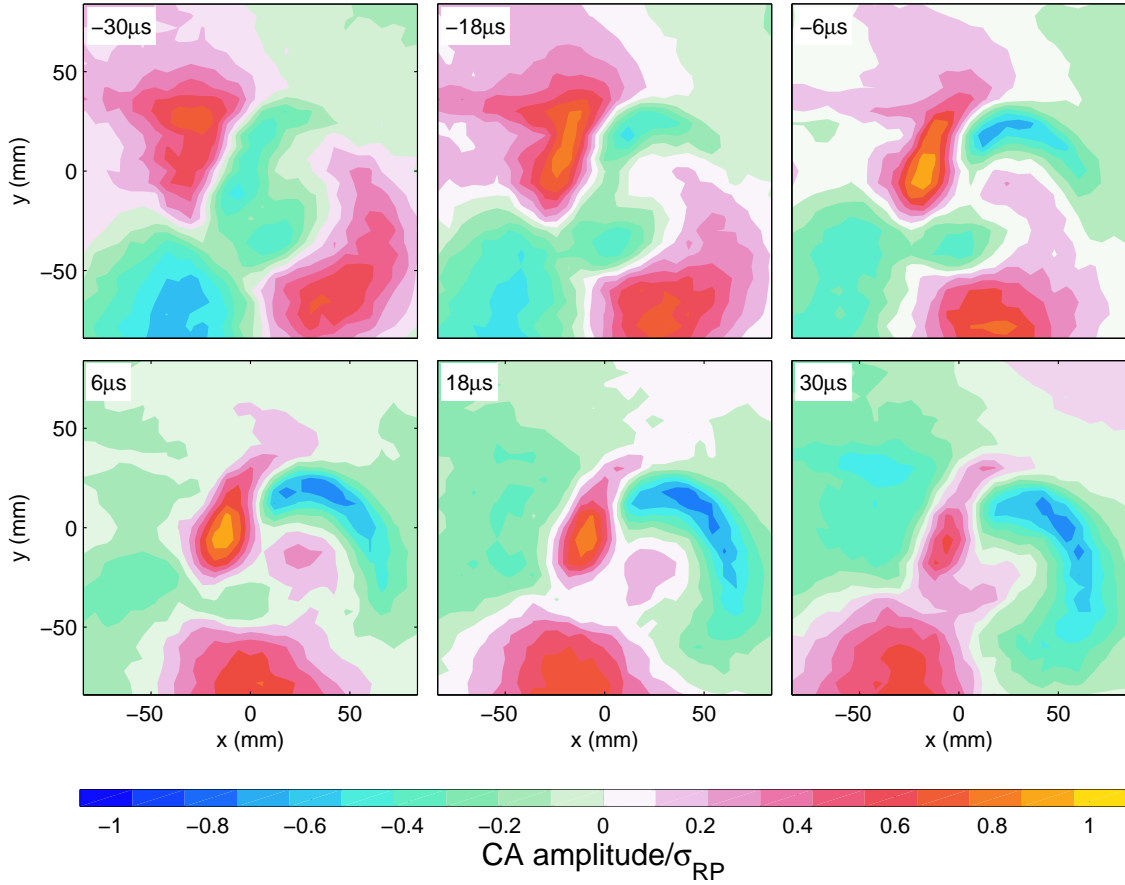


Figure 4.4: Spatio-temporal results of the standard CA analysis for  $-30\mu s < \tau < 30\mu s$ . The parameter for the CA analysis are:  $f_{c1} = 1.5 \cdot \sigma_{RP}$  and a trigger window width of  $0.2 \cdot \sigma_{RP}$ . The time  $\tau$  is given for each subplot in the top left corner. The CA-result shows large scale structures (maxima and minima) propagation clockwise.

the CA-amplitude is smaller than  $\sigma_{MP}$ .

In the previous chapter two possible origins for amplitude damping have been introduced, i.e. trigger jitter and trigger errors. In order to identify the origin of the amplitude damping, the proposed correlation analysis of the CA results is further applied separately on reference and on movable signal.

### CA analysis of reference probe signal

Guided by the simplified CA model presented in the chapter 3, [85], the reference signal  $f_{RP}$  is first analyzed. As any false trigger is caused by an event that differs from those of coherent structures, a correlation analysis should be a suitable approach to identify false trigger events. To analyze the CA process, four quantities are of interest as functions of the trigger level: the CA-result, the trigger statistic,

### 4.3. APPLICATION OF CA ANALYSIS TO BLAAMANN TURBULENCE DATA43

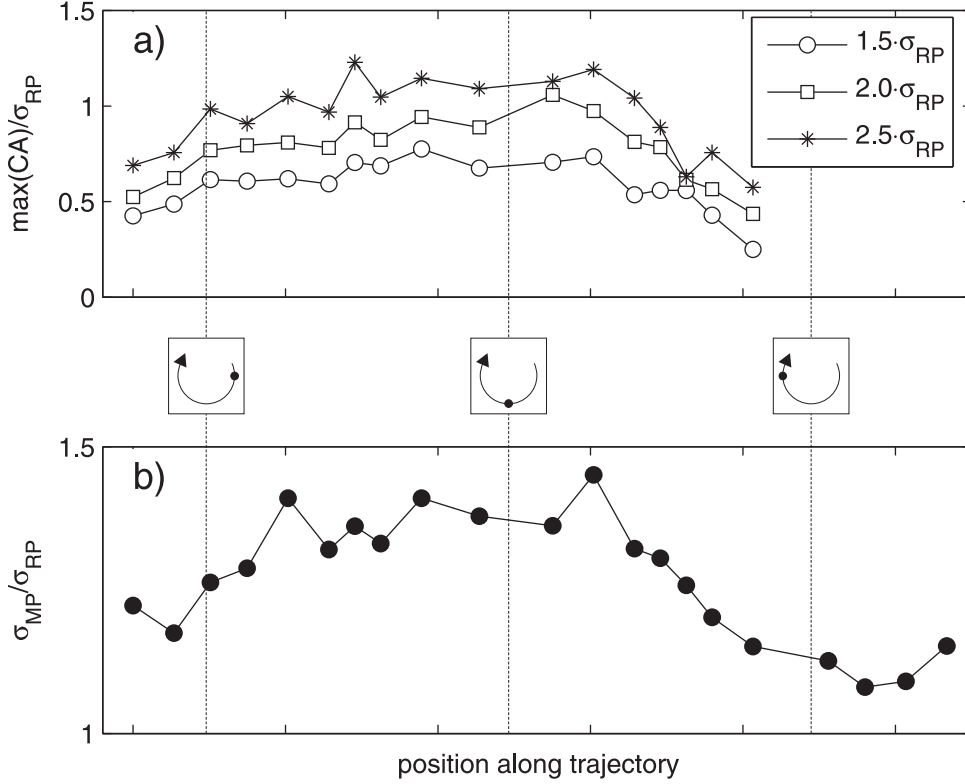


Figure 4.5: (a) The maximum amplitude of the conditional average along the trajectory of a structure. The different symbols denote different trigger conditions (circles for  $f_c = 1.5 \cdot \sigma_{RP}$ , squares for  $f_c = 2 \cdot \sigma_{RP}$ , and stars for  $f_c = 2.5 \cdot \sigma_{RP}$ ). The trajectory of the structure is sketched below the plot. (b) average fluctuation amplitude ( $\sigma_{MP}$ ) of the moveable probe signal along the same path as in (a). Both plots are normalized to  $\sigma_{RP}$ .

the maximum correlation values, and the time lag distribution. All of them are compiled in Fig. 4.6. To simplify cross-reference between different figures all amplitudes are normalized to  $\sigma_{RP}$  throughout this paper. Fig. 4.6a shows the CA-result for different trigger levels. Clearly, the CA-amplitude increases with trigger level  $f_{c1}$  and its peak value corresponds roughly with  $f_{c1}$ , e.g. for  $f_{c1}/\sigma_{RP} = 1$  the CA-amplitude is larger than 1 as well. At the same time, Fig. 4.6b shows that the number of trigger events decreases, as one would expect from the PDF shown in Fig. 4.3a. However, even for the high trigger level  $f_{c1}/\sigma_{RP} > 2$  still a few hundred events are detected. This assures that the time series with 256000 samples is sufficiently long for reasonable statistics, i.e. for a notable noise reduction due to the averaging process. In Figs. 4.6c and 4.6d the results of the correlation analysis are shown. The distribution of maximum correlation as a function of trigger level is shown in Fig. 4.6c. The color map codes the number of events found for that specific correlation value, i.e. a vertical summation of Fig. 4.6c would give Fig. 4.6b. It is seen that most of the events are found to have rather high correlation values with  $\max(\text{CCF}) > 0.8$ .

For a low trigger level ( $f_{c1}/\sigma_{RP} < 1$ ) a considerable amount of low correlated events are found which are absent for a high trigger level ( $f_{c1}/\sigma_{RP} > 1.5$ ). The time shift  $\tau_{max}$  of the maximum correlation is plotted in Fig. 4.6d. Time shifts  $\tau_{max} > 0 \mu s$  mean that the trigger event occurred too early, i.e. the highest correlation is found at a later time. The time shift distribution has a slight asymmetry with respect to  $\tau_{max} = 0 \mu s$ . Nearly no events are found with  $\tau_{max} < -10 \mu s$ . Further, many of the events have a time shift with  $\tau_{max} = (0 \pm 2) \mu s$ , which is of the order of the time resolution of the recording system.

In the previous chapter [85], it was shown that both effects, trigger errors and trigger jitter, contribute to an amplitude damping. Hence, according to Figs. 4.6c and 4.6d the fraction of low-correlation events for  $f_{c1}/\sigma_{RP} < 1$  and those with significant trigger jitter ( $\tau_{max} \neq (0 \pm 2)\mu s$ ) should cause an amplitude damping. To investigate this in detail, we exclude those events with trigger jitter from the CA process. The CA is computed separately for the events included in the selected jitter domain and for the remaining part. The results are shown in Fig. 4.7. Figs. 4.7a and 4.7c contain the results for those events which have a trigger jitter of  $\tau_{max} = (0 \pm 2)\mu s$ , while Figs. 4.7b and 4.7d are the corresponding plots for all events with  $\tau_{max} \neq (0 \pm 2)\mu s$ . Depicted are the results of CA (Figs. 4.7a and 4.7b), the maximum correlation distribution (Figs. 4.7c and 4.7d), the trigger statistics (Fig. 4.7e) and the CA-amplitude (Fig. 4.7f) as a function of trigger level  $f_{c1}/\sigma_{RP}$ . Compared to Fig. 4.6c, significant changes are observed for the distribution of maximum correlation. Fig. 4.7c shows that those events with small trigger jitter are highly correlated. The notable fraction of low correlation events observed for  $f_{c1}/\sigma_{RP} < 1$  in Fig. 4.6c has disappeared. All low-correlation events are related to trigger-jitter events as shown in Fig. 4.6d. For  $f_{c1}/\sigma_{RP} > 1$  in both cases (Figs. 4.7c and 4.7d) the average correlation is high. A similar behavior is found for the CA-results (Figs. 4.7a and 4.7b). While for low trigger level Fig. 4.7a shows amplitudes which are higher than  $\sigma_{RP}$ , the average amplitude of the trigger-jitter events (Fig. 4.7b) almost vanishes, which is expected for the average of low correlation events. In Fig. 4.7e the number of low-jitter (stars), high-jitter (dots) events and their sum (circles) are plotted for different trigger level. It is found that our rather strict criterion of  $\tau_{max} = (0 \pm 2) \mu s$  identifies almost half of the events as high jitter events, but the remaining fraction is still large enough to ensure good statistics. Although it is tempting to ease the jitter criterion in order to select only the low correlation part as trigger errors, one has to keep in mind that the trigger jitter itself causes an amplitude damping as well, i.e. all events with high correlation in Fig. 4.7d affect the CA-result. This becomes visible if Figs. 4.7a and 4.7b are compared. The CA-result in Fig. 4.7b is broader than in Fig. 4.7a due to trigger jitter. Additionally, a comparison of CA-amplitudes (Fig. 4.7f) yields that removing high jitter events from the CA increases the CA-amplitude up to a factor of two for low trigger level ( $f_{c1}/\sigma_{RP} < 1$ ).

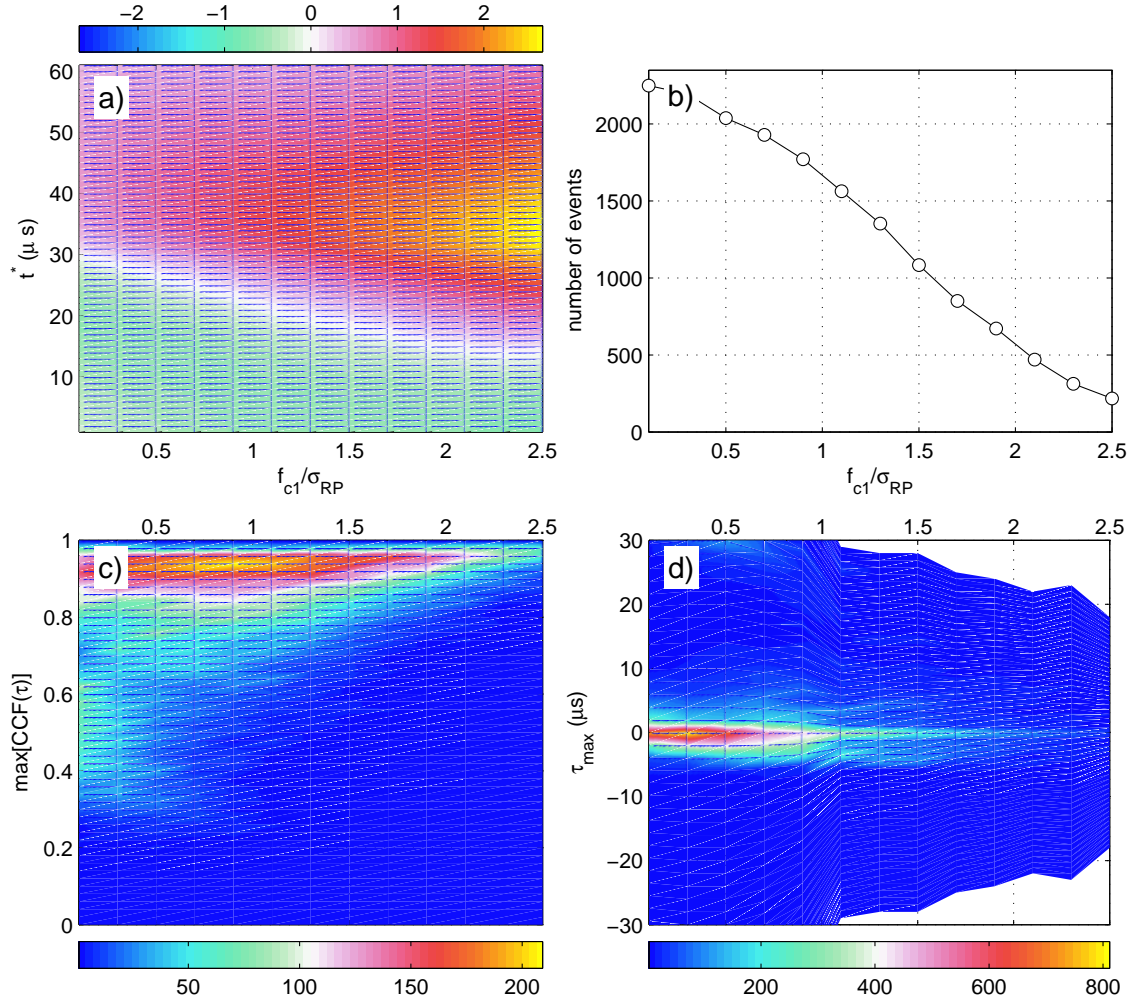


Figure 4.6: (a) CA-result at the reference probe as function of the trigger level  $f_{c1}$ . The CA results are obtained for a trigger window width of  $0.2 \cdot \sigma_{RP}$ . The CA-amplitudes are visualized by the color map and normalized to  $\sigma_{RP}$ . (b) number of trigger events as a function of trigger level. (c) distribution of maximum cross-correlation of all sub-series and the CA-result as a function of trigger level. The color denote the number of sub-series found for a specific value of maximum correlation. (d) distribution of trigger jitter  $\tau_{max}$  of maximum correlation with respect to  $\tau = 0$  as a function of trigger level.

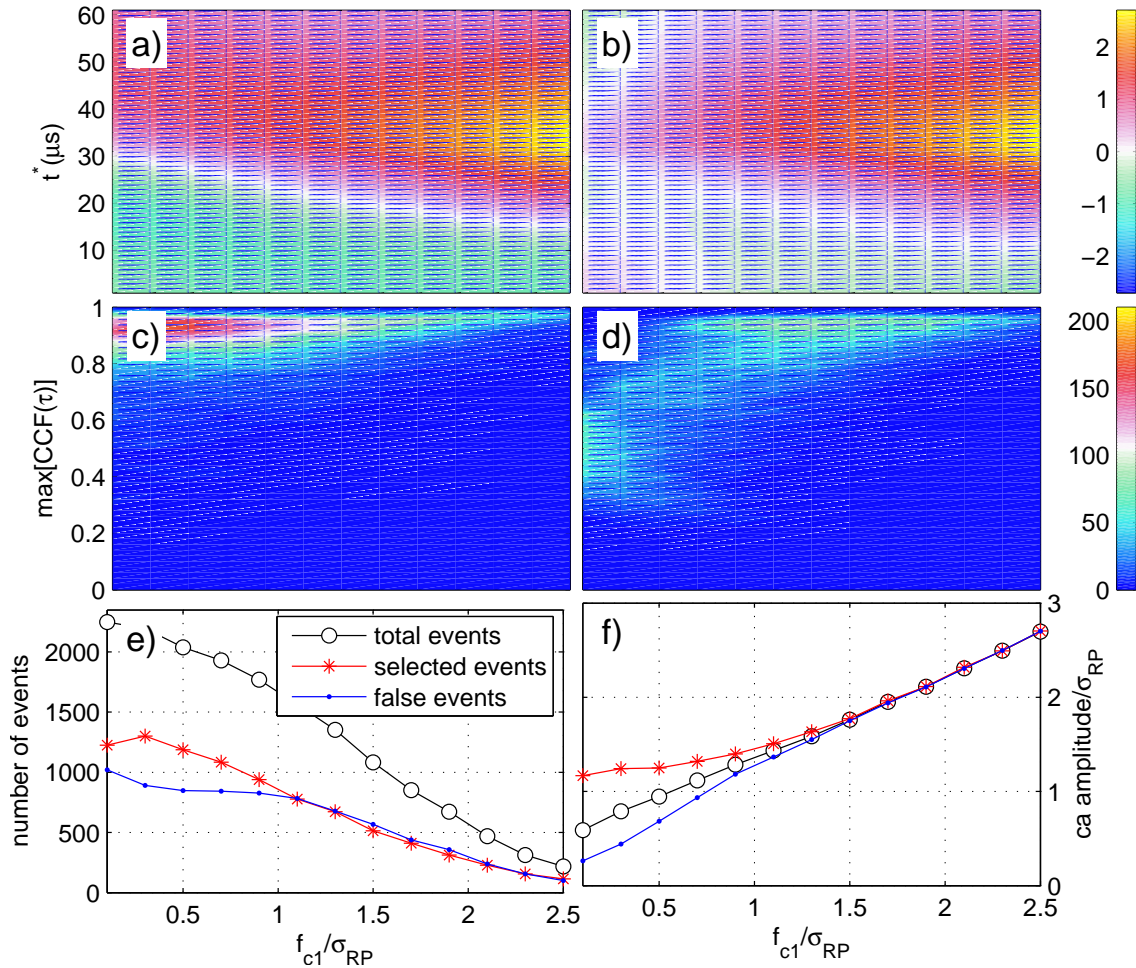


Figure 4.7: Analysis of the reference probe signal. The CA and correlation analysis for events with low jitter are plotted in (a) and (c). The results of CA and correlation analysis for the trigger errors are shown in (b) and (d). The plots are similar to Fig. 4.6a and Fig. 4.6c and use the same scaling to  $\sigma_{RP}$ . (e) event statistics as a function of trigger level. The number of events are shown for low-jitter events (stars), for high-jitter events (dots), and for all events (circles). (f) shows the maximum amplitude of the CA-result as a function of trigger level. The different markers are used as in subplot (e).

This analysis shows that the proposed correlation analysis can identify false-trigger events. Surprisingly, this simple trigger jitter criterion removes also the fraction of low-correlation events from the CA process. The analysis further shows that these false-trigger events cause a significant amplitude damping for low trigger level. However, for a trigger level of  $f_{c1}/\sigma_{RP} > 1.5$  the analysis shows as well that the amplitude damping observed in experiment (see Fig. 4.5) cannot be explained.

### CA analysis of moveable probe signal

When the correlation approach is applied to the reference probe, trigger jitter and trigger errors can be identified and, as the previous paragraph has shown, successfully eliminated. However, the typical CA process involves two probes which are separated spatially. This implies that not every event at the reference probe necessarily has to be linked to a coherent structure at the moveable probe. This new type of trigger errors might arise from a limited life time of structures, from structures following different trajectories or from noise. Of course, these trigger errors would give rise to the same amplitude damping as those discussed in the previous section. To investigate whether this causes the observed amplitude reduction in experiment, the correlation approach is now applied to the moveable probe signal. To discuss the results, the same analysis as in the previous paragraph is now performed at the position  $[x, y]_{MP} = [0 \text{ mm}, -79 \text{ mm}]$ , i.e. close to the lower boundary of the scanned area. The trigger events are still determined from the reference probe signal using a trigger window with a width of  $0.2 \cdot \sigma_{RP}$ . According to Fig. 4.7f a preselection of trigger events is not necessary at the reference probe for high trigger level. Fig. 4.8a shows the CA-result for different trigger level. At first glance, the CA-results show a similar behavior as observed for reference signal, i.e. an increasing trigger level yields an increase of CA-amplitude and the event number drops at the same time (Fig. 4.8b). However, compared to Fig. 4.6a and Fig. 4.7a, a very broad maximum with low amplitude is observed. The amplitude of the CA-structure is only about half of the trigger level although the fluctuation level is much higher at that position (see Fig. 4.5b).

Plotting the maximum correlation distribution as a function of trigger level (Fig. 4.8c) reveals significant differences with respect to the CCF analysis of the reference probe. This time the CCF plot shows a broad distribution with two distinct populations of events, a part with high correlation and a part with very low correlation. In contrast to the reference probe, here the two parts are more and more clearly separated with increasing trigger level and the low-correlation part does not disappear for high trigger level and its total number is not negligible. Interestingly, the time lag distribution (Fig. 4.8d) does not differ too much from the reference probe analysis (Fig. 4.6d). Still a significant number of events is detected with low time shift.

The next step of the analysis again selects all trigger events with  $\tau_{max} = (0 \pm 2) \mu\text{s}$ .



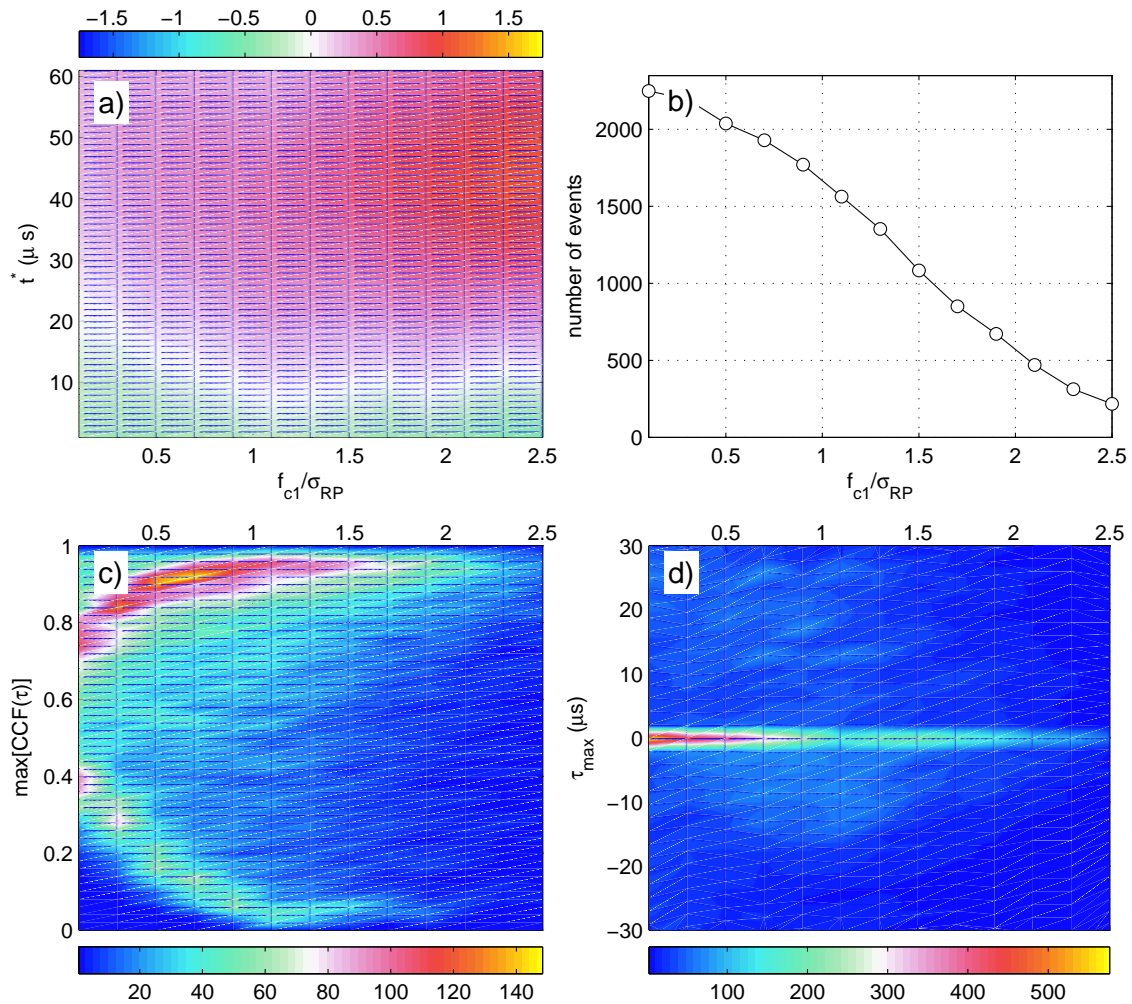


Figure 4.8: Results of the cross-correlation analysis of the moveable probe signal at  $x_{MP} = 0$  mm and  $y_{MP} = -79$  mm. The CA-result (a), the events statistic (b), the distribution of maximum correlation (c) and the trigger jitter distribution are plotted as a function of trigger level. A complete plot legend is found in the caption of Fig. 4.6. Please note the low amplitudes for the CA-result (a) and the two distinct populations with high and low correlation values (c), which differ significantly from the results of the reference probe signal analysis (Fig. 4.6a and 4.6c).



The results are plotted in Fig. 4.9. First, the CA-amplitude for the selected events is dramatically improved (Fig. 4.9a) while the CA-amplitude for the trigger errors is small even for a high trigger level (Fig. 4.9b). Fig. 4.9f shows that the amplitude improvement is typically a factor of 2-3. The origin of this high amplitude is shown by Figs. 4.9(c-e). The distribution of maximum correlation for the selected events has changed completely. For all trigger levels only high-correlation events remain after application of the trigger jitter filter (Fig. 4.9c). All low-correlation events are identified as trigger errors (Fig. 4.9d). The high gain in CA-amplitude is attributed to the event statistics (Fig. 4.9e). Over two thirds of the events (dots) are identified as high-jitter events, i.e. trigger errors. Although, the number of events with low jitter seems quite small, typically 250 events are used for the CA process and therefore the statistics for the averaging process is still acceptable.

The results observed by correlation analysis and jitter selection were computed for one position far away of the reference. In order to see a similar analysis for all spatial position from the scanned area we resume to trigger condition  $f_c = 1.5 \cdot \sigma_{RP}$  where CA results shows the best results in Fig. 4.9. For this reason the mean CCF value and event statistics for all spatial position is computed, Fig. 4.10. By using all triggered events (at RP) Fig. 4.8c the mean CCF is shown in Fig. 4.10a. The same values for events with low trigger jitter ( $-2\mu s \leq \tau \leq 2\mu s$ ) from Fig. 4.9a and with high trigger jitter, Fig. 4.9b are shown in Fig. 4.10b-c. These 2D maps shows higher CCF values for events having low trigger jitter over the entire scanned area, i.e. by jitter selection only the coherent events are selected at all spatial positions. The results on the event statistics, Fig. 4.10d-f are similar to Fig. 4.9e. They shows a lower number of coherent events (but sufficient, 250 - 600) Fig. 4.10e then noise events Fig. 4.10f for entire scanned area. The image pattern is caused by the signal shape and sub-series length ( $\Delta = 30 \mu s$ ), i.e. sub-series which include a coherent event maxima are higher correlated.

As for standard CA, the amplitude of the CA-result can be judged by comparison with  $\sigma_{MP}$  along the path of the structures. Fig. 4.11 basically shows the same as Fig. 4.5, but now  $\sigma_{MP}$  is compared to the amplitudes of the improved CA process. The result is encouraging. The CA-amplitudes are now about the same or little higher than  $\sigma_{MP}$  and they are close to the trigger criterion of  $f_{c1}/\sigma_{RP} = 1.5$ . This means that the CA-result for the coherent fraction of the fluctuations is fully consistent with overall fluctuation amplitudes and hence increases the validity of the CA-result.

To demonstrate the full performance of the improved CA method, the results of the different methods are compared in Fig. 4.12, which visualizes the results from the standard and the improved CA technique. In all cases the trigger level is set to  $f_{c1}/\sigma_{RP} = 1.5$  and the trigger window width is set to  $0.2 \cdot \sigma_{RP}$ . The first row of pictures shows the spatio-temporal evolution of the standard CA-result (Figs. 4.12a). It shows large scale structures which propagate clockwise. Their amplitude is quite low and significantly below  $\sigma_{RP}$ . The second row of images depicts the improved

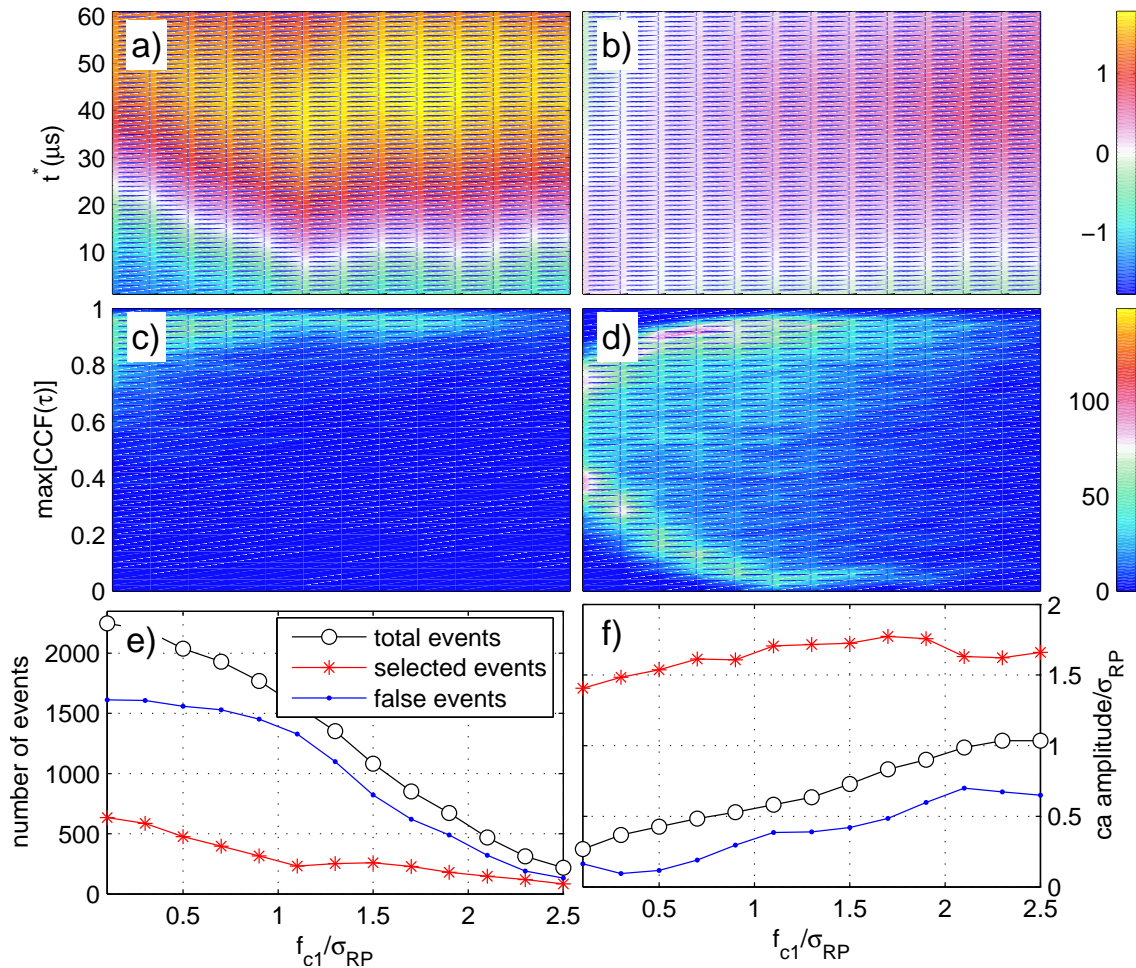


Figure 4.9: Application of trigger-jitter filter to the moveable probe signal. The CA and correlation analysis for events with low trigger jitter are plotted in (a) and (c). The CA and correlation analysis for the trigger errors are shown in (b) and (d). The event statistics is plotted in (e) and the maximum amplitude of the CA-result is shown in (f). For details see Fig. 4.7. Note the large difference in CA-amplitude in plot (a) and (b). Further, the low-correlation events (see Fig. 4.8c) disappeared in (c).

### 4.3. APPLICATION OF CA ANALYSIS TO BLAAMANN TURBULENCE DATA51

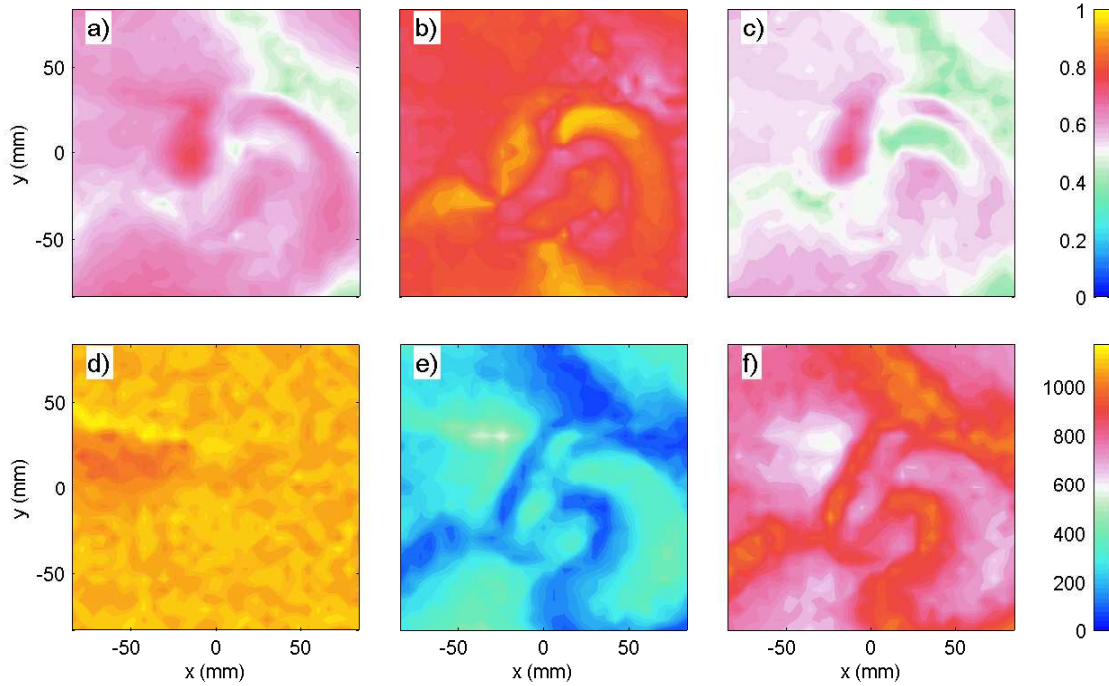


Figure 4.10: 2D results of the correlation analysis on MP. (a-c) the average of the CCF for trigger level of  $f_c = 1.5 \cdot \sigma_{RP}$  from the Fig. 4.8c and Fig. 4.9c-d at all spatial positions. (d-f) the trigger statistics from Fig. 4.9e at  $1.5 \cdot \sigma_{RP}$ . The color map indicates the number of events.

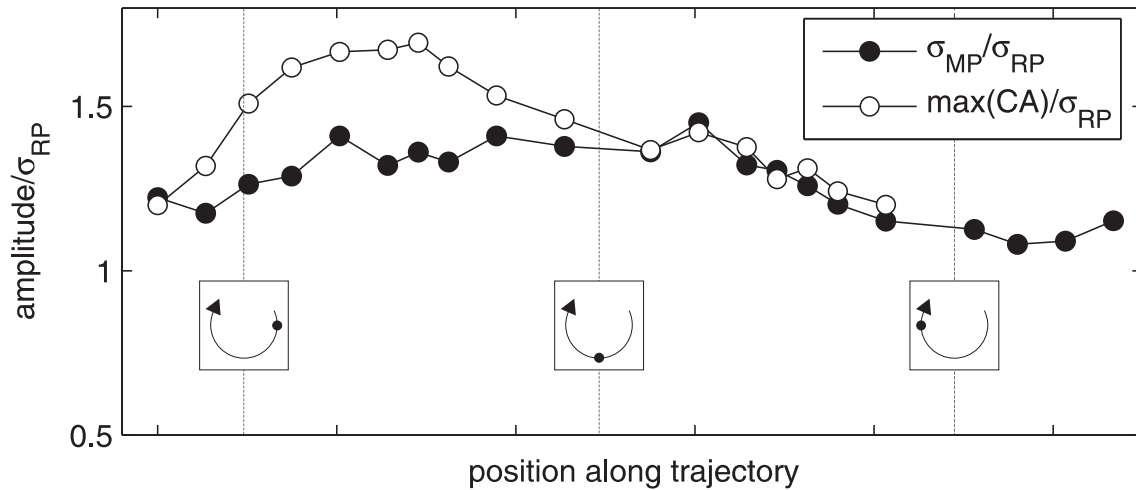


Figure 4.11: Result of the CA analysis including only low-jitter events in the averaging process (see Fig. 4.5 for comparison). Maximum amplitude of the conditional averaged signal along its trajectory for a trigger condition  $f_c = 1.5 \cdot \sigma_{RP}$  is denoted by the open circles. The solid circles are used for the average fluctuation amplitude  $\sigma_{MP}$ .

CA-results (Figs. 4.12b). Compared to Figs. 4.12a, the topology is the same, but the amplitudes are about three times higher. The artificially enhancement close to the reference probe Figs. 4.12a (see also Figs. 4.4) is not anymore present in the improved data. In the third row the spatio-temporal CA-result of the trigger errors is plotted. It shows only a weak similarity with the topology of Figs. 4.12a and 4.12b and the amplitudes are very low, which is expected as the average of weakly correlated events (noise) should vanish. Together the plots in Fig. 4.12 demonstrate, that the correlation analysis allows to improve the CA-result at any position of the scanned area. A closer inspection of the results at all positions even reveals that the average correlation value for the entire area is  $0.9 \pm 0.1$  and the event statistics shows about 250 events at each spatial position, i.e. the example of the moveable probe signal analysis shown in Figs. 4.8 and 4.9 is a typical result as it agrees qualitatively and quantitatively with other positions.

## 4.4 Application of CA analysis to KIWI turbulence data

The second test of the CA for complex data set is made by means of turbulence data from the KIWI device. In particular, the turbulence situation is analyzed using standard and improved (based on correlation analysis) CA technique. The temporal dynamics of weak turbulence state from KIWI experiment is denoted in Fig. 4.1b. The time series of the density fluctuations shows a spiky irregular behavior. In the corresponding power spectrum, frequency peaks are strongly broadened. The decrease of the power spectrum at high-frequency regime is given by law  $S(f) \propto f^{-\alpha}$  with  $\alpha \approx 3$ , which is typical for 2D-turbulence [96]. The broad peaks in the lower-frequency regime of the spectrum indicate that the turbulence is only weakly developed [75, 76]. The PDF of the density fluctuations is single humped and close to gaussian. The temporal dynamics detail of drift waves and turbulence were already studied in many papers and the main objective of the present chapter is to study prospects and limitation of CA in experiment. For CA analysis the plasma density is taken at the reference with a trigger limit of  $1.5 \cdot \sigma_{RP}$ . The statistical results of the correlation analysis are shown in Fig. 4.13. The number of events selected (Fig. 4.13a) by the improved method (red line) is low,  $\sim 200$  but still sufficient for good statistics. Similar amplitude results, Fig. 4.13b, have been found for a storage of 1MB (time series of 1s length) when the event statistic is better. An amplitude improvement is clearly obtained employing the improved technique with constant maximum values for  $f_{c1} \geq 1.5 \cdot \sigma_{RP}$ .

The spatio-temporal evolution of the CA structure is shown in Fig. 4.14. The results are computed using standard, Fig. 4.14a, and improved technique, Fig. 4.14b. The remaining part is plotted in Fig. 4.14c. The development of a large-scale turbulent density structure is clearly seen. At time  $\tau = 0 \mu s$  the positive density structure

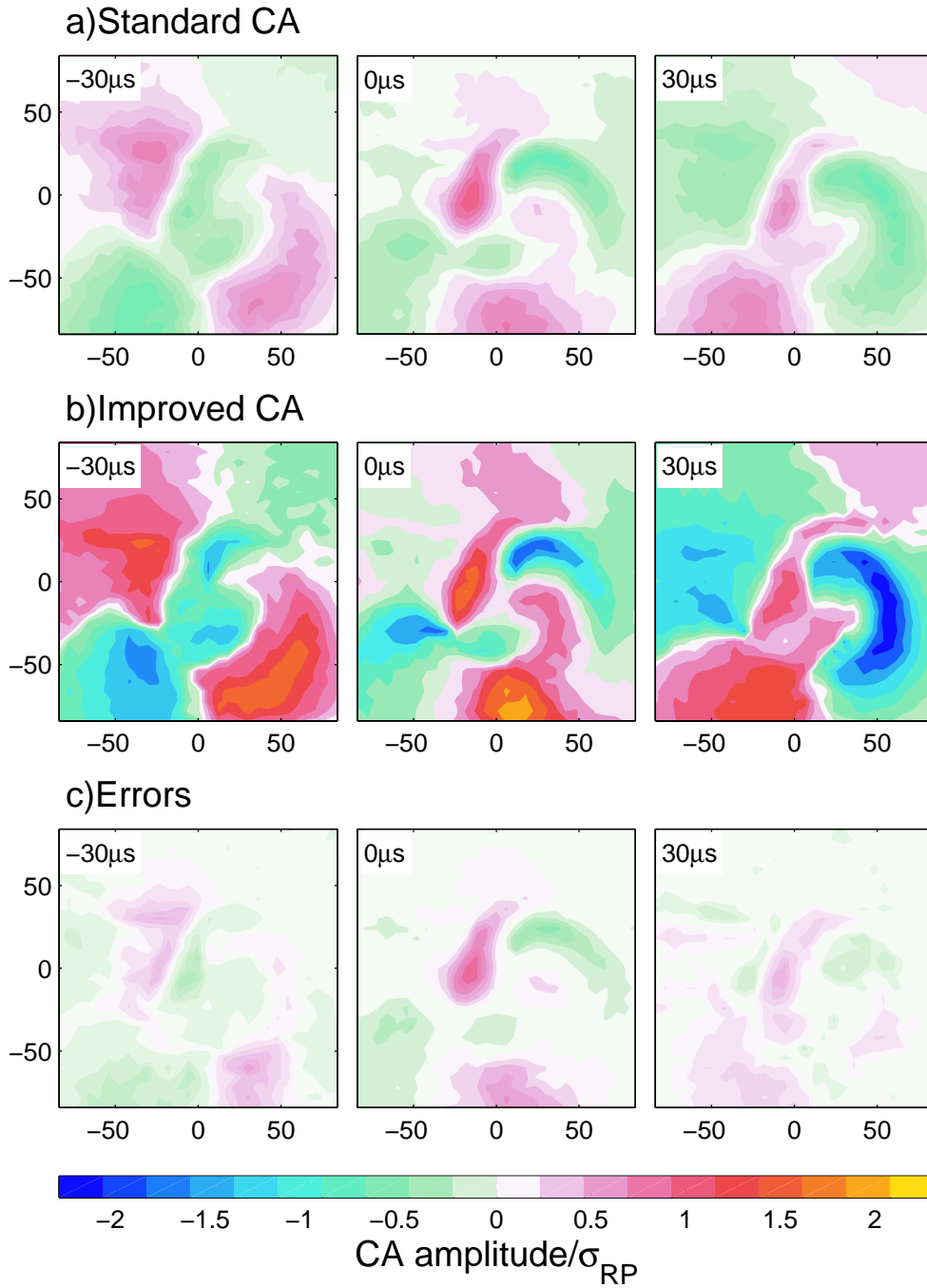


Figure 4.12: Spatio-temporal results of the CA analysis for  $\tau = -30\mu s$ ,  $\tau = 0\mu s$ , and  $\tau = 30\mu s$ . (a) is the result of standard CA, i.e. using all trigger events. (b) is the result if only events with low jitter are used. For the case of events with high jitter the result is shown in (c). All amplitudes are normalized to  $\sigma_{RP}$ , i.e. the color code is the same for all pictures. Note the amplitude enhancement for the improved CA method as well as the sharp contours of the structure.

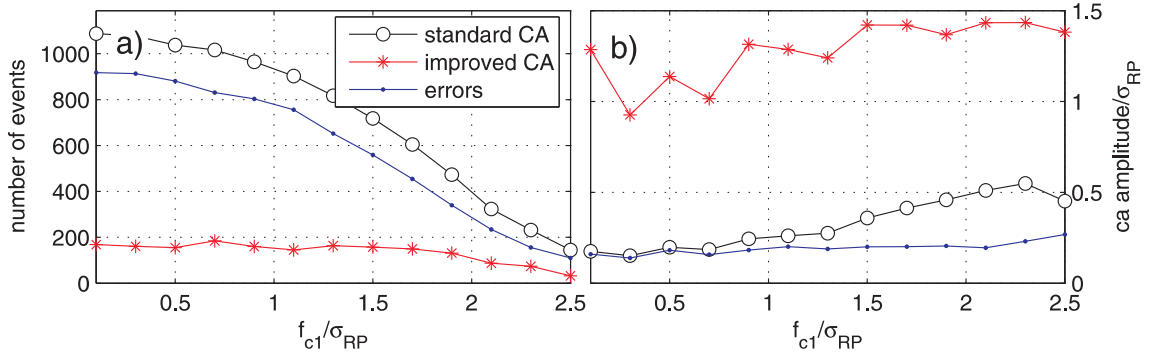


Figure 4.13: Event statistics in CA process for different trigger levels of a weak turbulence data (a). The number of events are shown for low jitter events (red stars), for high jitter events (blue dots) and for all selected events (black circles). The amplitude enhancement by improved CA method is shown by (b). For  $f_{c1} > 1.5 \cdot \sigma_{RP}$  it shows maximum constant values.

is found at the position of the reference probe. The shape of the observed structure is a monopole-type. The radial extend of the observed structure is similar to the extend of the drift mode (Fig. 4.2) and the structure size roughly corresponds to the plasma radius. The results are in good agreement with previous investigations [27]. An amplitude improvement is clearly seen and is about factor of 1.5-2. This improvement yields to a better spatial localization of CA resolved structures, i.e. enhancement of transport measurements.

## 4.5 Conclusion

Based on an analytical model and simulations of conditional averaging discussed in the Chapter 3, the effect of trigger errors on the averaging process on experimental data sets was investigated in detail in this chapter. First the CA results of standard technique on drift waves have shown reliable results in good agreement with previous investigations. Further the standard CA method was tested on turbulence data from the simple magnetized torus Blaamann. It was found that the results of standard CA are not consistent with the average fluctuation level and the chosen trigger level. Obviously, the CA process has been found to introduce a significant amplitude damping. To analyze the origin of the amplitude damping, a correlation analysis of the CA-results was applied. Its application to the reference probe signal revealed that trigger jitter and false trigger events cause a significant amplitude damping for low trigger level. However, the analysis could not explain the observed amplitude reduction for the high trigger level found in experiment. By applying the same correlation analysis to the moveable probe signal it was shown that the amplitude reduction can be avoided. On weak turbulence data from the KIWI experiment, it was also shown that the improved CA technique is required to gain full amplitude

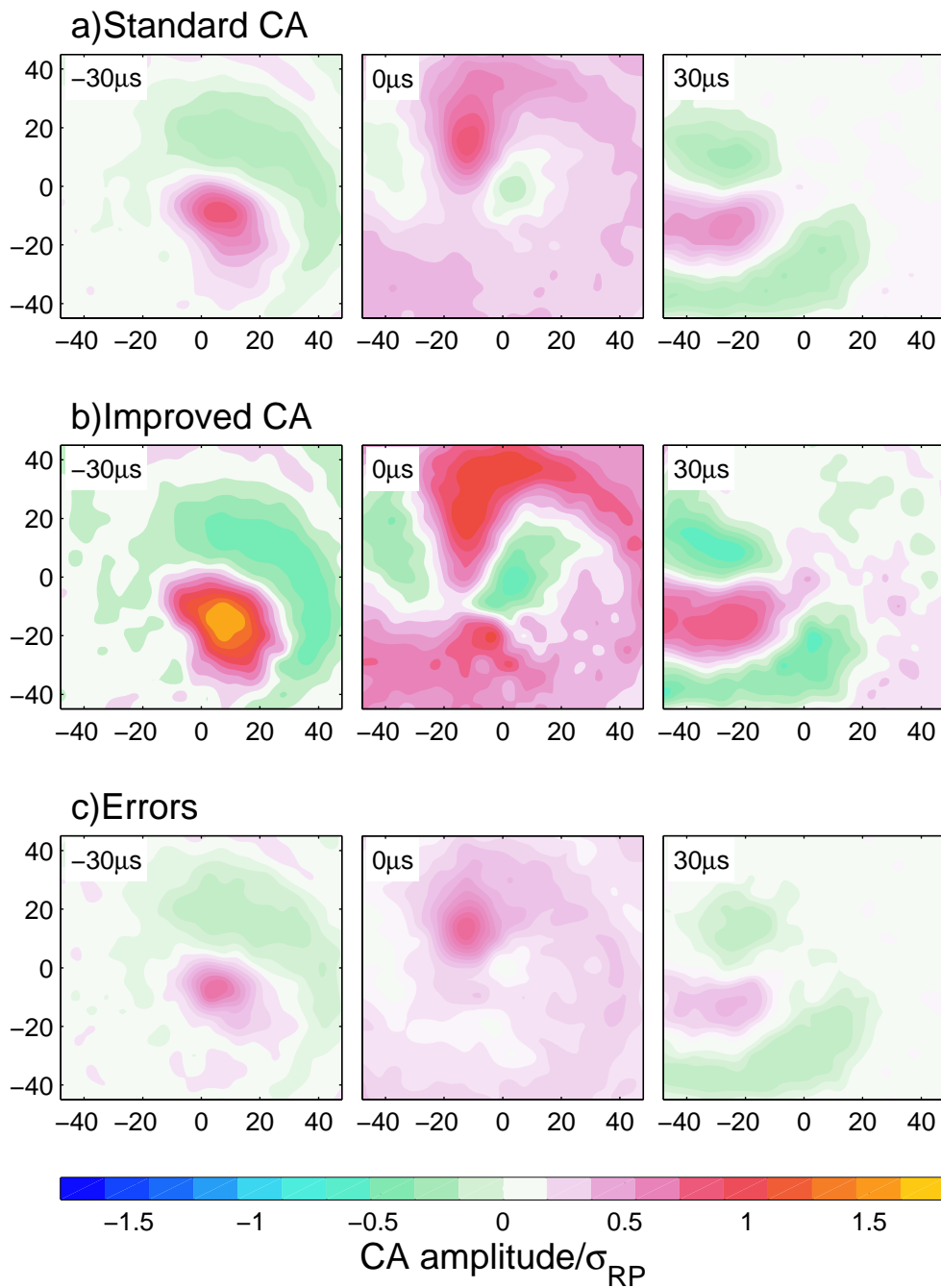


Figure 4.14: Spatio-temporal results of the CA analysis for standard (a), improved (b) method and the remaining part (c). All amplitudes are normalized to  $\sigma_{RP}$ , i.e. the color code is the same for all pictures. The amplitude enhancement for the improved CA method is obvious.

information. Therefore, the amplitude information of coherent fluctuation can be recovered by conditional averaging if trigger errors and trigger jitter are carefully taken into account.



# Chapter 5

## Technical issues of spatio-temporal diagnostics

Besides statistical techniques spatio-temporal diagnostics of plasma fluctuations can be made using multi-probe measurements as well. In the experiment KIWI, a 2D poloidal array as presented in the Chapter 2 is used. This instrument allows to measure plasma fluctuation at 63 positions simultaneously and with a fully coverage of the plasma column. The manufacturing difficulties of the probe array leads to variation of probe size and position. In previous investigations [54, 9, 8, 27], probes were distributed to cover one azimuthal circumference in the device, i.e. only 1D in space. For those probe arrays a normalization of probe signal to standard deviation gave reliable results due to the azimuthal symmetry of the device. For the new probe array a calibration is required due to the radial and azimuthal probe distribution. Furthermore, the effects of low spatial resolution, in order to limit plasma disturbance, have not been investigated in previous works. Therefore, this chapter concentrates on all these technical aspects of the probe array. Calibration methods for probe position and size as well as the spatial resolution aspects are investigated.

### 5.1 The probe position estimation

Manufacturing difficulties of the probe array lead to errors in the positioning and the size of the probes. Technically, errors of about  $\pm 0.5$  mm in probe length can not be avoided. This will lead to different collecting areas, i.e. amplitude information is distorted. Also, an exact positioning of the probe is practically difficult to realize. Therefore, a probe size and position calibration is required.

To estimate the probe position a method consisting of two steps is proposed. First, the position of probes is determined inside the plasma device, using a plasma beam and positions are given with respect to the vacuum vessel. Second, the accuracy of estimated positions can be improved using a picture from a high resolution camera.

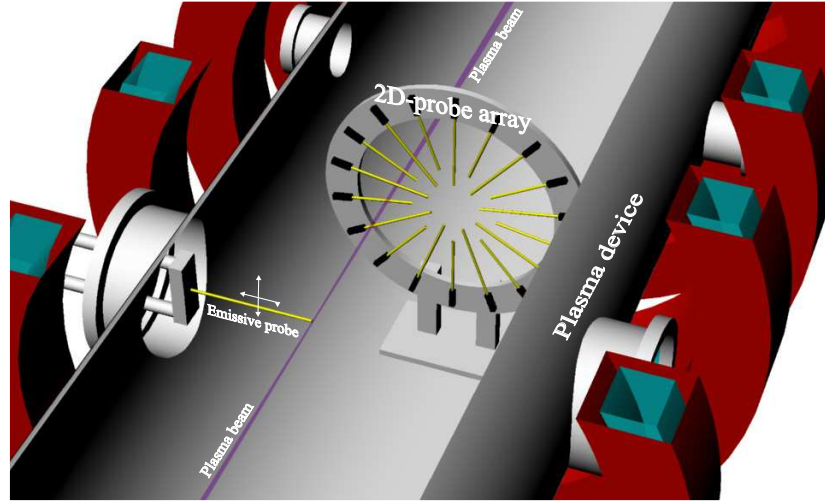


Figure 5.1: 3D sketch used for the probe position estimation. The yellow bars indicate the ceramic supports of probes. The emissive probe is mounted on the 2D positioning system and produces a localized plasma beam along the magnetic field.

To determine the probe positions of the 2D array probes inside the vacuum vessel, a small plasma beam is created using an emissive probe fixed on the 2D positioning system (Fig. 5.1). At a magnetic field of  $\sim 0.1$  T the emitted electrons are magnetized, i.e. their gyroradius is of the order of a few  $\mu m$ , and leads to a magnetized localized plasma production along the flux tube. The current carried by the emitted electrons along the magnetic field line is measured in the azimuthal plane by the Langmuir probes of the array. By moving the beam across the whole azimuthal plane with 1 mm resolution, a beam profile is obtained at each probe position. Figure 5.2a shows the resulting profile of a single probe of the array. The information from all probes is shown in Fig. 5.2b. The broader beam profiles at the edges indicate the magnetic field inhomogeneity. The probe positions are determined from the maximum of the signal amplitude with an accuracy better than  $\pm 2$  mm.

The accuracy in determining the probe positions can be improved using a higher resolution method, namely a high resolution picture of the probe array. For this reason a 5 Mega pixels camera is used. The picture of the array is taken from far away to reduce the lens boundary effects of the camera. Further the picture is re-scaled in the computer to the original size using the background circles, Fig. 5.3. The results are in good agreement with the previous method, i.e. blue stars denote the probe position estimated by the beam method. Hence, the image is used to determine the probe position relatively to each other with high accuracy, while the beam method gives the absolute positions with respect to the KIWI device, i.e. other probes being used.

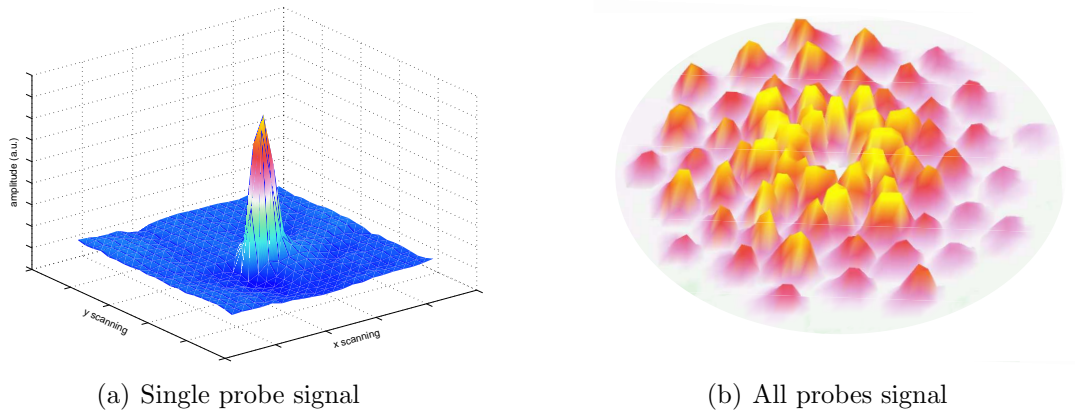


Figure 5.2: The electron current signal picked up by the array probes. These profiles are obtained by scanning the area around each probe of the array with the emissive probe.

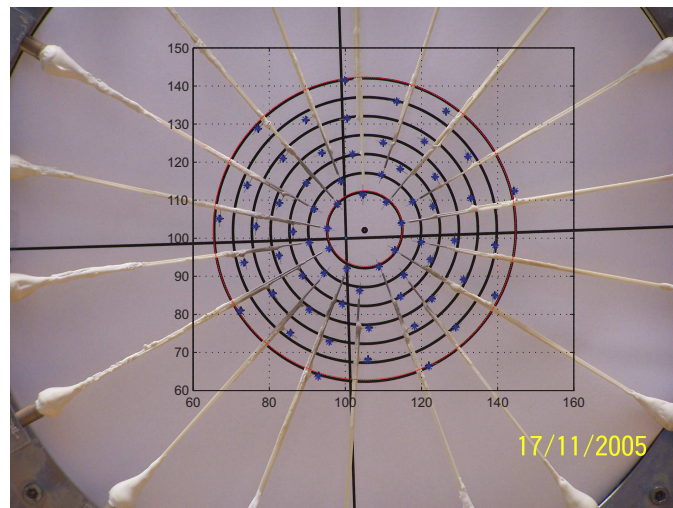


Figure 5.3: Picture of the probe array used for the optical estimation of the probe positions. The blue stars indicate positions determined by the beam method. The attached scale indicates our conventional positions of the 2D positioning system inside of the vacuum vessel.

## 5.2 The probe size calibration

Unfortunately, the method of probe positions estimation can not be used for the probe size estimation due to the spatial variation of the beam profile (Fig. 5.2b) and because of the probe surface contamination, i.e. by glue, which can not be observed with the camera. To estimate the probe size, an algorithm which uses real measured data from the drift wave regime is developed. The algorithm is based on the spatio-temporal constancy of the drift mode structures in the monochromatic wave regime. Based on the fact that a monochromatic mode propagates only azimuthally with constant amplitude, the probes at different azimuthal positions should see the same fluctuation amplitude if they have similar radial position. Furthermore, by investigation of the drift wave amplitude using two probe technique (see Chapter 3) it was found that the radial shape of the mode structure can be well approximated by a smooth function, e.g. a 5th order polynomial function. Assuming that the amplitude variation along azimuthal direction can be caused only by probe length deviation, it is possible to estimate the probe size. For a better understanding of the probe size calibration algorithm, it will be applied first to synthetic data.

### Synthetic data

The synthetic data consists of 4 gaussian structures (2 negative, 2 positive) with constant amplitude. They are simulated to move azimuthally around the probe array center. This way an  $m=2$  drift mode from KIWI is simulated. The signal of the simulated data taken at the probe positions is shown in Fig. 5.4a. The black dots indicate the probe position as estimated in the previous section. The data is represented on higher resolution grid by simple interpolation. By imposing a random probe size distribution of maximum  $\pm 20\%$ , a small amplitude disturbance can be seen in Fig. 5.4b. On this way the real experimental situation is quite well simulated. A calibration algorithm should now be able to recover the original synthetic data. In order to quantify the fluctuation magnitude the signal standard deviation (see data analysis methods in Chapter 2) is used. Fig. 5.4d indicates the standard deviation map of distorted data from Fig. 5.4b.

The radial dependence of the measured fluctuation magnitude, i.e. its standard deviation, accord with the center of gyration of structures is plotted in Fig. 5.4c. It shows (red stars) large variations from the original fluctuation amplitude (blue stars). However, a simple 5th order polynomial fit (black stars) to the data (red stars) well approximates the original values (blue stars). Obviously, the calibration factors can be estimated by the ratio of raw values and fitted values. Applying the calibration factors on distorted probe signals the original Gaussians are entirely recovered. The standard deviation map of calibrated probes signals is depicted in Fig. 5.4e.

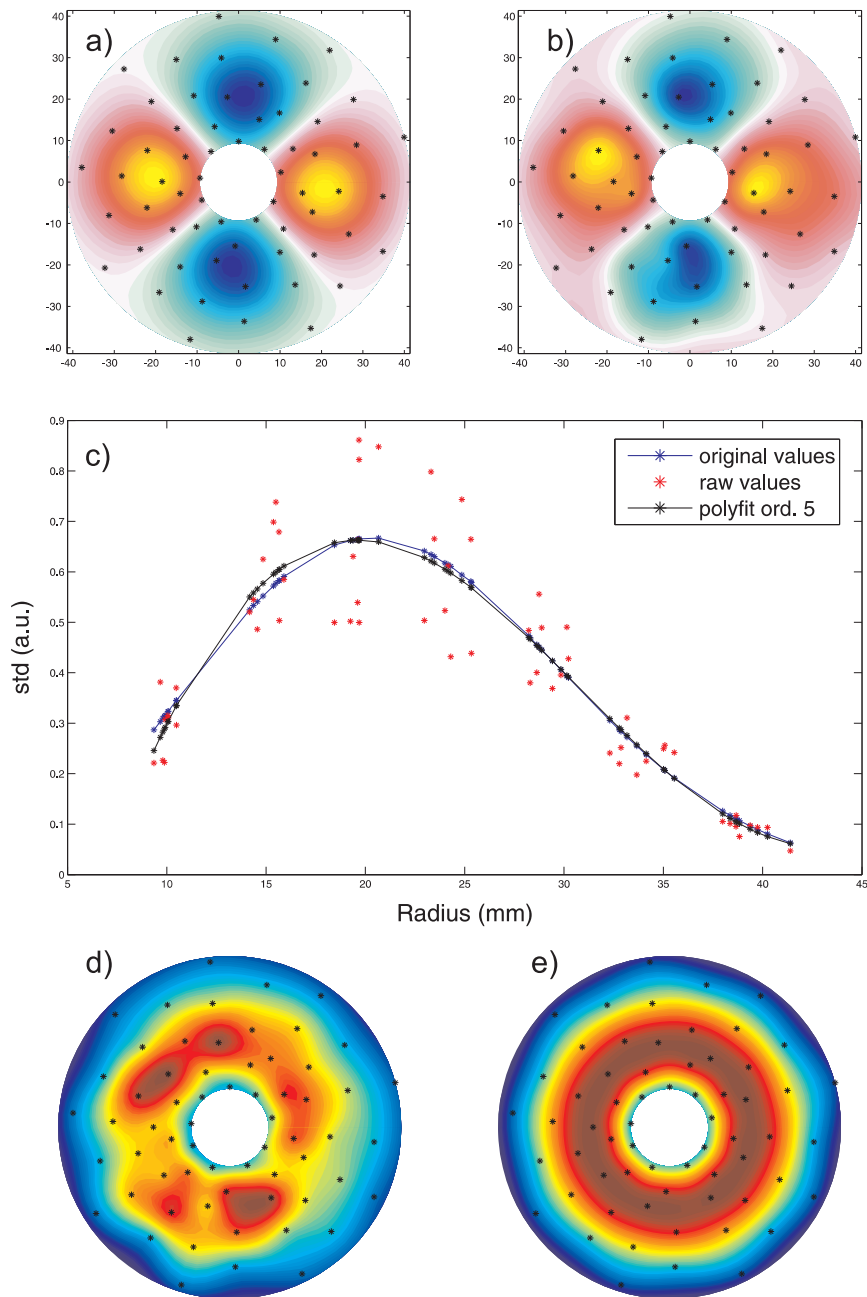


Figure 5.4: Synthetic data used to prove the calibration algorithm. (a) The original synthetic data (b) the distorted synthetic data by imposing probe size errors of maximum  $\pm 20\%$  (c) the radial dependence of the fluctuations amplitude (d) the standard deviation map of the distorted data (e) the standard deviation map of the recovered data.

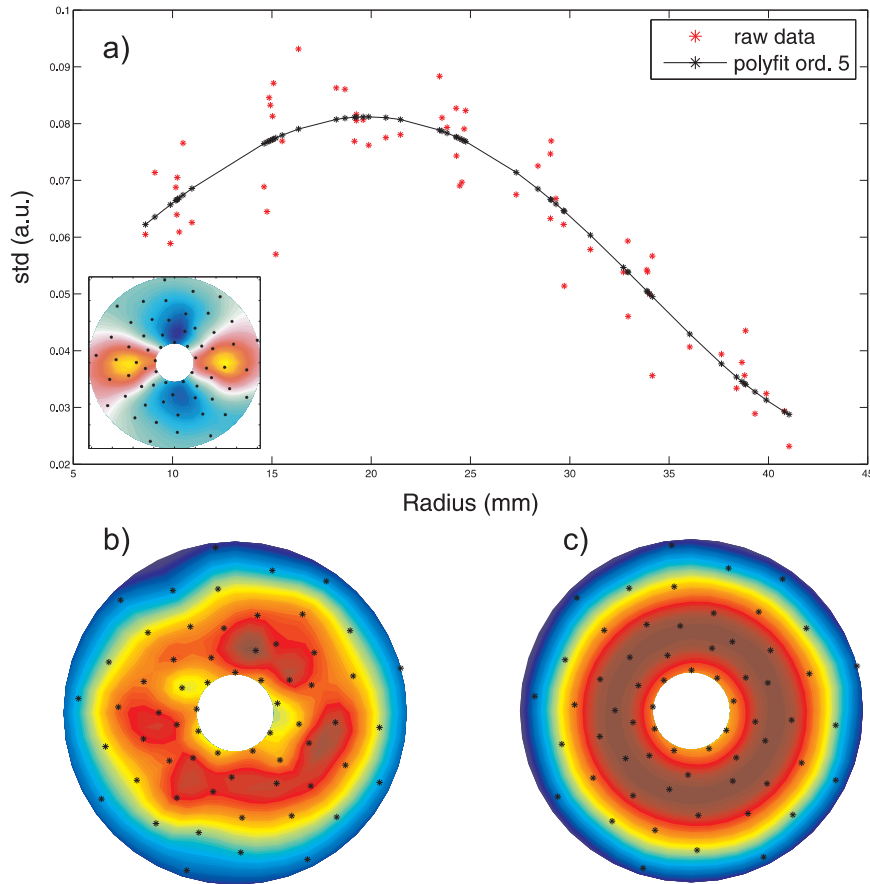


Figure 5.5: Experimental data used for the probe array calibration. (a) A snap shot of the drift waves mode is indicated in the left corner. The large diagram shows the radial dependence of the drift wave magnitude, while (b) and (c) indicate the 2D standard deviations maps before and after calibration.

### Experimental data

To estimate the probe size of our 2D probe array the same algorithm of calibration is applied to the experimental KIWI data. For this reason monochromatic drift wave data is recorded using the 2D probe-array. A snap shot of the data is shown in the left lower corner of Fig. 5.5a. It shows an  $m=2$  drift mode, which is a very stable mode in KIWI. The standard deviation map (Fig. 5.5b) indicates large variations in the fluctuation magnitude at probes along the azimuthal direction. The calibration factors are also determined by a simple 5th order polynomial fit (black stars) of the radial dependence of the signal standard deviation from the experiment (red stars) at all probes, Fig. 5.5a. The calibration results are shown by comparison of standard deviation maps before Fig. 5.5b, and after calibration Fig. 5.5c. Obviously the azimuthal variations of the uncalibrated array (Fig. 5.5b) are removed by the proposed calibration scheme.

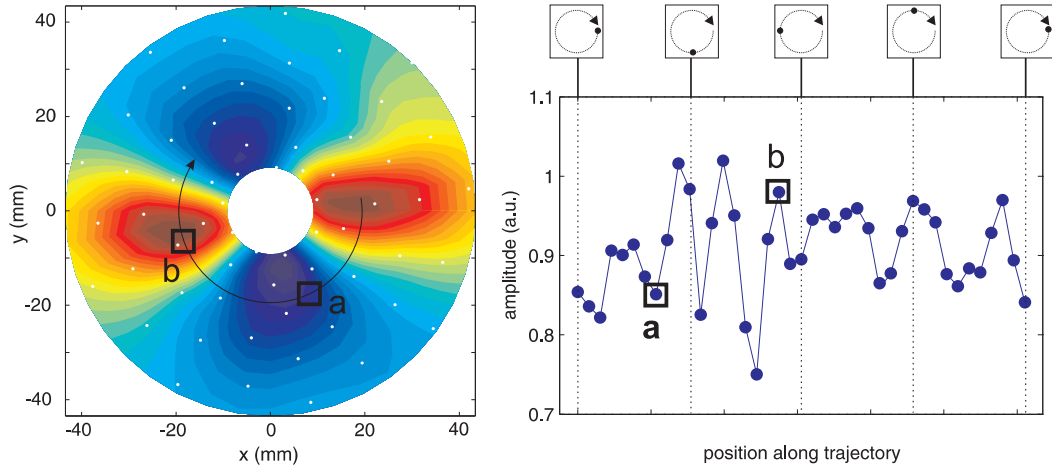


Figure 5.6: Amplitude evolution of density structures following the trajectory of the structure for a monochromatic drift wave regime in the KIWI device. a) A snapshot of the investigated drift mode ( $m=2$ ). The black arrow denotes the structure trajectory. b) Structure amplitude along its trajectory. The five sketches from above visualize the position of the density-structure (dot) along the trajectory (arrow).

Once the probe lengths are calibrated, the amplitude of the considered drift mode along its azimuthal trajectory should be constant. In order to test this aspect, it is worth to investigate the amplitude of one density maximum of the  $m=2$  drift mode in more detail (Fig. 5.6a). The amplitude dependence of the azimuthal position along its trajectory (black arrow) is represented in Fig. 5.6b. Although this is calibrated data, it shows large amplitude variations ( $\sim 20\%$ ) along the structure trajectory. The small boxes from above help to visualize the structure position. They indicate that amplitude variation is well correlated with the probes position (white dots in Fig. 5.6a), i.e. small values are observed when the structure is situated between probes and higher values when it is closer to a probe position. Therefore, the limited number of probes has a significant influence on the measured fluctuation amplitude and obviously the spatial resolution of the probe array is too poor. However, spatial under-sampling cannot be resolved by increasing the number of probes, as this would cause a notable plasma disturbance. Furthermore, typical discharge parameters in KIWI (see Table 2.1) require at least a distance of 5 mm between two probes to regard them as independent. Hence, a probe density of 1 probe/ $1\text{cm}^2$  can be regarded as a maximum value for KIWI. Finally this means that a different approach is needed to overcome the spatial under-sampling problem.





# Chapter 6

## Super-resolution methods

In this chapter a super-resolution algorithm for image processing is discussed in detail and an adapted algorithm for low resolution 2D-probe arrays is proposed. First, the basics about super-resolution techniques used for image improvement in *computer vision* are presented. The requirements for these methods are discussed and compared with conditions available in plasma diagnostics. Further, an algorithm based on cross-correlation analysis is adapted to 2D-probe arrays. Problems due to the extremely low resolution of these common spatio-temporal plasma diagnostics with respect to standard super-resolution techniques are discussed. The results of standard super-resolution and the proposed method are compared in the last part of the chapter.

### 6.1 Super-resolution for image processing

Turbulence studies in fluids and plasmas have shown that high spatial and temporal resolutions are needed to gain insight e.g. into the various transport processes being involved in fusion devices [41, 42, 43]. On the other hand, the necessity to have image and video with higher and higher resolution is found in many other fields, e.g. scientific (medical, space exploration, surveillance) and commercial (entertainment, high definition television) applications [97, 98, 99].

Increasing the resolution of the imaging sensor is clearly one way to increase the resolution of the acquired images. In image processing this solution may not be feasible due to the increased associated cost and the fact that shot noise increases during acquisition as the pixel size becomes smaller. In several other cases a huge number of pixels is not feasible due to the size restrictions of the sensor, data storage and transfer rates. In plasma diagnostics direct imaging is possible in fusion devices, [45, 46], but the resolution is below Megapixels and the method is very demanding and not applicable in general. For common diagnostic tools such as electrostatic probes or spectroscopic methods, the resolution is too poor for advanced turbulence

investigations. Therefore, post processing algorithms are required to increase the spatial resolution. To find a solution we just looked to other fields, i.e. *computer vision*, to see how the resolution problem is approached. A solution is provided by *super-resolution* algorithms which are well established methods in the field of *computer vision*.

### 6.1.1 Super-resolution definition and requirements

Super-resolution (SR) is a post processing algorithm to reconstruct a higher resolution image from several low resolution input images [100, 101, 102]. From the beginning it has to be clarified that the main requirements for the super-resolving procedure are the following: (i) the low spatial resolution inputs have to be globally or locally shifted images of the same spatial information and (ii) there is no temporal variation of the spatial information. Whereas in the traditional single image restoration problem only a single image is available for processing, the task of reconstructing high resolution images from multiple low resolution frames can take the advantage of the additional spatio-temporal information available from the image sequence. The basic idea is that low resolution images contain similar but not identical information which make possible the reconstruction of a frame with higher resolution than the original one. An important aspect which has to be kept in mind is that super-resolution is not applied routinely for every image requiring enhancement. In fact, it is a hand-crafted approach that requires individual parameter tuning for each image. One automated solution for all types of images is not possible.

### 6.1.2 Super-resolution algorithm

In the most general case a super-resolution algorithm requires three steps:

**A.** At the first step, *image recording*, a number of low resolution images of a static or moving scene is recorded. These low resolution observations are related by local or global sub-pixel shifts due to the object or camera motion.

**B.** *Sub-pixel shift estimation* (local displacement vectors) is the second step of SR procedure. Approximate calculation of local displacement vectors is usually based on the analysis of optical flow. Optical flow is defined as the change of image brightness in consecutive images. On the assumption that these changes of image irradiance are caused by absolute object (camera) motion, the optical flow allows to approximate well the local displacement vectors. The optical flow can not always be identified with local displacements. For example consider a rotating sphere without any surface texture. No optical flow can be observed even though a motion of object points occurs. On the other hand, for a static object and changing lighting conditions an optical flow can be observed for the object surface although no motion of

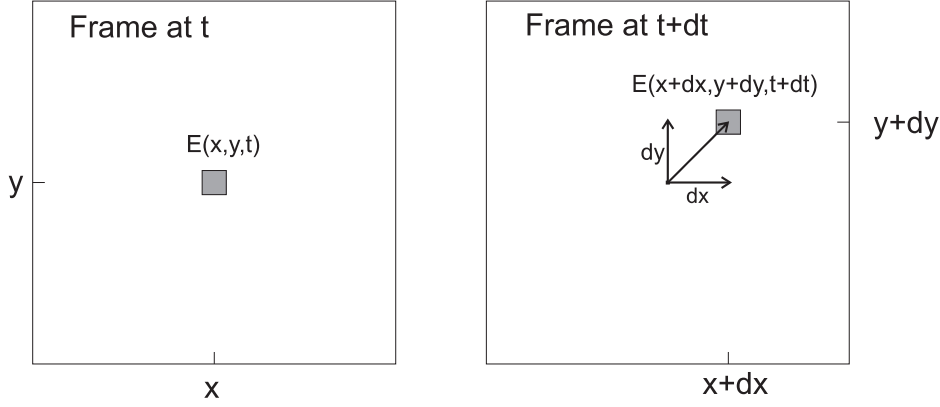


Figure 6.1: The optical flow at the pixel  $(x, y)$  is the 2D-velocity vector  $(v_x, v_y) = \left(\frac{\delta x}{\delta t}, \frac{\delta y}{\delta t}\right)$

surface takes place. The optical flow can also depend on instability of the camera sensor, on changing illumination, or on different surface appearance for different viewing directions. Thus it is clear from the beginning that optical flow only allows to approximate local displacement vectors. Besides these particular limitations of the optical flow, it yields good results if applied under reasonable conditions.

To understand the basic idea of optical flow computation let us consider the image brightness at the point  $(x, y)$  in the image plane at  $t$  be denoted by  $E(x, y, t)$ , (Fig. 6.1). Consider a patch of the image brightness pattern that is displaced a distance  $\delta x$  in  $x$ -direction and  $\delta y$  in  $y$ -direction in time  $\delta t$ . The brightness of the patch is assumed to remain constant so that:

$$E(x, y, t) = E(x + \delta x, y + \delta y, t + \delta t). \quad (6.1)$$

By Taylor expanding the right-hand side about the point  $(x, y, t)$  we get,

$$E(x, y, t) = E(x, y, t) + \delta x \cdot \frac{\partial E}{\partial x} + \delta y \cdot \frac{\partial E}{\partial y} + \delta t \cdot \frac{\partial E}{\partial t} + \epsilon, \quad (6.2)$$

where  $\epsilon$  contains the second and higher order terms in  $\delta x$ ,  $\delta y$  and  $\delta t$ . After subtracting  $E(x, y, t)$  from both sides and dividing through by  $\delta t$  we have:

$$\frac{\delta x}{\delta t} \cdot \frac{\partial E}{\partial x} + \frac{\delta y}{\delta t} \cdot \frac{\partial E}{\partial y} + \frac{\partial E}{\partial t} + \frac{\delta \epsilon}{\delta t} = 0. \quad (6.3)$$

In the limit as  $\delta t \rightarrow 0$  this becomes:

$$\frac{\delta x}{\delta t} \cdot \frac{\partial E}{\partial x} + \frac{\delta y}{\delta t} \cdot \frac{\partial E}{\partial y} + \frac{\partial E}{\partial t} = 0, \quad (6.4)$$

which is known as optical flow constrain equation.

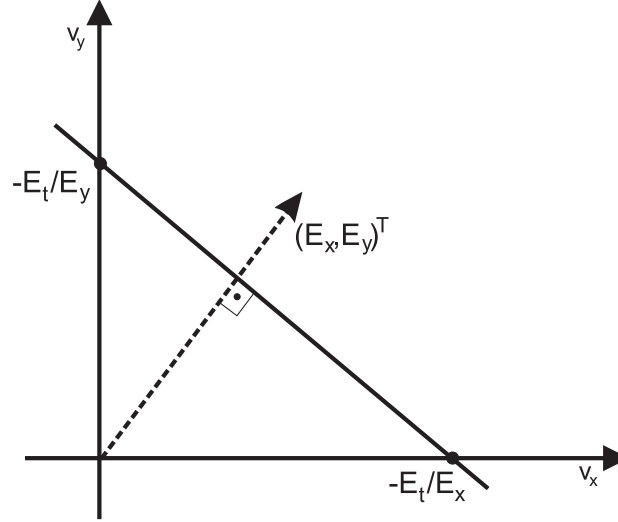


Figure 6.2: The constrain equation restricts the possible range of the optical flow onto a straight line in velocity space.

If we take

$$v_x = \frac{\delta x}{\delta t} \text{ and } v_y = \frac{\delta y}{\delta t}, \quad (6.5)$$

then for a certain moment in the image sequence the optical flow constrain equation has the form:

$$E_x \cdot v_x + E_y \cdot v_y + E_t = 0 \text{ or } (E_x, E_y)(v_x, v_y)^T = -E_t \quad (6.6)$$

where  $v_x$  and  $v_y$  depend on  $(x, y)$  and where the partial derivatives of image brightness depend on  $(x, y, t)$ . Therefore, the values of  $(v_x)$  and  $(v_y)$  for a particular image point  $(x, y)$  are restricted by this linear equation (Eq. 6.6). Only the perpendicular component of the movement in the direction of the brightness gradient can be estimated by:

$$v_{\perp} = -\frac{E_t}{\sqrt{E_x^2 + E_y^2}}. \quad (6.7)$$

The ambiguity of a solution  $(v_x, v_y)$  on the line  $v_x \cdot E_x + v_y \cdot E_y = -E_t$  corresponds to the *aperture problem* [103, 104] in computer vision field as is illustrated in Fig. 6.2, i.e. the degree of freedom for motion analysis if only local information is analyzed and/or available. However, the component of the movement in the direction of the iso-brightness contours, at right angle to the brightness gradient, can not be determined. As a consequence, the flow velocity  $(v_x, v_y)$  can not be computed locally without introducing additional constraints.

Although, across the time various methods of optical flow estimation have been proposed (first order Taylor series, correlation with zero padding, cross correlation with phase fitting, lock matching methods), the most successful ones are based on the optical flow constraint equation [105, 106, 103, 104, 107]. Furthermore, different

solutions have been proposed to resolve this equation (Eq. 6.6). Horn&Schunck [106] are the first who have proposed an iterative solution of Eq. 6.6. Lucas&Kanade [105] solution of optical flow equation suppose that neighboring pixels have the same flow vectors. Peleg&Irani [107, 108] decompose the object (camera) motion to polar coordinates in radial translation and azimuthal rotation of the object (camera). All of them conduct to reliable results of optical flow and can be adapted to a variety of specific situations.

Starting from the assumption that neighboring surface points of a dynamic, rigid object have approximately the same local displacement vectors, one way to express additional constraint is to minimize the square of the magnitude of the gradient of the optical flow velocity (smoothness of the optical flow field)

$$\left(\frac{\partial v_x}{\partial x}\right)^2 + \left(\frac{\partial v_x}{\partial y}\right)^2 + \left(\frac{\partial v_y}{\partial x}\right)^2 + \left(\frac{\partial v_y}{\partial y}\right)^2. \quad (6.8)$$

For the set of all image points for which the optical flow has to be calculated the global constraint means that functional:

$$F_s(v_x, v_y) = \int \int \left( \left(\frac{\partial v_x}{\partial x}\right)^2 + \left(\frac{\partial v_x}{\partial y}\right)^2 + \left(\frac{\partial v_y}{\partial x}\right)^2 + \left(\frac{\partial v_y}{\partial y}\right)^2 \right) dx dy. \quad (6.9)$$

has to be minimized.

Since the optical flow constraint equation has to be satisfied at the same time for all image points of a given image sequence for a moment  $t$ , a solution for  $(v_x, v_y)$  for this time  $t$  also has to minimize the functional:

$$F_o(v_x, v_y) = \int \int (v_x(x, y) \cdot E_x(x, y) + v_y(x, y) \cdot E_y(x, y) + E_t(x, y))^2 dx dy. \quad (6.10)$$

This functional indicates the error concerning the validity of the optical flow constraint equation for a function pair  $(v_x, v_y)$ .

The functionals  $F_s$  and  $F_o$  can be weighted by a weighting parameter  $\lambda \geq 0$ . The total error which has to be minimized

$$F_{HS}(v_x, v_y) = F_s(v_x, v_y) + \lambda \cdot F_o(v_x, v_y) \quad (6.11)$$

is the key equation in the Horn-Shunck method of the optical flow estimation, [106]. The variation calculus (use of Euler equations) provides a pair

$$\begin{aligned} \nabla^2 v_x &= \lambda \cdot (v_x \cdot E_x + v_y \cdot E_y + E_t) \cdot E_x \\ \nabla^2 v_y &= \lambda \cdot (v_x \cdot E_x + v_y \cdot E_y + E_t) \cdot E_y \end{aligned} \quad (6.12)$$

of partial elliptic second order differential equations for the solution. A system of partial differential equations has generally an infinite number of solutions. By specifying boundary conditions a unique solution can be determined. Numerical iteration

technique can be used for this solution strategy. A second solution strategy of the optimization problem is given by the use of a discrete iteration scheme starting with some selected initial values.

In the discrete case the smoothness error of the (discrete) optical flow field  $(v_x, v_y)$  in point  $(i, j)$  can be estimated by simple differences of function values in the neighboring image points:

$$F_s(i, j) = \frac{1}{4} \cdot ((v_x(i+1, j) - v_x(i, j))^2 + (v_x(i, j+1) - v_x(i, j))^2) + \frac{1}{4} \cdot ((v_y(i+1, j) - v_y(i, j))^2 + (v_y(i, j+1) - v_y(i, j))^2) \quad (6.13)$$

for a particular time  $t$ . The error of optical flow constraint can be estimated by:

$$F_o(i, j) = (E_x(i, j, t) \cdot v_x(i, j) + E_y(i, j, t) \cdot v_y(i, j) + E_t(i, j, t)). \quad (6.14)$$

Altogether the minimization problem

$$F_{HS}(i, j) = \sum (F_s(i, j) + \lambda \cdot F_o(i, j)) \rightarrow \text{minimum}. \quad (6.15)$$

The minimization assumption impose that partial derivatives  $\frac{\partial F_{HS}}{\partial v_x}$  and  $\frac{\partial F_{HS}}{\partial v_y}$  have to be set equal to zero to determine the arguments at the minimum. This leads to the set of equations:

$$\begin{aligned} (1 + \lambda \cdot E_x^2) \cdot v_x + \lambda \cdot E_x \cdot E_y \cdot v_y &= (\bar{v}_x - \lambda \cdot E_x \cdot E_t) \\ \lambda \cdot E_x \cdot E_y \cdot v_x + (1 + \lambda \cdot E_y^2) \cdot v_y &= (\bar{v}_y - \lambda \cdot E_y \cdot E_t), \end{aligned} \quad (6.16)$$

where:  $\bar{v}_{x,y}(i, j) = \frac{1}{4} \cdot (v_{x,y}(i+1, j) + v_{x,y}(i, j+1) + v_{x,y}(i-1, j) + v_{x,y}(i, j-1))$ , or local averages values.

The general solution of this set of linear equations is given by

$$\begin{aligned} v_x &= \frac{1}{1 + \lambda \cdot (E_x^2 + E_y^2)} [(1 + \lambda \cdot E_y^2) \cdot \bar{v}_x - \lambda \cdot E_x \cdot (E_t + E_y \cdot \bar{v}_y)] \\ v_y &= \frac{1}{1 + \lambda \cdot (E_x^2 + E_y^2)} [(1 + \lambda \cdot E_x^2) \cdot \bar{v}_y - \lambda \cdot E_y \cdot (E_t + E_x \cdot \bar{v}_x)]. \end{aligned} \quad (6.17)$$

This given solution of  $v_x, v_y$  depend on the values of  $v_x$  and  $v_y$  in the 4-neighborhood, i.e. the solution can not be determined simultaneously for various image points just based on this solution. However, these formulas support an iterative solution strategy. Altogether this specifies the *Horn-Shunck algorithm* [106] for calculating optical flow fields. The iterative solution steps are given by the iteration formulas:

$$\begin{aligned} v_x^{n+1} &= \bar{v}_x^n - \frac{E_x \cdot \bar{v}_x^n + E_y \cdot \bar{v}_y^n + E_t}{1 + \lambda \cdot (E_x^2 + E_y^2)} \cdot \lambda \cdot E_x \\ v_y^{n+1} &= \bar{v}_y^n - \frac{E_x \cdot \bar{v}_x^n + E_y \cdot \bar{v}_y^n + E_t}{1 + \lambda \cdot (E_x^2 + E_y^2)} \cdot \lambda \cdot E_y, \end{aligned} \quad (6.18)$$

where  $n = 1, 2, 3, \dots$  denotes the iteration step. In every iteration step the values of the optical flow are calculated at all image points. The weighting factor  $\lambda$  and the iteration number are free parameters of the technique.

C. In the last step of the super-resolution algorithm the information of optical flow/sub-pixel shifts is used to *fuse the images* by adding additional pixels in a master frame. The result is an image which contains the pixels of all images, but they are not placed on a regular grid. The re-sampling process to a regular grid can be made directly using simple least square plane fitting, bilinear interpolation schemes, normalized convolution or iterative reconstruction.

## 6.2 Super-resolution for plasma diagnostics

Although, many super-resolution algorithms are described in literature [101] they are not directly applicable to spatio-temporal plasma diagnostics. With respect to the first step in super-resolution no severe problems are found. The diagnostic tools are usually fixed with respect to the plasma but the plasma is not static. On the one hand, strong plasma drifts ( $E \times B$ ) exist in many cases, which cause a relative motion of camera or object. On the other hand, the structures in turbulence are in principle not static. However, due to the high temporal resolution of the diagnostics the structures can be regarded as quasi-static, i.e. typically their propagation is resolved while their amplitude and shape are practically unchanged. Hence, it is no problem to produce a series of shifted low-resolution images of the same turbulence scene. The second step in super-resolution bears significant difficulties. They are introduced by the extreme spatial under-sampling, i.e. the low number of pixels. Based on few pixels with rather large spatial separation spatial correlation techniques and block matching algorithms fail. Even the commonly used estimation of optical flow with first order Taylor expansion is not suitable as it needs the spatial derivative of each single image. For extreme spatial under-sampling the numerical estimation of spatial gradients is subject to high errors and thus the resulting velocity field is strongly distorted. Hence, the fusion of images does not lead to reliable results. As a consequence, super-resolution for plasma diagnostics should base on the high temporal resolution to estimate the velocity field. In many cases sample rates of 1 Msample (Mega sample) are achieved, which is almost one order of magnitude higher than necessary. The idea to use this wealth of information to improve the spatial resolution is presented in the following section.

### 6.2.1 Super-resolution algorithm for 2D probe arrays

Common spatio-temporal diagnostics rely on 2D probe-arrays. As shown in previous chapter their spatial resolution is critical. Technically, increasing the probe number is not possible, but post processing algorithms such as super-resolution based on the

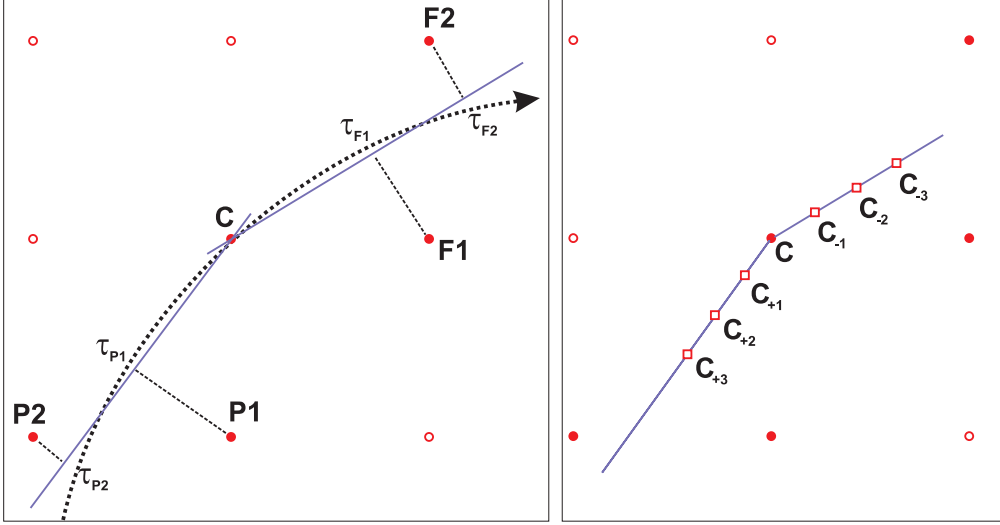


Figure 6.3: Visualization of correlation approach to estimate the velocity at pixel  $C$ . Pixel without significant correlation are represented by open circles. Those pixels whose cross-correlation with  $C$  has positive values for the position of maximum correlation  $\tau_X$  are labeled  $X \sim F1$  and  $X \sim F2$ . Pixel with negative values of  $\tau_X$  are labeled  $X \sim P1$  and  $X \sim P2$ . (a) shows the real trajectory (dashed line) and the estimated trajectory (solid line). The positions  $\tau_X$  of maximum correlation, i.e. closest distance of  $X$  and the estimated trajectory are indicated by dots. (b) the mapping of future and past amplitude information to the trajectory is shown.

high temporal resolution should be possible. Therefore, an adapted super-resolution algorithm for 2D-array is further proposed. To remain in accordance with image processing and its established notations, especially to allow for a clear reference either to plasma physics or to image processing, *probe* and *pixel* are considered equivalent throughout this chapter.

In order to estimate the local displacement vectors needed in the second step of the super-resolution algorithm, a method based on temporal correlation analysis, which is a well established method in turbulence [73], is developed. The general idea is to use maximum crosscorrelation of the time trace of neighboring pixels for structure tracking (see Fig.6.3). To estimate the velocity at pixel  $C$  at  $t_0$  a short timeserie  $r_C(t)$  is chosen with  $t \in [t_0 - \Delta t, t_0 + \Delta t]$ . Here,  $\Delta t$  depends on the system characteristics, and must be larger than the ratio of structure size and structure velocity. Further, the timeseries should not be too long in order to correlate only local information and to obtain a well localized estimation of the velocity field. First the crosscorrelation of  $r_C(t)$

$$C_{C,X}(\tau) = \int r_C(t)r_X(t + \tau)d\tau \quad (6.19)$$



with all neighboring points  $X$  is computed directly, i.e. without use of Wiener-Khintchine theorem [109].

If a significant correlation is observed, the time lag  $\tau_X$  is determined from maximum correlation for each of them. Further, points with positive and negative  $\tau_X$  are grouped to solve Eq. 6.20 for each group separately. The two pixels  $X = F1, F2$  (i.e.  $X = P1, P2$  for positive  $\tau$ ) with highest correlation are used to compute the velocity. As illustrated in Fig. 6.3a, the position of maximum correlation for a propagation with constant velocity corresponds to the perpendicular projection of  $X$  to the trajectory. Hence, using Pythagorean theorem  $\vec{v}_+ = (v_x, v_y)$  is obtained by solving the equation:

$$(v_x^2 + v_y^2)\tau_X - v_x(x_X - x_C) - v_y(y_X - y_C) = 0, \quad (6.20)$$

for  $X = F1, F2$ .  $\vec{v}_-$  is obtained respectively by using  $X = P1, P2$  instead. The local velocity at pixel  $C$  is finally described by the mean value of  $v_+$  and  $v_-$ .

Once the velocity field (displacement vectors) is known the fusion of images is straight forward. Starting with the image at  $t_0$ , additional pixels with  $r_C(t) = r_C(t_0 \pm n \cdot \delta t)$  are added along the streamline Fig. 6.3b.  $\delta t$  is the inverse sample rate and the integer number  $n$  is locally limited in order to obtain full coverage between original pixel. They reflect the future and past amplitude evolution at pixel  $C$ . Finally, the fused image is interpolated to fill a regular grid using biharmonic splines. This scheme is a well established interpolation technique used for surface topography maps in satellite data [110] and avoids spurious overshooting known for simple spline interpolation. Other reconstruction schemes, used in machine vision, e.g. normalized convolution, exact or iterative construction [111] are much more expensive to compute and do not give better results.

## 6.2.2 Optical flow vs. displacement vectors

To test the proposed algorithm of displacement vectors estimation for 2D-probe arrays, it is applied on synthetic data consisting of a gaussian structure with normalized amplitude mapped on a  $15 \times 15$  grid (Fig. 6.4). It moves along the dashed line with constant velocity. By using the standard method used in computer vision based on iterative solution of Eq. 6.6, as presented in the section 6.1.2, the displacement vectors are shown in Fig. 6.4a. They do not show parallel and equal vectors as expected. Spatial variation of estimated vectors is caused by poor gradients information. Using the correlation based algorithm, special designed for 2D-probe array with spatial under-sampled data, the estimated vectors are denoted in Fig. 6.4b. Clearly the proposed algorithm gives a better estimate of displacement vectors. They are all parallel to the real direction of structure motion (dashed line) and their constant magnitude corresponds to the original value.

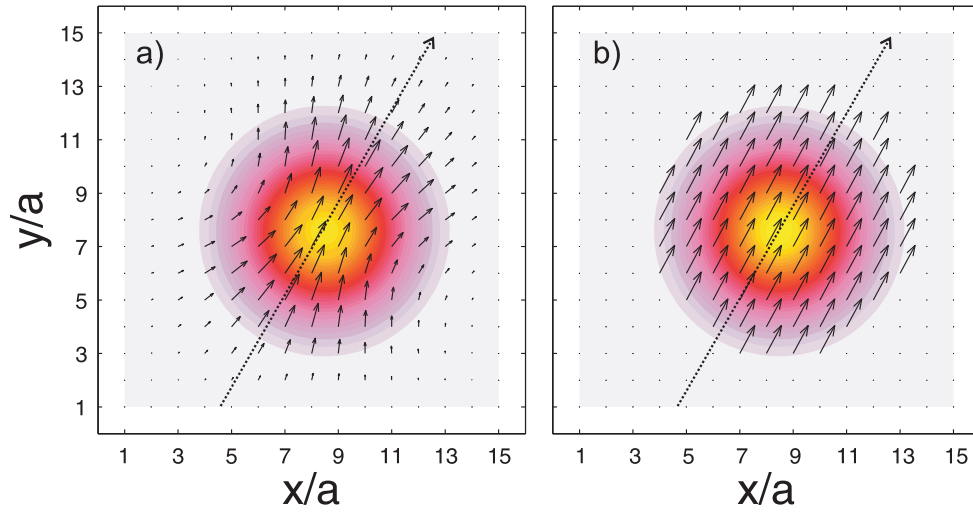


Figure 6.4: Velocity field computed with first order Taylor expansion [106] (a) and our correlation based algorithm (b) for gaussian structure (color filled contours) with radius  $r = 2.5a$ , which propagates with constant velocity along the dashed line.

### 6.3 Remarks

This chapter proposed a super-resolution algorithm to enhance the spatial resolution of spatio-temporally resolved plasma diagnostics. This algorithm is taken from computer vision and adapted to 2D-probe arrays. Although the described algorithm is based on cartesian coordinates for the probe positions, it can easily be modified for different probe arrangements. It has to be pointed out that similar results have been found for equally distributed probes in poloidal coordinates. In principle, any probe array could be used. Even if the probe positions are subject of random displacements from strict ordering, the results are found to be similar. The performance of the algorithm will be tested in detail in the following chapter.

# Chapter 7

## Applications of super-resolution to plasma diagnostics

In this chapter the super-resolution algorithm proposed in the last chapter [112] is tested first on artificial data and then on typical turbulence data from experiment. For this reason first the adapted algorithm for 2D probe-arrays is tested on the simplest synthetic data of a single structure. To quantify the improvement of the method the main structure properties such as, amplitude, trajectory and shape are analyzed in detail. To test if super-resolution can manage complex situation, it is applied in the last part of the chapter to turbulence data from simulation.

### 7.1 Application to synthetic data

Typically, probe arrays are used to investigate plasma turbulence, e.g. to quantify the contribution of coherent structures to anomalous transport, to identify their instability mechanism, or to study nonlinear wave phenomena. In any case, amplitude, trajectory and shape of structures are of major interest. Hence, a performance test of our super-resolution algorithm has to focus on these quantities. In order to study them independently, the super-resolution algorithm is applied to synthetic data first. In the following we use a simple arrangement of  $8 \times 8$  probe on a square grid, which is quite typical for Langmuir probe arrays in several experiments [32, 24, 34, 35, 36, 37, 33]. For the following analysis the probe distance is arbitrary and the results depend on the ratio of structure size to probe distance only. Accordingly, the structure size is given in units of probe distance  $a$ .

The synthetic data consists of a gaussian structure with normalized amplitude mapped on a  $8 \times 8$  grid (Fig. 7.1). It moves along a linear trajectory with constant velocity. Its direction is chosen arbitrarily with respect to the grid with the only condition that it does not have any short-scale periodicity. Only a short part of structure path in the middle of the array is considered in the following to exclude

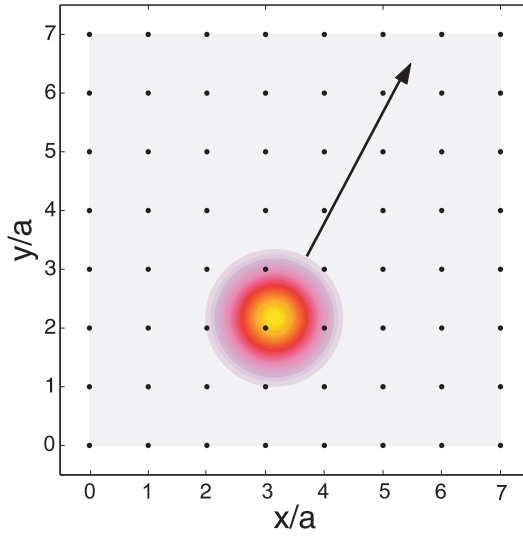


Figure 7.1: Visualization of synthetic data which is used to test the super-resolution algorithm. The dots indicate the probes/pixels arranged on a  $8 \times 8$  grid. The color filled contours represent the gaussian structure. It has constant amplitude. The arrow indicates the direction of propagation. The structure propagates with constant velocity.

effects of the array boundaries. Different structure sizes were used to generalize the analysis. To investigate the improvement of the super-resolution algorithm the main characteristics, i.e. amplitude, trajectory and shape, of the structure are compared in detail with and without application of the super-resolution. This means, the raw data set ( $8 \times 8$  pixel) and the super-resolved data set are interpolated with biharmonic splines to the same resolution. Hence, the differences are solely attributed to the use of super-resolution. In all graphs the simple interpolated raw data is represented by dashed lines and squares, while the super-resolved data is marked by solid lines and circles. The dotted lines refer to the gaussian structures and are plotted for reference.

### Amplitude

The structure amplitude is an important quantity as it determines the life time of a structure and its transport properties. First, the simple interpolated raw data is analyzed. The dashed blue line in Fig. 7.2 shows the maximum amplitude of a Gaussian and its temporal evolution along the trajectory as it is recovered without super-resolution. The structure radius is  $r \equiv \sigma = 0.5a$ , which is close to the spatial Nyquist limit. Clearly, the original amplitude is only recovered at a single position along the trajectory ( $x = 3$ ). At all other positions the measured amplitude is significantly lower. Further, the amplitude shows strong variations. Peak amplitude reductions of up to 45% are observed and on average only three quarter of

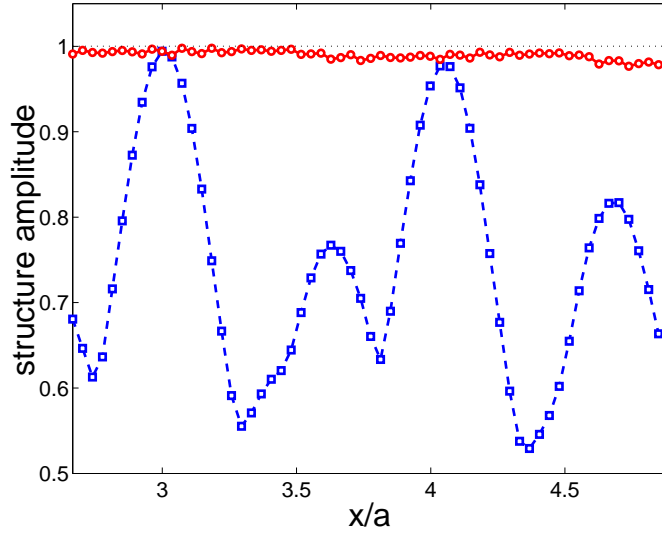


Figure 7.2: Structure amplitude along its trajectory (see Fig. 7.1). The position represented by the projection to the  $x$  coordinate and is given in units of the grid size  $a$ . The structure has a radius of  $r = 0.5a$ . The simple interpolated data is represented in dashed blue lines and squares, the super-resolved data is marked by red solid lines. The amplitude reference is shown by means of the black dotted line.

the original amplitude are recovered. A closer inspection of Fig. 7.3a and a comparison with Fig. 7.2 reveals that the original structure amplitude is resolved where the trajectory coincides with a probe position and that the amplitude minima are at positions where the distance between the structure maximum and neighboring probes is maximum. Hence, the measured amplitude evolution depends sensitively on the trajectory, i.e. its distance to the probes. However, similar behavior is found for any other trajectory. The same analysis can be made as a function of structure sizes. Structures with radius below  $r = 0.3a$  are not analyzed because they are so small that they are almost invisible for the probe array, i.e. they can propagate quite long distances without hitting a probe. Fig. 7.3 shows the mean (open blue squares) and minimum amplitude values (solid blue squares) obtained from simple interpolation (dashed blue lines) along the trajectory shown in Fig. 7.1. The curves show severe amplitude reduction with decreasing structure size. Further, the discrepancy of average and minimum amplitude increases with decreasing amplitude. This indicates that the overall amplitude variation along the trajectory increases. Furthermore, even for structures with radius  $r \geq a$ , significant amplitude deviations from the reference value (dotted black line) are observed. This means that even for large structures, which cover several probes at a time, the average amplitude is underestimated. Structures larger than  $r = \sigma \geq 1.5a$  are not shown because almost 100 % of the amplitude is resolved on average. Amplitude evolution of the same synthetic data using super-resolution is shown in Fig. 7.2 and Fig. 7.3 (solid red line with circles). Figure 7.2 shows that for identical conditions an almost constant

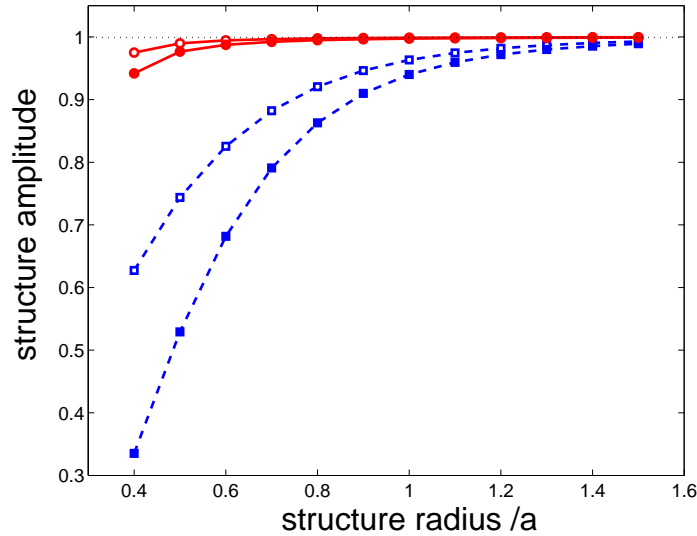


Figure 7.3: The mean (open markers) and maximum (solid markers) trajectory deviation along the trajectory is shown as a function of structure size. The simple interpolated data is represented dashed blue lines and squares, the super-resolved data is marked by solid red lines.

amplitude is now found along the trajectory. The variations are below 3%. Further, the amplitude is almost unity, i.e. agrees with the reference value (dotted black line). This is a significant improvement compared to the simple interpolated data (dashed blue line). Furthermore, this result even holds for the full spectrum of structure sizes (Fig. 7.3). For large structures the amplitude is fully recovered by super-resolution. Only for structure sizes  $r < 0.5a$  notable deviations are found, but they are still below 5% on average. For structure sizes  $r \leq 0.3a$ , the amplitude variation suddenly increases and almost approaches the value of the simple interpolated data, which is not surprising as the time trace of neighboring probes loses correlation due to the sporadic detection by probes.

Summarizing, Fig. 7.2 and Fig. 7.3 show that the amplitude information cannot be recovered with simple interpolation even in case of rather large structures, while super-resolution is capable to improve the amplitude evolution of the structures as long as the grid size is in reasonable agreement with the structure size.

## Trajectory

The capability of super-resolution to recover the structure trajectory is investigated in the following. A robust definition for structure trajectory is the position of a local amplitude maximum as function of time. Fig. 7.4 a shows the trace for the same Gaussian as in Fig. 7.2 and Fig. 7.3. The true trajectory is indicated by a dotted black line. The results of simple biharmonic spline interpolation of the data (dashed

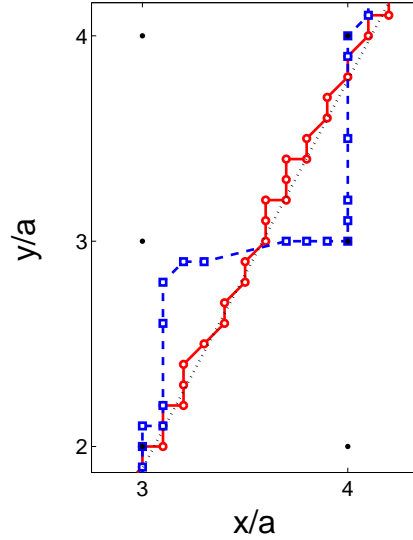


Figure 7.4: Short part of a typical structure trajectory for structure with radius  $r = 0.5a$ . The dots indicate the probe/pixel positions. The dotted black line is the real trajectory of the structure. The arrow represents the motion direction. The markers indicate the positions of the structure maximum.

blue line with squares) reveal two things. First, the detected structure maximum does not follow the dotted black line. Strong deviations are observed. The trajectory basically consists of orthogonal parts which are aligned with the grid vectors of the probe array. Second, although the maximum positions (blue squares) are measured with a fixed sample rate they are not uniformly distributed along the trajectory. They tend to focus close to probe positions and the measured structure velocity shows strong modulation. To quantify the result for different sizes of the structure the maximum and the mean deviation from real trajectory is computed using

$$\Delta = \frac{1}{N} \sum_{i=1}^N |f_{real}(x(t_i), y(t_i)) - f(x(t_i), y(t_i))|, \quad (7.1)$$

where  $f_{real}(x(t_i), y(t_i))$  is the original structure position and  $f(x(t_i), y(t_i))$  is the actual position obtained by simple interpolation at time  $t_i$ . Fig. 7.5 shows the result for simple interpolation (dashed blue line). Clearly, the trajectory deviation increases with decreasing structure size. For small structures maximum trajectory deviations (solid blue squares) are comparable with the half grid spacing. An analysis similar to Fig. 7.4 shows that this is caused by more and more step-like trajectories with increasing focus at probe positions. Further, Fig. 7.5 shows that significant deviations are observed even for structure radii which are comparable with grid spacing. For large structures the deviations approach the meshwidth of the interpolation grid. Basically, this means that the maximum is preferably detected at the probe positions and it tends to jump from one probe position to the next in order to stay closest to

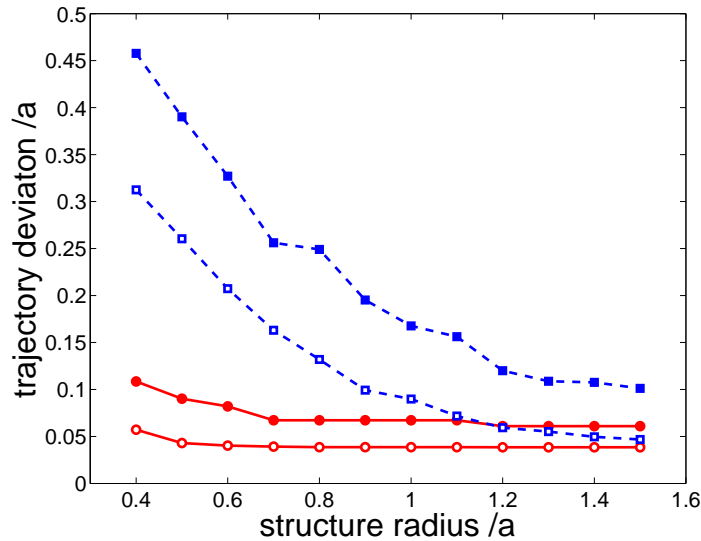


Figure 7.5: The mean (open markers) and maximum (solid markers) trajectory deviation along the trajectory is shown as a function of structure size.

the trajectory within a discrete grid. This is in good agreement with the observations made for amplitude evolution. If the maximum is found close to a probe position its value is given by the value measured with that probe. Hence, the further the probe and the trajectory are separated the more the maximum amplitude will deviate from unity. Additionally this effect becomes more dramatic with decreasing structure size. This is exactly what is observed in Fig. 7.4 and Fig. 7.5. The same analysis for super-resolution reveals that the trajectory (solid red line in Fig. 7.4) is closer to the real one. A nearly uniform distribution of maximum positions along trajectory is obtained and, therefore, the structure velocity is found almost constant. The mean trajectory deviation is almost independent of structure size (open red circles) and corresponds to half grid spacing of interpolated data. For small structures slight deviations from trajectory exist, but they are negligible.

Comparing Fig. 7.2 and Fig. 7.4 the errors in amplitude and trajectory are well correlated. Interpolation tends to put the maximum close to the probe if it is operated on spatially under-sampled data. Hence, no significant improvement can be obtained by simple interpolation. Obviously, super-resolution removes the spatial under-sampling and all subsequent problems with amplitude and trajectory.

## Shape

Reliable information on structure shape is important for several physical processes in plasma, e.g. mode structure [113, 114] or decorrelation by sheared flows [115]. For our synthetic data the shape of a Gaussian is represented by concentric, circular



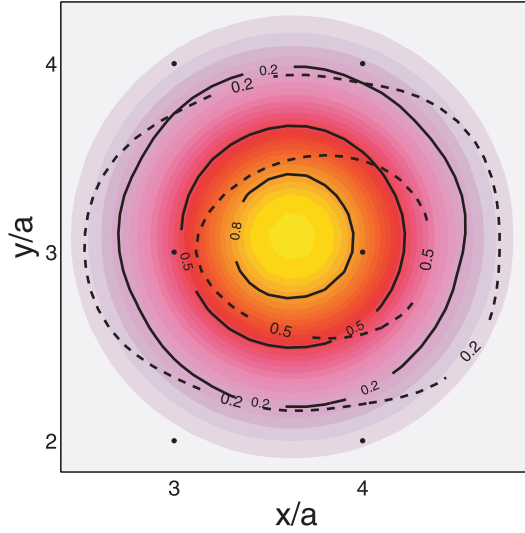


Figure 7.6: Example for shape deformation of a structure with  $r = 0.5a$ . Dashed line contours represent a structure obtained from simple interpolation. The super-resolved structure is represented by solid lines. In the background by color filled contours the original gaussian is posted.

contour lines. Fig. 7.6 shows the contour lines of a Gaussian with  $r = 0.5a$  for simple interpolated (dashed line) and super-resolved data (solid line). Clearly, simple interpolation of the spatially under-sampled data (dashed line) yields strong deformations (Fig. 7.6) from circular shape. On the contrary, super-resolution reproduces the circular shape almost perfectly. In order to quantify the shape deviation the root mean square displacement of the 50% contour is computed, i.e. for 100 equidistantly distributed points on the circular 50% reference contour the root mean square distance to the obtained contour is computed. Fig. 7.7 shows the result for various structure radii. To eliminate effects of amplitude and trajectory errors the structures are centered and rescaled to their original amplitude before computing the shape deviation. For structure radii larger than the grid size the shape deviations of simple interpolated (dashed line) and super-resolved (solid line) data are comparable. Both methods reproduce the circular shape quite well. For smaller structures the simple interpolation leads to significantly larger shape deviations. Basically, the observed structures are elliptical as shown in Fig. 7.6. The decrease in shape deviation for very small structures ( $r = 0.4a$ ) for simple interpolated data is attributed to the fact that structures which cover just one probe have to produce circular contour lines solely due to interpolation. Hence an analysis for structures with  $r \leq 0.3a$  is omitted here. As already mentioned, a typical situation where structure shape is of interest is found in shear flows. There, structures are stretched until they decorrelate into two separate structures. To check whether the resolution of super-resolution is sufficient to detect such process, two Gaussians with similar amplitude and radius  $r = 0.5a$  are placed with separation  $a$ . Fig. 7.8 shows the result obtained by simple

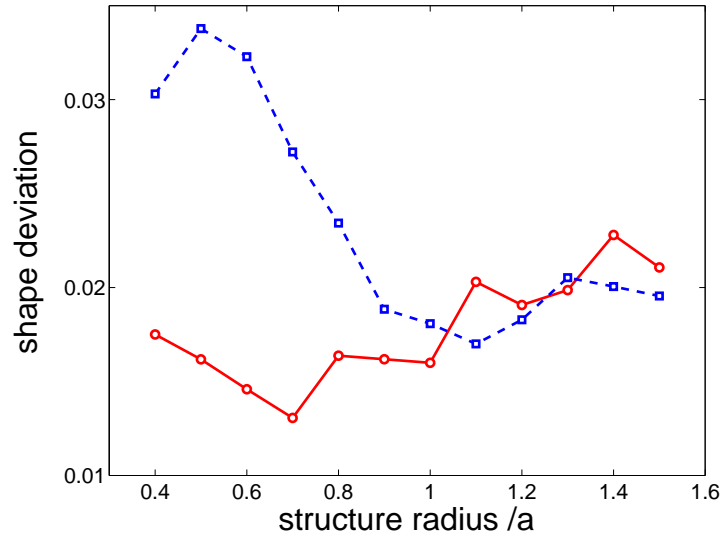


Figure 7.7: Shape deviation of 50% contour for different structure sizes. Dashed blue line indicates simple interpolation, the solid red line indicates super-resolution.

interpolation (dashed line) and super-resolution (solid line). While simple interpolation yields just one elongated structure with an eccentric maximum, super-resolution clearly resolves both maxima. Both maxima are found to have similar size, shape and amplitude and the contours are in close agreement with the original data. Hence, Fig. 7.8 shows that super-resolution improves the resolution, as it allows to separate two structures which are merged with simple interpolation.

## 7.2 Application to simulation turbulence data

So far the tests with synthetic data allowed to investigate the improvements obtained with super-resolution in detail. They allowed to study the working principle of the algorithm and to pinpoint the origin of observed deviations in amplitude, trajectory and shape. However the results were obtained for smooth, fully symmetric structures which propagate with constant velocity along a straight line without any other structure or noise being involved. From a practical point of view, this does not assure that the algorithm can handle complex situations like turbulence, where many irregular shaped structures are involved, which obey complicated rules of motion. In order to demonstrate the applicability of super-resolution to turbulence data without lacking a well defined reference, simulations based on the Hasegawa-Wakatani drift wave model [116] are performed. To be in close agreement with typical experimental conditions a constant drift velocity along the slanting direction with about 10 pixels per second is included. The simulation provides data with high spatial ( $256 \times 256$  pixel) and temporal resolution. A typical density fluctuations evolution with full spatial resolution is plotted in first row of pictures from Fig. 7.9. They denote three

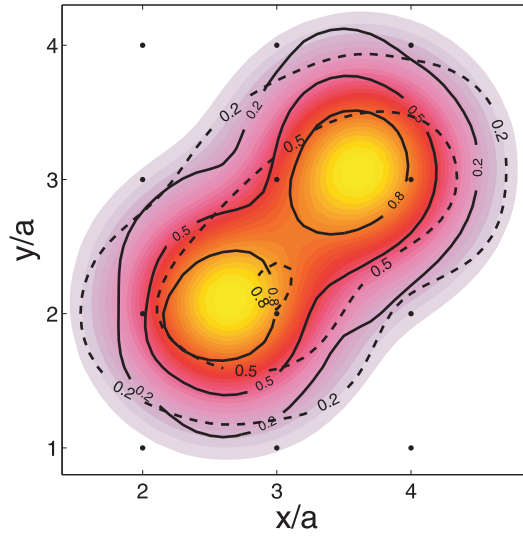


Figure 7.8: Shape of two structures with  $r = 0.5a$  and separation  $a$ . Solid contours show the the result obtained with super-resolution. The dashed lines corresponds to simple interpolation. The color filled contours represent the original gaussian structures.

snapshots over  $20 \mu\text{s}$  at 0, 10 and  $20 \mu\text{s}$  respectively. In order to simulate a typical plasma diagnostic, the data is downsampled by a factor 23, i.e. the initial resolution of  $256 \times 256$  is reduced to  $12 \times 12$ . The simple interpolated, low resolution images corresponding to the first row of pictures are shown in the next row of pictures in Fig. 7.9. Clearly, the large scale properties are similar, but the amplitudes are significantly lower and many small scale structures have disappeared or merged to larger ones. Hence, an agreement with original scenes cannot be stated. In the last row of pictures Fig. 7.9 shows the same undersampled data, but this time reconstructed using super-resolution. The overall agreement with original data set has significantly improved. The amplitudes are in good agreement and the number and positions of maxima are well reproduced. Even the shape of structures is much closer to the original data.

A quantification of the result is obtained by computing  $k$ -spectra. For sufficient statistics the spectra are averages of 35 images. To obtain a common scaling, all spectra are normalized to RMS-amplitude (Root Mean Square) of full resolution images. Fig. 7.10 shows the average  $k$ -spectra for original simulation data (dotted line), simple interpolation (dashed line) and super-resolution (solid line). To provide a link between wave vector  $k$  and the results obtained in the previous section a second scale in units of structure radius normalized to the grid size ( $a = 23$  pixel) is plotted. First, it is found that the simple interpolated data yields too low power even for small values of  $k$ , i.e. large structure size. An amplitude reduction of  $3\text{dB}$  is observed, i.e. only about 70% from original amplitude can be recovered. This is in good agreement with the result obtained for synthetic data (see Fig. 7.3).

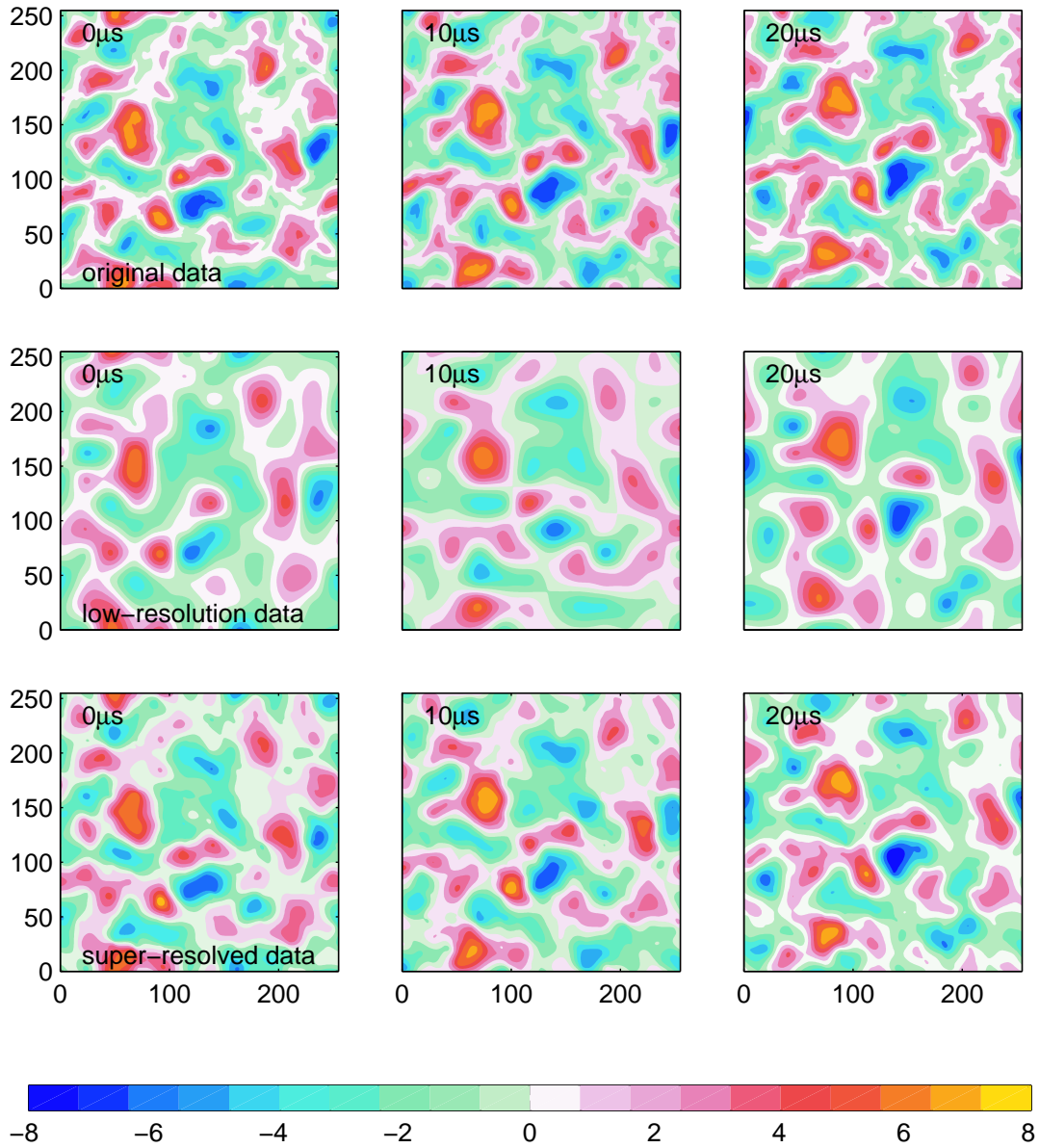


Figure 7.9: First row of three pictures show full resolution image of turbulent fluctuation obtained from a Hasegawa-Wakatani-drift wave model [116]. Second row of pictures show the result of simple interpolation applied to a down sampled data. Third row of images denote the result of super-resolution applied to the same down sampled data .

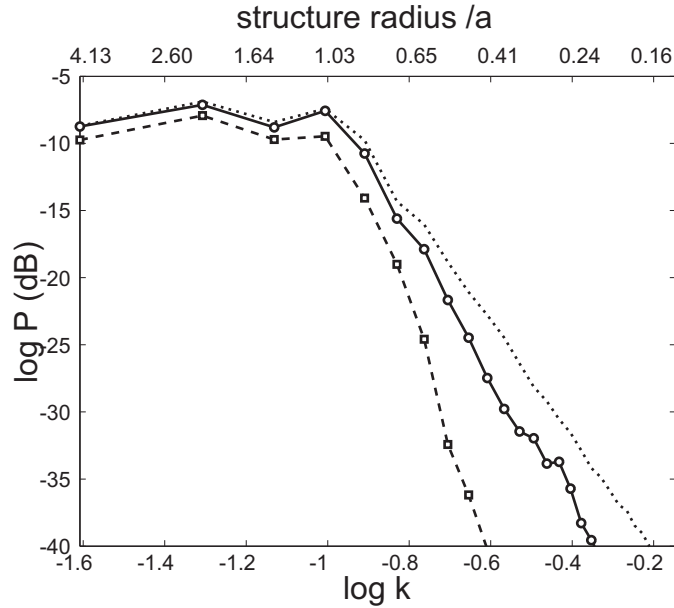


Figure 7.10: The  $k$  spectrum calculated from Fig. 7.9. The additional upper scale refers to the structure size definition used for synthetic data. The dotted line corresponds to Fig. 7.9a, the dashed line to the simple interpolation result shown in Fig. 7.9b, and the solid line refers to super-resolution (Fig. 7.9c).

However, for super-resolved data the information is recovered to almost 100%, as long as the structures are larger than the grid size ( $r > a$ ). Even for small structures ( $r < a$ ) a clear improvement is observed for super-resolution. For structure sizes down to  $r = 0.3a$  ( $\log k \approx -0.4$ ) the power law for super-resolution has an exponent close to those of the original data. Below  $r = 0.3a$  the slope of super-resolved and interpolated data is identical and is typical for the interpolation process. This is in full agreement with the results from synthetic data (Fig. 7.3) and indicates an enhancement of resolution.

### 7.3 Summary and conclusion

In this chapter the proposed super-resolution algorithm as a method for enhancement of the spatial resolution of spatio-temporally resolved plasma diagnostics was tested by application to synthetic data and turbulence data from simulation. It was shown that simple interpolation of typical experimental data does not yield reliable results for turbulence investigations. Amplitudes, trajectory and shape are found to be subject of severe errors even for structures being much larger than the spatial Nyquist limit. A detailed comparison with super-resolved data revealed that amplitude, trajectory and shape are significantly improved by application of our super-resolution algorithm. These important physical quantities are found to

be reproduced qualitatively and quantitatively, even for structures smaller than the spatial Nyquist limit. The application of the super-resolution algorithm to turbulence data obtained from a Hasegawa-Wakatani drift wave model showed that the algorithm is able to deal with typical turbulence data and significantly improves the results. Hence the proposed super-resolution is found suitable for plasma turbulence investigation [112]. This method promises to enable better diagnostics of transport processes in plasma turbulence and especially the investigation of large scale coherent structures, their dynamics and life time will benefit from super-resolution.

# Chapter 8

## Comparison of super-resolution and conditional averaging

The previous chapters have shown that spatio-temporal imaging of plasma fluctuations can be done using electrostatic probes in two ways, using conditional averaging (CA) technique, and using multi probes synchronous recordings by 2D-probe arrays. To understand the physical processes resolved by these diagnostic methods a comparison of them is required. Therefore, this chapter concentrates on comparison between synchronous measurements using 2D-probe array and CA results. For this reason, these two methods are applied to weak turbulence (multi mode) data from the KIWI experiment. For a better comparison the CA analysis is applied at similar resolution data set from 2D-probe array using synchronous recordings. To overcome the spatial resolution of 2D-probe array the data is improved using the super-resolution (SR) algorithm presented in the chapter 6. The main features of the turbulence, i.e. structure amplitude and spatial evolution, are analyzed in detail to quantify differences between CA and SR.

### 8.1 Spatio-temporal characterization of weak turbulence

In this chapter, spatio-temporally resolved density fluctuations of a weakly turbulence state are recorded and analyzed using conditional averaging (CA) method and super-resolution (SR) to compare the diagnostic methods. Before comparison a brief characterization of the turbulence in the KIWI device is presented in this section. It focuses on techniques used in previous works and will allow us to motivate the guide lines for the comparison of CA and SR. For CA analysis the improved method, as presented in the chapter 4 is used. The experimental setup was described in the Chapter 2 in detail.

### 8.1.1 Super-resolution results

As presented in the Chapter 2, a weakly turbulent plasma can be obtained in the magnetized midsection of the KIWI device by adjusting the grid voltage. Plasma density fluctuations in this regime have been already characterized from temporal evolution point of view in the Chapter 2. It was shown that the broad peaks in the low frequency regime of the spectrum correspond to typical frequencies of  $m=1\dots3$  drift modes. The decrease of the power spectrum is given by a power law  $S(f) = f^{-\alpha}$ , with  $\alpha \approx 3$ . These findings indicate that the turbulence is only weakly developed [75, 76].

Using simultaneously recorded data of the probe array the spatio-temporal evolution along the azimuthal direction can be visualized and quantified (Fig. 8.1a and Fig. 8.1b). These density fluctuations (Fig. 8.1a) are recorded in the area of the steepest gradients. The spatio-temporal density evolution is highly irregular and pronounced structures eventually occur and propagate in azimuthal direction. The slight difference of stripes inclination indicates that the velocity of the structures is not constant. Many of those spatio-temporal structures seem to have a finite lifetime and frequent phase dislocations can be observed. The corresponding mode number-frequency power spectrum (Fig. 8.1b) is obtained by direct Fourier transformation of the spatio-temporal data (Fig. 8.1a). The wave number spectrum indicates the presence of several modes involved. It shows more peaked spectra at low mode numbers and broader in rest. These results are in good agreement with previous measurements [8, 27] with probe arrays special designed for this 1D spatio-temporal analysis.

By super-resolving the new probe-array data, 2D pictures of plasma fluctuations which cover entire plasma column are obtained. Fig. 8.1c shows snap shots of plasma density fluctuations at different time instants. The values of the color bar denotes ion saturation currents normalized to the standard deviation of a reference probe localized in the region of the maximum density gradient. The pictures show a complex situation consisting of multiple maxima. Dominant are pictures with 1, 2 and 3 structures, as denoted by the spectra (Fig. 8.1b) too. Therefore, the weak turbulence state from the KIWI can be characterized as a multi mode situation, where the most stable drift modes in the KIWI, i.e.  $m=1,2,3$ , contribute significantly to the observed fluctuations.

### 8.1.2 Conditional averaging results

The weak turbulence state, at the same plasma conditions, is analyzed in this section using CA technique. For this reason a cross section in the middle of the device is scanned using the 2D positioning system (see Chapter 2 for technical details) with a resolution of 1 mm. As reference a probe of the array is again chosen. The trigger condition consists of a signal threshold of  $1.5 \cdot \sigma_{RP}$  and a window of  $0.2 \cdot \sigma_{RP}$  combined



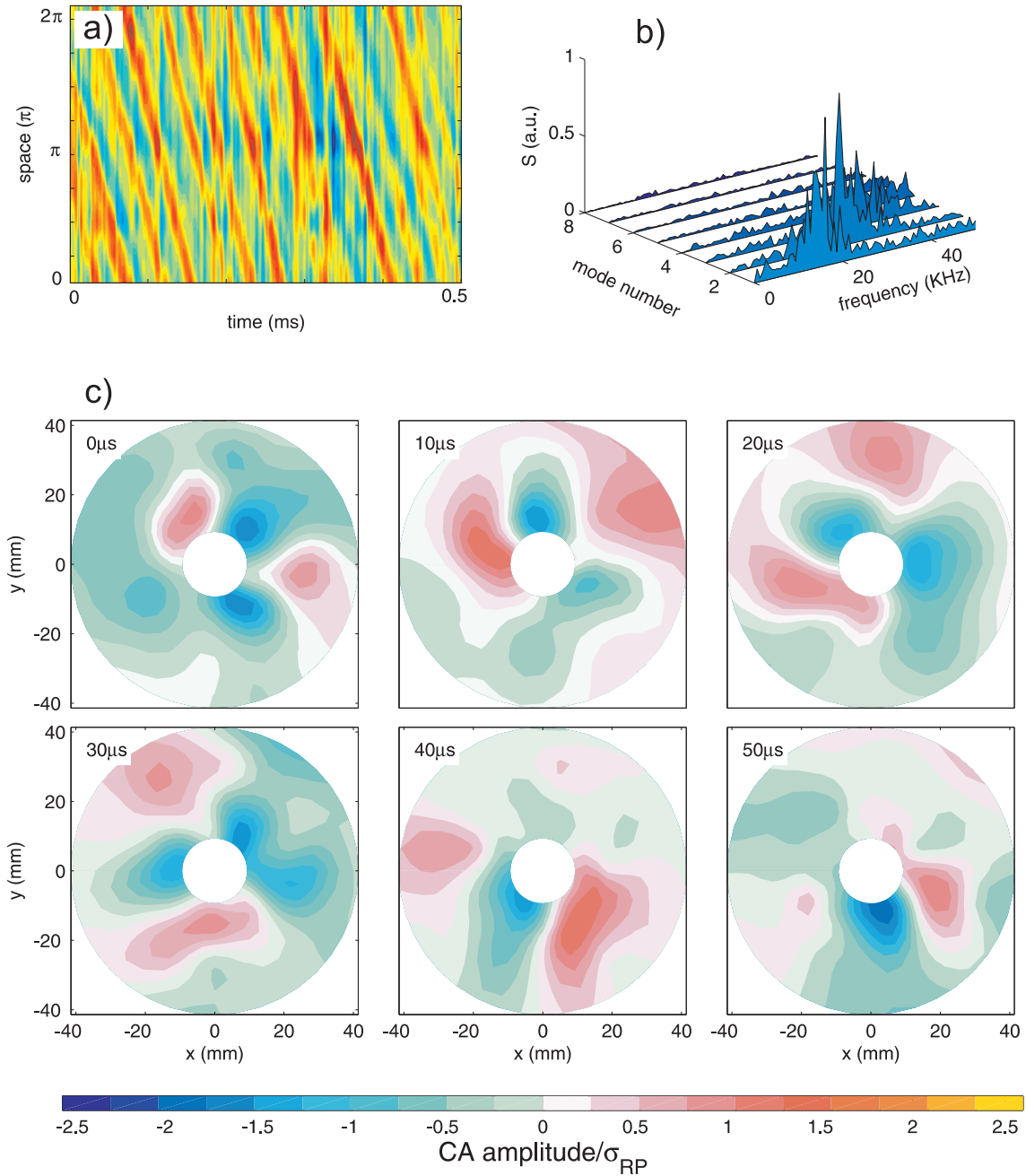


Figure 8.1: a) Spatio-temporal data, b) the frequency-mode number spectrum and c) plasma density fluctuations picture, using 2D probe array. The data used for these plots are acquired using 2D-probe array. For (a) and (b) the data from probes situated at the same radial positions in the region of steepest gradients, is used.

with a positive slope of the signal. The spatio-temporal evolution of the CA resolved structures is shown in Fig. 8.2a.

In order to compare the results of CA with SR, both techniques should be applied to data set recorded with similar resolution. For this reason the CA analysis is applied also on synchronous data from the 2D-array data. For both cases the same reference probe and the improved CA method (see Chapter 4) are used. The CA results on 2D-array data are shown in Fig. 8.2b.

By using the 2D positioning system (Fig. 8.2a), the averaging structures are spatially resolved with higher resolution, than using 2D probe array (Fig. 8.2b). However, in both CA results the development of a large-scale density structure can be clearly seen. The presence of one pronounced maxima which propagates anti-clockwise in azimuthal direction is observed. There is no difference in size of the structure and direction of propagation. Further, there are no phase shifts between different recording methods. All pictures indicate a monopole-like shape of the coherent structure and these results are in good agreement with previous investigations [27]. Therefore, due to the structure size even lower resolution of the 2D-array is suitable to obtain good results for a comparison with SR data. Furthermore, the CA of synchronous recording does not differ from asynchronous CA. Therefore, for a better comparison the 2D-array data can be used for both: CA analysis and SR.

At the first glance, the characterization presented in the previous section and the CA analysis of the same turbulence situation shows differences between CA and SR. On one hand, the improved CA analysis (see Chapter 4) has been developed in order to improve the amplitude information. Therefore, a quantitative comparison of SR and CA first implies an analyze of the resolved structures amplitude. On the other hand, SR indicates a complex spatial behavior of the turbulence consisting of mixture of drift wave modes (Fig. 8.1c) while by CA analysis a clear monopole-like structure is obtained (Fig. 8.2). This is a notable difference that demands further investigations.

## 8.2 The amplitude evolution

As shown in the Chapter 3 the amplitude estimate of the standard CA is critical. The cross-correlation based improved CA method (see chapter 4) promises better results and a comparison with SR results allows to judge whether the resolved amplitude is sufficient. For this reason the amplitude of the CA monopole-like structure (Fig. 8.2b) is compared with amplitudes of the original selected structures contained in 2D array data and improved by SR (Fig. 8.1c). This comparison is made for different trigger thresholds of CA analysis. Fig. 8.3 shows the amplitude statistics of SR data. The results are normalized to the standard deviation of the reference probe. In this amplitude distribution, only those structures with higher amplitude than the trigger threshold and with similar spatial location as the CA structure at

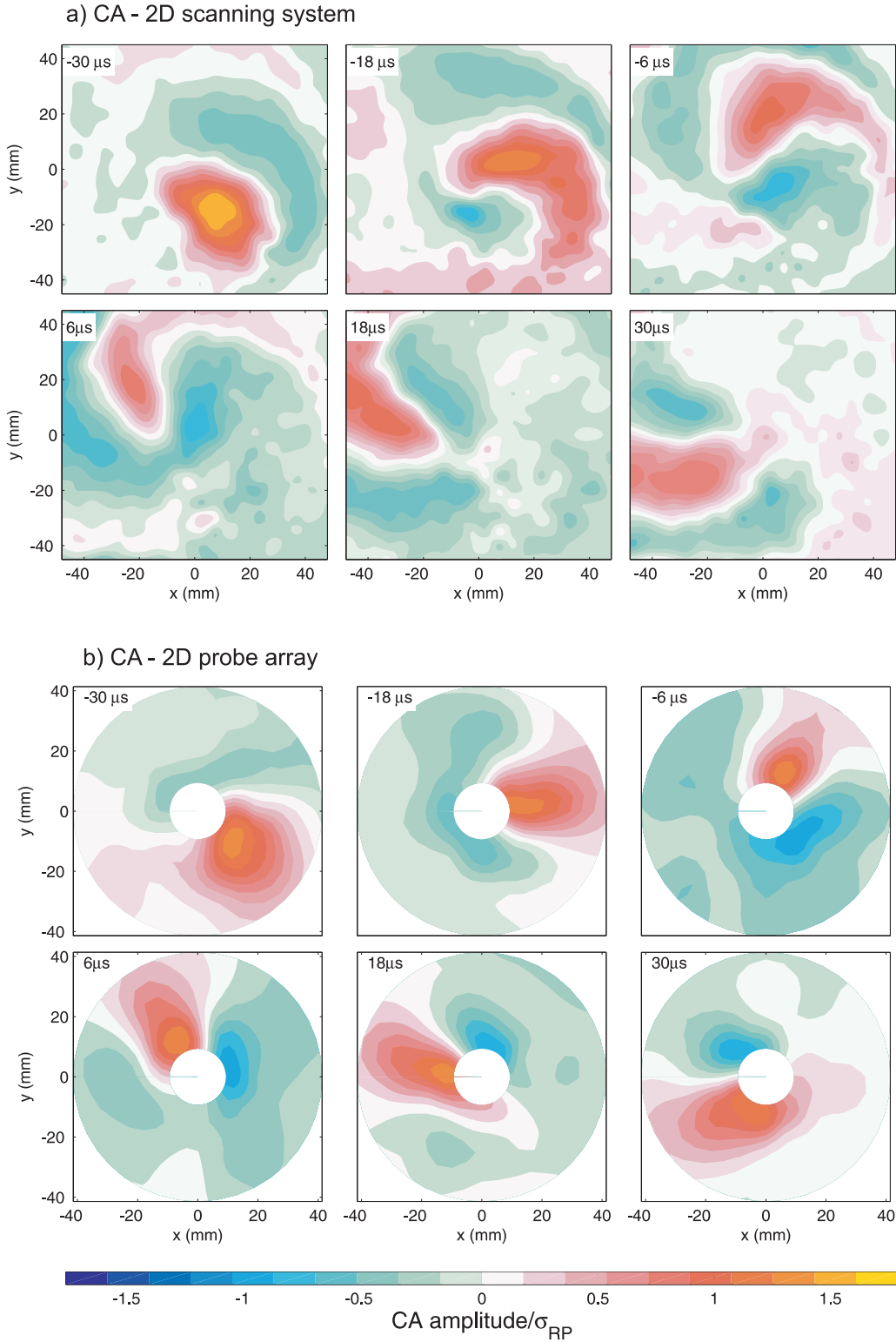


Figure 8.2: Conditionally averaged density fluctuations recorded in the azimuthal section perpendicular to the magnetic field. a) The CA analysis is done with standard procedure by using the 2D positioning system to gain spatial information. b) CA results using 2D-array synchronous recorded data. The values at the color bar are ion saturation currents in units of standard deviation of the reference probe.

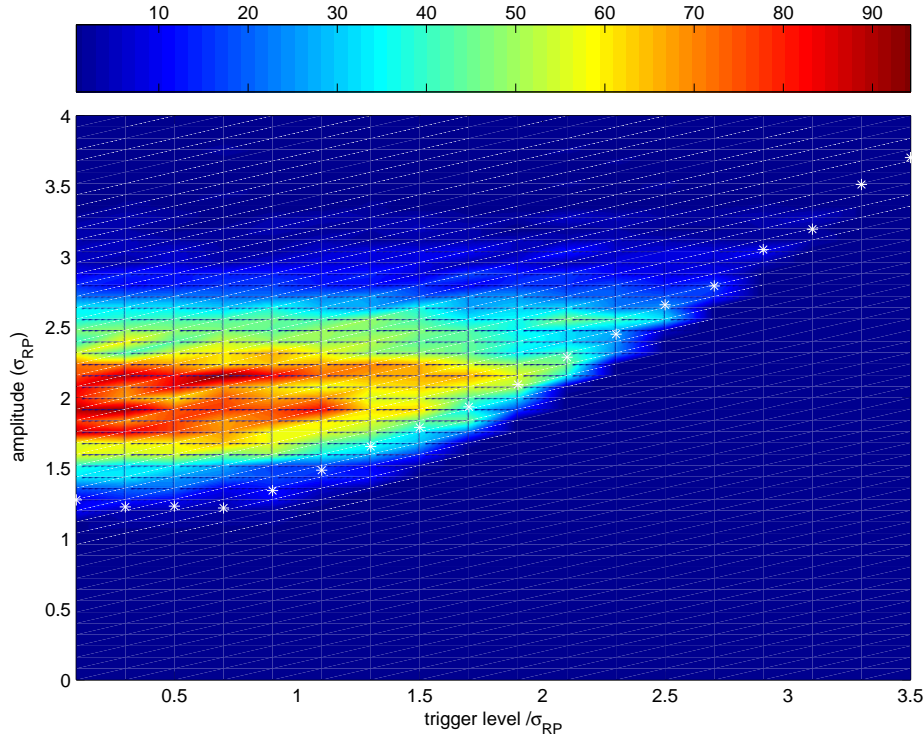


Figure 8.3: The structures amplitude statistics for weak turbulence in KIWI. The white dots represent CA structure amplitude at different trigger thresholds. The background color plot shows the amplitude distribution of structures selected in CA analysis. The color bar indicates the number of structures.

$\tau = 0\mu s$  are considered. It shows a broad distribution of amplitudes, i.e. between  $1.5 - 2.5 \cdot \sigma_{RP}$ . By white stars the amplitude of the resolved monopole-like structure by CA analysis at  $\tau = 0\mu s$  is denoted. The trigger level and the trigger window ( $0.2 \cdot \sigma_{RP}$ ) effects lead to CA structures amplitude values in the lower boundary of the distribution. These results are in good agreement with CA results presented in the chapter 4. Even for a low trigger level the CA amplitudes are reasonable. However, CA amplitudes are still at the lower bound whereas the average SR structure amplitudes are higher.

### 8.3 The spatio-temporal structure

To address the second question, namely why CA analysis yields an azimuthal propagation of a monopole-type density structure while the other method indicates a complex behavior of multiple structures, individual 2D snap shots at the same time instants, i.e.  $\tau = 0\mu s$ , as presented in Fig. 8.4 are analyzed. To simplify the analysis, the spatial distribution along the structure trajectory is considered by taking

only one radial position (line-plots from Fig. 8.4). This is justified because CA and SR results (Fig. 8.3b and Fig. 8.2c) indicate a mostly azimuthal propagation of the resolved structure. For comparison randomly selected subseries of SR data, which were used for CA, are presented in Fig. 8.4. The CA result shows only one clear maximum at spatial position  $\phi = 1.6 \cdot \pi$ . Due to the trigger condition SR indicates always a maximum at  $\phi = 1.6 \cdot \pi$  as well, but in many cases there are additional maxima. The positions of the additional maxima differ from a subseries to another.

To analyze the relation between CA and SR results in more detail the distance between SR structures is of interest. This distance is computed as the separation length between the maxima at  $\phi = 1.6 \cdot \pi$  and the neighboring maxima (black dots). The distance distribution for all selected subseries is shown in Fig. 8.5. This distribution shows a number of structures at the same spatial position as the CA structure, i.e. due to the trigger threshold, and in rest a broad distribution with small broad peaks at about  $2 \cdot \pi/4$ ,  $2 \cdot \pi/3$  and  $2 \cdot \pi/2$ . These peaks indicate the pattern of drift modes in this weak turbulence state, i.e.  $m=1..4$ .

Guided by the results presented upon the contribution of modes to the fluctuation (see 8.1.1) we now use the distance between maxima as an estimation of the wavelength of the drift mode. To understand this effect let take the most extreme case where the structure distance statistics is the wavelength statistics of monochromatic modes. Although, this is a cruel assumption which makes the most extreme case. If it is possible to explain the relation of CA monopole and sinusoidal wave, it will certainly hold for short wave-pattern as well. By considering the monochromatic wave as a harmonic oscillation, i.e.  $\cos(2 \cdot \pi/d_k \cdot x)$  with  $x = 0..2 \cdot \pi$  and  $d_k$  be the structures distance, the averaging results (Fig. 8.6) show a monopole (red dashed line) that fits the CA-measurement very well (blue solid line). At first glance this seems to be a surprising result, but mathematically, this is not. It is well known that a broad distribution of wave lengths can be used to produce a localized wave package or even a delta function. Hence our measurement shows directly that the wave spectrum observed in experiment yields a CA monopole, i.e.  $\delta = \sum_k (\cos(k \cdot x))$ .

Further this means that the CA analysis cannot give information on the structure shape because this wavelength analysis is possible only for synchronous data. This analysis fails for two probes technique where the measurements are asynchronous.

## 8.4 Conclusion

In this chapter the results of super-resolution and conditional averaging methods on weak turbulence data from the KIWI experiment have been compared. The spatio-temporal evolution of weak turbulence means, from CA analysis point of view, azimuthal propagation of a monopole-type density structure, while by SR the

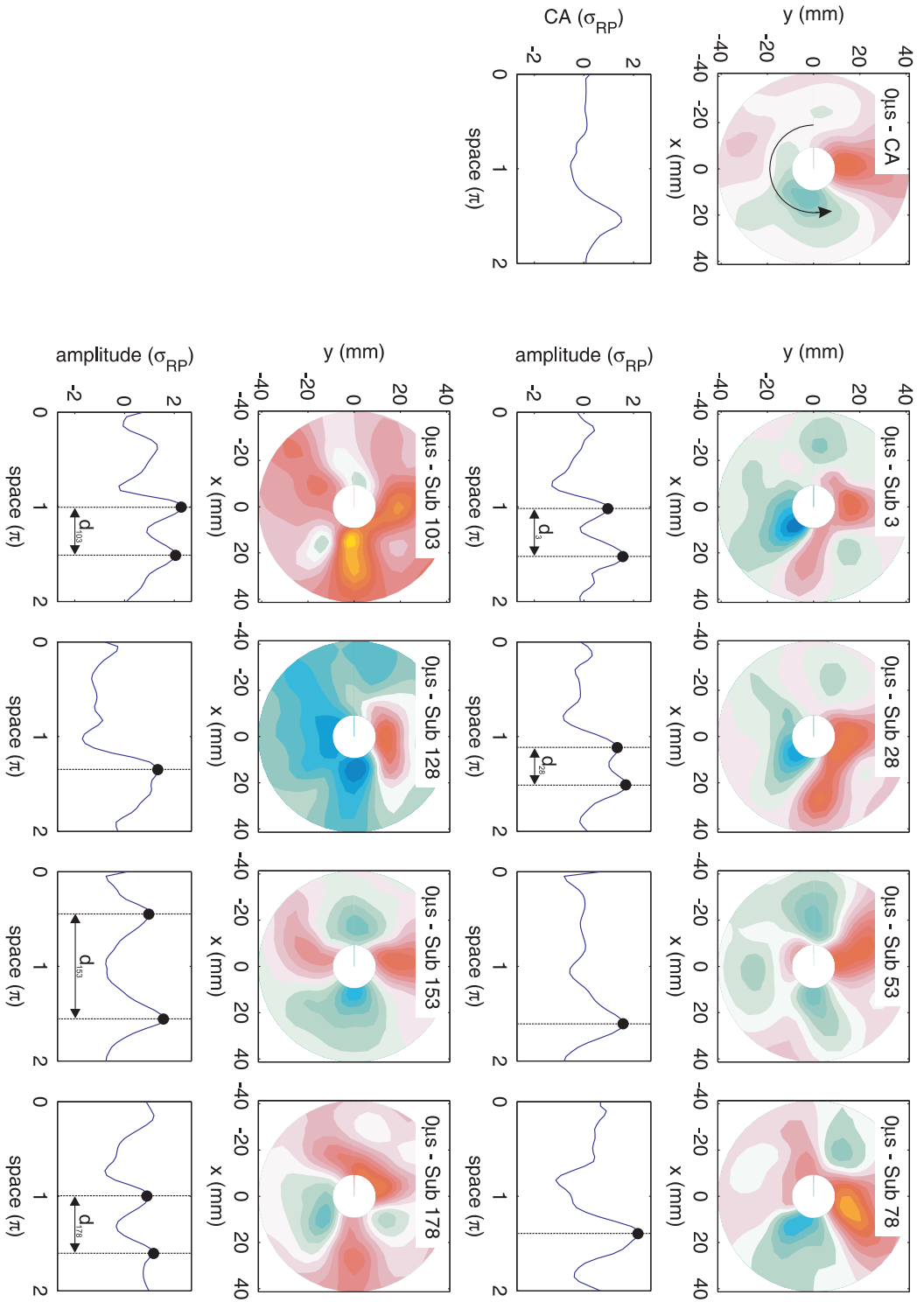


Figure 8.4: Pictures of the spatial distribution of density fluctuations at the time instant  $\tau = 0 \mu\text{s}$ , where the trigger condition is met in CA analysis. First color picture denotes the CA analysis result while rest of color pictures are SR representation of the 2D-array data. The line-plots denote the density fluctuations along the azimuthal direction in the steepest gradients region. The structure distance is marked with  $d_k$  ( $k=1..$ number of selected subseries).

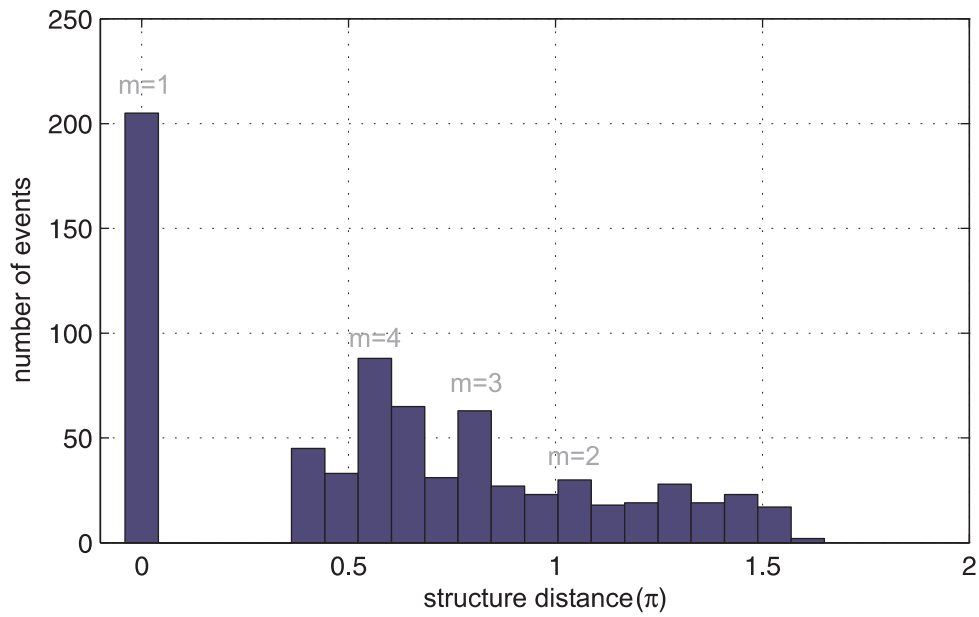


Figure 8.5: The structure distance statistics for SR data. Zero denote monopole-type structure. The broad peaks in the distribution indicate drift modes pattern, i.e.  $m=2,4$ .

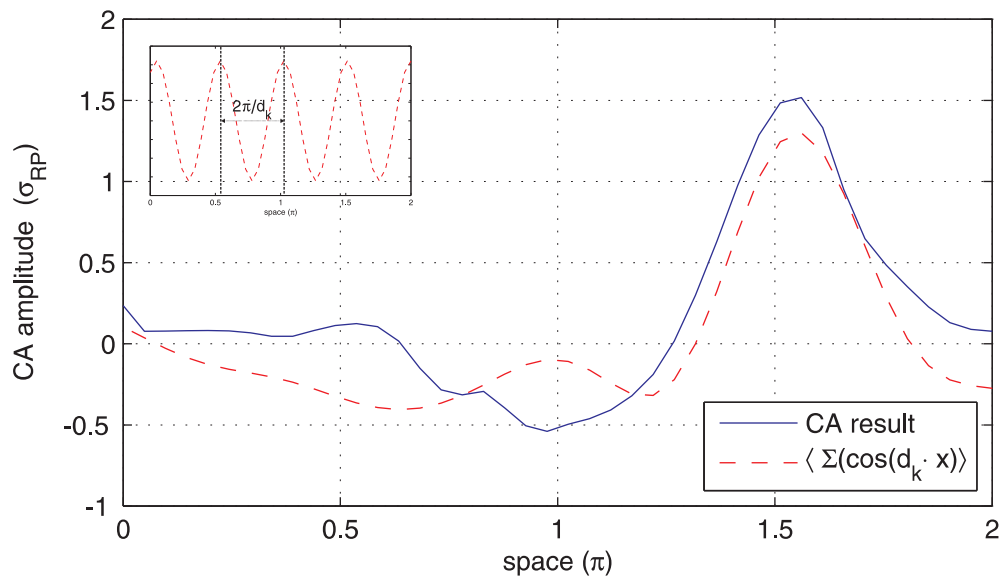


Figure 8.6: The averaging result of monochromatic modes (red dashed line) with broad wavelength distribution (Fig. 8.4). The small plot in the upper corner indicates an example of the artificial monochromatic mode signal. The blue line indicates the CA result from experiment.

turbulence state implies a complex behavior of multiple structures. It was shown that CA give reliable results only for local approximation around the reference but it fails to resolve the global evolution. Therefore, for characterization of the turbulence instantaneous spatio-temporal measurements are needed.



# Chapter 9

## Summary and conclusions

Spatio-temporal investigations of plasma fluctuations from the linear KIWI device were made using advanced Langmuir probe methods. First, the conditional averaging technique was applied. It yields to spatio-temporal information about plasma fluctuations by analyzing the statistical relationships between a fixed and a movable probe. For this a 2D scanning system with a spatial resolution of 1 mm has been constructed. Second, a new 2D-probe array which cover entire plasma column was constructed and used for multi-point simultaneous recordings of plasma fluctuations.

It was shown that the conditional averaging is an apparently simple technique that uses only two probes and gives high spatial and temporal resolution. A detailed comparison of the model predictions and conditional averaged synthetic data has shown that the conditional averaging process introduces a significant amplitude reduction to the data. The reason of this amplitude reduction was found to be caused by false trigger events, i.e. trigger events that are caused by the background noise without any coherent signal being involved. Further, the comparison showed that conditional averaging is not sensitive with respect to structure size, i.e. only large amplitude fluctuations are detected by this method. This causes severe implications in the experiment on the estimation of anomalous transport caused by the coherent structures. An amplitude reduction of density and potential structures by a factor of up to three each, would yield a contribution to transport that is nearly one order of magnitude too low. The origin of the amplitude damping found by using synthetic data was analyzed in the experiment using the correlation analysis of the conditional averaging results. It was shown that reliable amplitude of conditional averaging can be obtained using an advanced correlation analysis that defines the proper choice of the trigger condition. However, it was shown that the averaging process implies that only the average temporal evolution is observed, which can be quite different from the real dynamics.

By using the 2D-probe array for spatio-temporal diagnostics it was shown that a limited number of probes ( $\simeq 1$  probe/cm<sup>2</sup>) cannot provide the necessary spatial resolution for advanced investigations. This can give severe limitations on advanced

turbulence diagnostics, i.e. energy cascades, transport barriers, etc. Although, the mentioned diagnostics are very limited in spatial resolution their temporal resolution is in most cases by far sufficient. In many cases sample rates of 1 Ms/s are achieved which is almost one order of magnitude higher than necessary. Along the idea to use this wealth of information to improve the spatial resolution, a post-processing algorithm (super-resolution) that transfer information from the time-domain into the space-domain by proper interpolation was adapted from computer-vision to our 2D-probe array. Based on cross-correlation analysis of the temporal information, the super-resolution algorithm was used even with very small number of grid points as it is typically found for probe array data.

The capability of the proposed super-resolution algorithm for spatial improvement of 2D probe array data was proven first on synthetic data and then on experimental data. A detailed analysis on synthetic data showed that the amplitude, trajectory and shape are significantly improved. These important physical quantities are found to be well reproduced qualitatively and quantitatively, even for structures smaller than the spatial Nyquist limit. The application of the super-resolution algorithm on turbulence data obtained from a Hasegawa-Wakatani drift wave model showed that the algorithm is capable to handle typical turbulence data and significantly improves the results. Hence, the proposed super-resolution method was found suitable for plasma turbulence investigation. This method promises to enable better diagnostics of transport processes in plasma turbulence and especially the investigation of large-scale coherent structures, the investigation of their dynamics and life time will benefit from super-resolution.

In this thesis it was shown that spatio-temporal imaging of plasma fluctuations can be performed using electrostatic probes in two ways, namely using conditional averaging technique and multi probes synchronous recordings by 2D-probe arrays. To understand the physical processes resolved by these diagnostic methods, a comparison of them was presented in the final chapter. For this reason, results of super-resolution and conditional averaging method on weak turbulence data from the KIWI experiment were analyzed. It was shown that the spatio-temporal evolution of weak turbulence means, from the conditional averaging analysis point of view, that an azimuthal propagation of a monopole-type density structure prevails, while super-resolution analysis implies a more complex behavior of multiple structures. It was shown that conditional averaging gives reliable results only for the local approximation around the reference probe but fails to resolve a global evolution. Therefore, to characterize the turbulence correctly, instantaneous spatio-temporal measurements are needed.

In this work the advanced techniques for spatio-temporal plasma fluctuations diagnostic was experimentally tested on simple low- $\beta$  devices. In these experiments where steady state operation is possible drift waves and weak turbulence (multi-mode) states were studied directly with probes. Especially, the linear magnetized configuration has the advantage of allowing to study the transition from a simple

situation (monochromatic wave) to a complicated (weak turbulence) in a well controlled experiment. These are solid basics to develop and test the principles of new diagnostics. In general the introduced methods are not restricted to these systems. As the simulation has shown the application of the super-resolution does only require spatio-temporal data. Electrostatic probes are only one possibility. In fusion devices the application of super-resolution to the gas puff imaging ([45, 46]) or emission spectroscopy should be possible.

In general, the spatial under-sampled data is not only found in plasma physics. Other fields like geophysics, astrophysics or medicine suffer under limited spatial resolution cause by a limited number of recording channels, while the recording speed of the capturing techniques make possible temporally over-resolved data records. Therefore, the proposed super-resolution algorithm presented here can provide a feasible solution for spatial resolution improvement in many fields.



# Bibliography

- [1] W. Horton. Drift wave turbulence and anomalous transport. In A. A. Galeev and R. N. Sudan, editors, *Handbook of Basic Plasma Physics*, volume 2, chapter 6.4, pages 383–449. North-Holland Physics, Amsterdam, 1984.
- [2] Hidalgo C. *et al.* Edge turbulence and anomalous transport in fusion plasmas. *Plasma Phys. Controlled Fusion*, 37(11A):A53–A67, 1995.
- [3] A. J. Wootton, B. A. Carreras, H. Matsumoto, K. McGuire, W. A. Peebles, Ch. P. Ritz, P. W. Terry, and S. J. Zweben. Fluctuations and anomalous transport in tokamaks. *Phys. Fluids B*, 2(12):2879–2903, 1990.
- [4] B. Fischer and M. Krämer. Experimental study of drift wave turbulence and anomalous transport. *Plasma Phys. Controlled Fusion*, 31(3):453–470, 1989.
- [5] J. Bleuel, M. Endler, H. Niedermeyer, M. Schubert, H. Thomsen, and the W7-AS Team. The spatial structure of edge fluctuations in the Wendelstein 7-AS stellarator. *New Journal of Physics*, 4:38, 2002.
- [6] F. Wagner and U. Stroth. Transport in toroidal devices - the experimentalist's view. *Plasma Phys. Controlled Fusion*, 35:1321–1371, 1993.
- [7] M. Endler, H. Niedermeyer, L. Giannone, E. Holzhauser, A. Rudyj, G. Theimer, N. Tsois, and ASDEX Team. Measurements and modelling of electrostatic fluctuations in the scrape-off layer of ASDEX. *Nucl. Fusion*, 35(11):1307–1339, 1995.
- [8] A. Latten. *Multisondendiagnostik von Driftwellenturbulenz und anomalem Radialtransport in Laborplasmen*. PhD thesis, Christian-Albrechts-Universität Kiel, 1997.
- [9] Dietmar Block. *Synchronization of drift waves and its effects on fluctuation-induced transport*. PhD thesis, Christian-Albrechts-Universität Kiel, 2002.
- [10] A. H. Nielsen, H. L. Pécseli, and J. J. Rasmussen. Turbulent transport in low- $\beta$  plasmas. *Phys. Plasmas*, 3(5):1530–1544, 1996.

- [11] C. Lechte, S. Niedner, and U. Stroth. Comparison of turbulence measurements and simulations of the low-temperature plasma in the torsatron TJ-K. *New Journal of Physics*, 4:34, 2002.
- [12] M. Kick, H. Maassberg, M. Anton, J. Baldzuhn, M. Endler, C. Görner, M. Hirsch, A. Weller, S. Zoletnik, and the W7-AS Team. Electric field and transport in W7-AS. *Plasma Phys. Controlled Fusion*, 41:A549–A559, 1999.
- [13] M. Endler, I. García-Cortés, C. Hidalgo, G. F. Matthews, ASDEX Team, and JET Team. The fine structure of ELMs in the scrape-off layer. *Plasma Phys. Controlled Fusion*, 47(2):219–240, 2005.
- [14] S. K. Saha and R. Kumar. Effect of poloidal velocity shear on the edge fluctuations in the SINP tokamak. *Plasma Phys. Controlled Fusion*, 46(7):1065–1074, 2004.
- [15] Burrell K. H. *et al.* Tests of causality: Experimental evidence that sheared  $E \times B$  flow alters turbulence and transport in tokamaks. *Phys. Plasmas*, 6(12):4418–4435, 1999.
- [16] H. W. Hendel, T. K. Chu, and P. A. Politzer. Collisional drift waves—identification, stabilization, and enhanced plasma transport. *Phys. Fluids*, 11:2426–2439, 1968.
- [17] F. F. Chen. Electric probes. In H. Huddelstone, editor, *Plasma Diagnostic Techniques*. Academic, New York, 1965.
- [18] N. Hershkowitz. How langmuir probes work. In O. Auciello and D. L. Flamm, editors, *Plasma Diagnostics*, volume 1, pages 113–183. Academic, San Diego, CA, 1989.
- [19] J. E. Allen. Probe theories and applications: modern aspects. *Plasma Sources Sci. Technol.*, 4:234–241, 1995.
- [20] F. J. Øynes, O.-M. Olsen, H. L. Pécseli, A. Fredriksen, and K. Rypdal. Experimental study of low-frequency electrostatic fluctuations in a magnetized toroidal plasma. *Phys. Rev. E*, 57(2):2242–2255, 1998.
- [21] N. Mahdizadeh, F. Greiner, M. Ramisch, U. Stroth, W. Guttenfelder, C. Lechte, and K. Rahbarnia. Comparison of langmuir and emissive probes as diagnostics for turbulence studies in the low-temperature plasma of the torsatron TJ-K. *Plasma Phys. Controlled Fusion*, 47(4):569–579, 2005.
- [22] L. Giannone, R. Balbín, H. Niedermeyer, M. Endler, G. Herre, C. Hidalgo, A. Rudyj, G. Theimer, Ph. Verplanke, and W7-AS Team. Density, temperature, and potential fluctuation measurements by swept Langmuir probe technique in Wendelstein 7-AS. *Phys. Plasmas*, 1:3614–3621, 1994.

- [23] M. Endler, L. Giannone, K. McCormick, H. Niedermeyer, A. Rudyj, G. Theimer, N. Tsois, S. Zoletnik, ASDEX Team, and W7-AS Team. Turbulence in the SOL of ASDEX and W7-AS. *Physica Scripta*, 51:610–616, 1995.
- [24] A. Latten, T. Klinger, A. Piel, and Th. Pierre. A probe array for the investigation of spatio-temporal structures in drift wave turbulence. *Rev. Sci. Instrum.*, 66(5):3254–3262, 1995.
- [25] A. Latten. Entwicklung eines 64-Kanal-Transientenrekorders zur Untersuchung turbulenter Driftwellen. Master's thesis, Christian-Albrechts-Universität Kiel, 1994.
- [26] Christiane Schroder, Olaf Grulke, Thomas Klinger, and Volker Naulin. Drift waves in a high-density cylindrical helicon discharge. *Phys. Plasmas*, 12(4):042103, 2005.
- [27] Olaf Grulke. *Investigation of large-scale spatiotemporal fluctuation structures in magnetized plasmas*. PhD thesis, Christian-Albrechts-Universität Kiel, 2001.
- [28] Carsten Lechte. *Microscopic structure of plasma turbulence in the torsatron TJ-K*. PhD thesis, Christian-Albrechts-Universität Kiel, 2003.
- [29] S. J. Zweben. Search for coherent structure within tokamak plasma turbulence. *Phys. Fluids*, 28:974–982, 1985.
- [30] B. LaBombard and B. Lipschultz. Densepack: An array of langmuir probes in the limiter shadow plasma of alcator c tokamak fusion experiment. *Rev. Sci. Instrum.*, 10:2415–2424, 1986.
- [31] H. Thomsen, M. Endler, T. Klinger, and the W7-AS Team. Active probe experiments at the Wendelstein 7-AS stellarator. *Plasma Phys. Controlled Fusion*, 47(9):1401–1414, 2005.
- [32] J. Zweben. Search for coherent structure within tokamak plasma turbulence. *Phys. Fluids*, 28(3):974–982, 1985.
- [33] Mirko Ramisch. *Scaling and manipulation of turbulent structures in the torsatron TJ-K*. PhD thesis, Christian-Albrechts-Universität Kiel, 2005.
- [34] D. L. Rudakov, M. G. Shats, R. W. Boswell, C. Charles, and J. Howa. Overview of probe diagnostics on the H-1 heliac. *Rev. Sci. Instrum.*, 70:476, 1999.
- [35] K. Ohkuni, K. Toi, S. Ohdachi, and S. Takagi. Langmuir probe array for edge plasma study on the compact helical system heliotron/torsatron. *Rev. Sci. Instrum.*, 70:419, 1999.

- [36] S. J. Jeon, G. S. Eom, J. H. Kim, and W. Choe. Multichannel rf-compensated langmuir probe array driven by a single bias supply. *Rev. Sci. Instrum.*, 73:277, 2002.
- [37] E. Martines, M. Hron, and J. Stöckel. Coherent structures in the edge turbulence of the castor tokamak. *Plasma Phys. Controlled Fusion*, 44:351–359, 2002.
- [38] M. Bruchhausen, R. Burhenn, M. Endler, G. Kocsis, A. Pospieszczyk, S Zoletnik, and W7-AS Team. Fluctuation measurements on the Wendelstein 7-AS stellarator by means of repetitive lithium laser blow-off. *Plasma Phys. Controlled Fusion*, 46(3):489–505, 2004.
- [39] S. J. Zweben, J. Caird, W. Davis, D. W. Johnson, and B. P. Le Blanc. Plasma turbulence imaging using high-power laser thomson scattering. *Rev. Sci. Instrum.*, 72(1):1151–1154, 2001.
- [40] H. Parket *et al.* Recent advancements in microwave imaging plasma diagnostics. *Rev. Sci. Instrum.*, 74:4239, 2003.
- [41] W. Horton. Drift waves and transport. *Rev. Mod. Phys.*, 71(3):735–778, 1999.
- [42] O.E. Garcia, V. Naulin, A.H. Nielsen, and J.J. Rasmussen. Computations of intermittent transport in scrape-off layer plasmas. *Phys. Rev. Lett.*, 92(16):165003, 2004.
- [43] Z.Lin, T.S. Hahm, W.W. Lee, W.M. Tang, and R.B. White. Turbulent transport reduction by zonal flows: Massively parallel simulations. *Science*, 281:1835–1837, 1998.
- [44] M. Lesieur. *Turbulence in Fluids*, volume 1 of *Fluid Mechanics and its Applications*. Kluwer Academic Publishers, Dordrecht, 2. edition, 1990.
- [45] J. L. Terry, S. J. Zweben, B. Bose, O. Grulke, E. S. Marmor, J. Lowrance, V. Mastrocola, and G. Renda. High speed movies of turbulence in Alcator C-Mod. *Rev. Sci. Instrum.*, 75:4196–4199, 2004.
- [46] R. J. Maqueda, G. A. Wurden, D. P. Stotler, S. J. Zweben, B. LaBombard, J. L. Terry, J. L. Lowrance, V. J. Mastrocola, G. F. Renda, D. A. D’Ippolito, J. R. Myra, and N. Nishino. Gas puff imaging of edge turbulence (invited). volume 74, pages 2020–2026. AIP, 2003.
- [47] Zhen Xiangjun, Hu Liqun, Wan Baonian, Chen Zhongyong, Shi Yuejiang, Lin Shiyao, Ding Yonghua, Zhou Liwu, and HT-7 Team. The electron temperature estimation using soft x-ray imaging in HT-7 tokamak. *Plasma Science and Technology*, 8(2):147–150, 2006.



- [48] R. J. Adrian. Conditional eddies in isotropic turbulence. *Phys. Fluids*, 22(11):2065–2070, 1979.
- [49] T. Huld, A. H. Nielsen, H. L. Pécseli, and J. J. Rasmussen. Coherent structures in two-dimensional plasma turbulence. *Phys. Fluids B*, 3(7):1609–1625, 1991.
- [50] F. Greiner, D. Block, and A. Piel. Observation of mode like coherent structures in curved magnetic fields of a simple magnetized torus. *Contrib. Plasma Phys.*, 44(4):335–346, 2004.
- [51] Christiane Schroder, Olaf Grulke, Thomas Klinger, and Volker Naulin. Spatial mode structures of electrostatic drift waves in a collisional cylindrical helicon plasma. *Phys. Plasmas*, 11(9):4249–4253, 2004.
- [52] O. Grulke, T. Klinger, M. Endler, A. Piel, and W7-AS Team. Analysis of large-scale fluctuation structures in the scrape-off layer of the Wendelstein 7-AS stellarator. *Phys. Plasmas*, 8(12):5171–5180, 2001.
- [53] Zhang Guo-Ping, He Ye-Xi, Wang Wen-Hao, Gao Zhe, Zeng Li, Xie Li-Feng, and Feng Chun-Hua. Observation of radial propagation of electrostatic fluctuations in edge plasma of the sino united spherical tokamak. *Chinese Physics Letters*, 21(12):2469–2471, 2004.
- [54] C. Schröder. Experimentelle untersuchungen des globalen dynamischen plasmagleichgewichts in plasmaexperiment KIWI. Master’s thesis, Christian-Albrechts-Universität Kiel, April 1999.
- [55] J. Noetzel. Destabilisierung und sättigung von driftwellen in experiment Kiwi. Master’s thesis, Christian-Albrechts-Universität Kiel, Dezember 1996.
- [56] U. Boelter. Untersuchungen zur Wechselwirkung stromgetriebener Driftwellen mit Potentialrelaxationsoszillationen. Master’s thesis, Christian-Albrechts-Universität Kiel, Januar 1996.
- [57] T. Pierre, G. Leclert, and F. Braun. Magnetized double-plasma device for wave studies. *Rev. Sci. Instrum.*, 58:6–11, 1987.
- [58] K. N. Leung, G.R. Taylor, J. M. Barrick, S. L. Paul, and R. E. Karibel. Plasma confinement by permanent magnet boundaries. *Phys. Lett. A*, (57):145, 1976.
- [59] T. Fujita, T. Ohnuma, and S. Adachi. Plasma states in a cylindrical cusp-shaped magnetic field composed of a permanent magnet array. *Plasma Phys.*, 23(11):1019–1026, 1981.
- [60] R. Limpaecher and K. R. MacKenzie. Magnetic multipole containment of large uniform collisionless quiescent plasmas. *Rev. Sci. Instrum.*, 44(6):726–731, 1973.

- [61] H. M. Mott-Smith and I. Langmuir. The theory of collectors in gaseous discharges. *Phys. Rev.*, 28:727–763, 1926.
- [62] J. E. Allen. Probe theory - the orbital motion approach. *Physica Scripta*, 45:497–503, 1992.
- [63] I. D. Sudit and R. C. Woods. A study of the accuracy of various Langmuir probe theories. *J. Appl. Phys.*, 76(8):4488–4497, 1994.
- [64] K. Hansen, T. Klinger, and A. Piel. Computer controlled probe diagnostic system and application in a magnetized laboratory plasma. *Rev. Sci. Instrum.*, 65(8):2615–2622, 1994.
- [65] N. Hershkowitz and M. H. Cho. Measurements of plasma potential using collecting and emitting probes. *J. Vac. Sci. Technol.*, 6(3):2054–2059, 1988.
- [66] I. Langmuir. The interaction of electron and positive ion space charges in cathode sheaths. *Phys. Rev.*, 33:954–990, 1929.
- [67] R. F. Kemp and J. M. Sellen. Plasma potential measurements by electron emissive probes. *Rev. Sci. Instrum.*, 37(4):455–461, 1966.
- [68] E. Y. Wang, N. Hershkowitz, T. Intrator, and C. Forest. Techniques for using emitting probes for potential measurement in RF plasmas. *Rev. Sci. Instrum.*, 57(10):2425–2431, 1986.
- [69] D. Diebold, N. Hershkowitz, A. D. Bailey III, M. H. Cho, and T. Intrator. Emissive probe current bias method of measuring dc vacuum potential. *Rev. Sci. Instrum.*, 59(2):270–275, 1988.
- [70] G. M. Jenkins and D. G. Watts. *Spectral analysis and its applications*. Holden-Day, San Francisco, 1968.
- [71] M. F. Priestley. *Spectral analysis and time series*. Academic, San Diego, 6 edition, 1998.
- [72] H. L. Pécseli. *Fluctuations in Physical Systems*. Cambridge University Press, Cambridge, 2000.
- [73] E. J. Powers. Spectral techniques for experimental investigation of plasma diffusion due to polychromatic fluctuations. *Nucl. Fusion*, 14:749–752, 1974.
- [74] E. Marden-Marshall, R. F. Ellis, and J. E. Walsh. Collisional drift instability in a variable radial electric field. *Plasma Phys. Controlled Fusion*, 28(9B):1461–1482, 1986.

- [75] T. Klinger, A. Latten, A. Piel, T. Pierre, and G. Bonhomme. Experimental study of transition phenomena from regular to turbulent drift waves. In S. Benkadda, F. Doveil, and Y. Elskens, editors, *Transport, Chaos and Plasma Physics 2*. World Scientific, Singapore, 1996.
- [76] T. Klinger, A. Latten, A. Piel, G. Bonhomme, T. Pierre, and T. Dudok de Wit. The route to drift wave chaos and turbulence in a bounded low- $\beta$  plasma experiment. *Phys. Rev. Lett.*, 79:3913–3916, 1997.
- [77] R. F. Ellis and E. Marden-Marshall. Comparison of local and nonlocal theories of the collisional drift instability. *Phys. Fluids*, 22:2137–2139, 1979.
- [78] R. E. Kaplan and J. Laufer. In *Proc. 12th Int. Cong. Appl. Mech.*, page 236, Stanford Univ., 1969.
- [79] L. S. G. Kovasznay, V. Kibens, and R. F. Blackwelder. *J. Fluid. Mech.*, 41:283, 1970.
- [80] T. C. Tung und R. J. Adrian. Higher-order estimates of conditional eddies in isotropic turbulence. *Phys. Fluids*, 23:1469–1470, 1980.
- [81] H. Johnson, H. L. Pécseli, and J. Trulsen. Conditional eddies in plasma turbulence. *Phys. Fluids*, 30(7):2239–2254, 1987.
- [82] Y. G. Guezennec. Stochastic estimation of coherent structures in turbulent boundary layers. *Phys. Fluids*, 1(6):1054–1060, 1989.
- [83] H. L. Pécseli and J. Trulsen. A statistical analysis of numerically simulated plasma turbulence. *Phys. Fluids B*, 1(8):1616–1636, 1989.
- [84] H. L. Pécseli and J. Trulsen. Analytical expression for conditional averages: A numerical test. *Physica Scripta*, 43:503–507, 1990.
- [85] D. Block, I. Teliban, F. Greiner, and A. Piel. Prospects and limitations of conditional averaging. *Physica Scripta*, T122:25–33, 2006.
- [86] Barni R *et al.* Formation of spiral structures and radial convection in the edge region of a magnetized rotating plasma. *New Journal of Physics*, 7(225), 2005.
- [87] T. Huld, A. H. Nielsen, H. L. Pécseli, and J. J. Rasmussen. Coherent structures in two-dimensional plasma turbulence. *Phys. Fluids B*, 3(7):1609–1625, 1991.
- [88] O. Grulke, T. Klinger, and A. Piel. Experimental study of the dynamics of conditionally averaged structures in weakly developed electrostatic turbulence. *Phys. Plasmas*, 6(3):788–796, 1999.
- [89] H. Tasso, B. J. Green, and H. P. Zehrfeld. Stationary equilibrium for the toroidal theta pinch. *Phys. Fluids*, 12(11):2444–2445, 1969.

- [90] K Avinash and S N Bhattacharyya. On the impossibility of plasma equilibria with flow in magnetic fields having only a toroidal component. *Plasma Phys. Controlled Fusion*, 34(6):1163–1167, 1992.
- [91] F. Greiner, O. Grulke, C. Lechte, and A. Piel. RF-plasma in a simple magnetized torus. In *Proc. 2000 Int. Congress on Plasma Physics*, volume 1, pages 140–143, Quebec City, Canada, 2000.
- [92] O Grulke, F Greiner, T Klinger, and A Piel. Comparative experimental study of coherent structures in a simple magnetized torus. *Plasma Phys. Controlled Fusion*, 43(4):525–542, 2001.
- [93] C. Riccardi and Å. Fredriksen. Waves and coherent structures in the turbulent plasma of a simple magnetized torus. *Phys. Plasmas*, 8:199–209, 2001.
- [94] Å Fredriksen, C Riccardi, L Cartegni, and H Pécseli. Coherent structures, transport and intermittency in a magnetized plasma. *Plasma Phys. Controlled Fusion*, 45(5):721–733, 2003.
- [95] S. V. Ratynskaia, V. I. Demidov, and K. Rypdal. Measurements of anomalous particle and energy fluxes in a magnetized plasma. *Physical Review E (Statistical, Nonlinear, and Soft Matter Physics)*, 65(6):066403, 2002.
- [96] U. Frisch. *Turbulence: The Legacy of A. N. Kolmogorov*. Cambridge University Press, Cambridge, 1995.
- [97] N. Omrane and Phil L. Palmer. Superresolution for translated satellite images using the walsh functions. *Proceedings of SPIE*, 5238:62–71, 2004.
- [98] S. Peled and Y. Yeshurun. Superresolution in MRI: Application to human white matter fiber tract visualization by diffusion tensor imaging. *Magnetic Resonance in Medicine*, 45:29–35, 2001.
- [99] R. Peeters *et al.* The use of superresolution techniques to reduce slice thickness in functional MRI. *International Journal of Imaging Systems and Technology (IJIST), Special issue on High Resolution Image Reconstruction*, 14(3):131–138, 2004.
- [100] R. Lagendijk and J. Biemond. *Iterative Identification and Restoration of Images*. Kluwer Academic Publishers, 1991.
- [101] Sean Borman. *Topics in Multiframe Superresolution Restoration*. PhD thesis, University of Notre Dame, Notre Dame, IN, May 2004.
- [102] R. Tsai and T. Huang. Multi-frame image restoration and registration. *Advances in Computer Vision and Image Processing*, 1:317–339, 1984.

- [103] J.L. Barron, D.J. Fleet, and S.S. Breauchemin. Performance of optical flow techniques. *International Journal of Computer Vision*, 12(1):43–77, 1994.
- [104] S.S. Breauchemin and J.L. Barron. The computation of optical flow. *ACM Computing Surveys*, 27(3):433–467, 1996.
- [105] B.D. Lucas and Takeo Kanade. An iterative technique of image registration and its application to stereo. *Proc. 7th International Joint Conference on Artificial Intelligence*, pages 674–679, 1981.
- [106] B.K.P. Horn and B.G. Schunck. Determining optical flow. *Artificial Intelligence*, 17:185–204, 1988.
- [107] M. Irani and S. Peleg. Improving resolution by image registration. *Journal of Computer Vision, Graphics, and Image Processing*, 53(3):231–239, 1991.
- [108] M. Irani and S. Peleg. Motion analysis for image enhancement: Resolution, occlusion, and transparency. *Journal of Visual Communication and Image Representation*, 4:324–335, 1993.
- [109] A. Khintchine. Korrelationstheorie der stationären Prozesse. *Math. Ann.*, 109:604–615, 1934.
- [110] David T. Sandwell. Biharmonic spline interpolation of GEOS-3 and SEASAT altimeter data. *Geophysical Research Letters*, 14:139–142, 1987.
- [111] C.L. Luengo Hendriks and L.J. van Vliet. Resolution enhancement of a sequence of undersampled shifted images. *Proc. 5th Annual Conference of the Advanced School for Computing and Imaging (Heijen, NL, June 15-17)*, pages 95–102, 1999.
- [112] I Teliban, D Block, A Piel, and V. Naulin. A super-resolution method for spatio-temporal plasma diagnostics. *Plasma Phys. Controlled Fusion*, 48(3):419–431, 2006.
- [113] D. Block and A. Piel. Transport studies of driven drift waves i: monochromatic waves. *Plasma Phys. Controlled Fusion*, 45(4):413–425, 2003.
- [114] D. Block and A. Piel. Transport studies of driven drift waves ii: weak turbulence. *Plasma Phys. Controlled Fusion*, 45(4):427–437, 2003.
- [115] P. W. Terry. Suppression of turbulence and transport by sheared flow. *Rev. Mod. Phys.*, 72(1):109–165, 2000.
- [116] A. Hasegawa and M. Wakatani. Plasma edge turbulence. *Phys. Rev. Lett.*, 50:682–686, 1983.

## Publications

### Journal papers

1. D. Block, I. Teliban, F. Greiner and A. Piel.  
"Prospects and limitations of conditional averaging",  
*Phys. Scripta* **T122**, 25–33 (2006).
2. I. Teliban, D. Block A. Piel and V. Naulin.  
"Super-Resolution method for spatio-temporal plasma diagnostics",  
*Plasma Phys. Control. Fusion* **48**, 1–13 (2006).
3. I. Teliban, D. Block, A. Piel and F. Greiner.  
"Improved conditional averaging technique for plasma fluctuations diagnostics",  
*submitted to Plasma Phys. Control. Fusion*.

### Conference papers

1. I. Teliban, D. Block and A. Piel. "Application of super-resolution method to Langmuir probe arrays" in *Proceedings of the 33rd EPS Conference on Plasma Physics, Rome, 2006*

## Acknowledgments

First of all I would like to thank to Prof. Dr. A. Piel for offering me the great opportunity to prepare the present work in his group. I benefitted a lot from the discussions with him and from his encouragements.

I would like to express my gratitude to Dr. D. Block who helped me a lot, despite his new responsibilities for his first children. His interest in my work and the many discussions were extremely valuable during the preparation of this work. He also showed exceptional persistence in the corrections of the final manuscript. Furthermore, I want to thank to him and his wife, Annya, for their help and friendship.

Thanks for all funny times and interesting cultural experiences to my colleagues: O. Arp, M. Klindworth, M. Hirt, I. Goertz, M. Kroll, I. Pilch, S. Knist and H. Maurer. I owe many thanks to my office colleague T. Trottenberg who helped me any time I needed. My life would have been in danger without precious advices from Dr. F. Greiner. The technical support of V. Rohwer and M. Poser helped me a lot at the experimental part of the work. Special thanks belongs also to M. Brix and his team for the shown professionalism in the construction of the new probe array. Thanks to our secretaries Mrs. M. Seeger and Mrs. S. Thiedemann for helping me with the bureaucratic part. Many thanks to DR. C. Zafiu for the careful reading of the thesis. I would also like to thank my romanian friends who made my stay in Kiel a pleasure.

My most profound thanks for my precious wife for all the love, support, and encouragement a man could ask for.





## Curriculum Vitae

### personal data

name: Iulian Teliban  
 date of birth: 23.05.1978  
 place of birth: Dorohoi, Romania  
 nationality: Romanian  
 marital status: Married

### school education

1985 – 1989 Primary School, Dorohoi, Romania  
 1989 – 1993 Secondary School, Dorohoi, Romania  
 1993 – 1987 Theoretical High School of Computer Science, Dorohoi, Romania

### scientific education

1997 – 2001 Study of physics at the "Al. I. Cuza" University, Iasi, Romania  
 06/2001 State examination and diploma thesis at the "Al. I. Cuza" University, Iasi, Romania (mark 9.38 from 10)  
 2001 – 2003 Master studies in plasma physics at the "Al. I. Cuza" University, Iasi  
 02/2003 – 08/2003 Research scholarship (Erasmus-Socrates) at Physics Institute of the University on Innsbruck, Austria  
 09/2003 Master of Science in plasma physics (mark 10 from 10)  
 since 11/2003 Ph.D. graduation in the Christian-Albrechts University, Kiel  
 Subject: Spatio-temporal diagnostics of plasma fluctuations with probe arrays and statistical techniques.

### **Eidesstattliche Erklärung**

Hiermit versichere ich an Eides Statt, dass die vorliegende Dissertation, abgesehen von der Beratung durch meinen wissenschaftlichen Lehrer und der Verwendung der angegebenen Hilfsmittel, nach Inhalt und Form meine eigene ist. Sie hat weder ganz noch teilweise an einer anderen Stelle im Rahmen eines Prüfungsverfahrens vorgelegen. Die Arbeit ist unter Einhaltung der Regeln guter wissenschaftlicher Praxis entstanden.

Kiel, den .....